BULK-FLOW ANALYSIS FOR FORCE AND MOMENT COEFFICIENTS OF A SHROUDED CENTRIFUGAL COMPRESSOR IMPELLER

A Thesis

by

MANOJ KUMAR GUPTA

Submitted to the Office of Graduate Studies of
Texas A&M University
in partial fulfillment of the requirements for the degree of

MASTER OF SCIENCE

May 2005

Major Subject: Mechanical Engineering

BULK-FLOW ANALYSIS FOR FORCE AND MOMENT COEFFICIENTS OF A SHROUDED CENTRIFUGAL COMPRESSOR IMPELLER

A Thesis

by

MANOJ KUMAR GUPTA

Submitted to the Office of Graduate Studies of
Texas A&M University
in partial fulfillment of the requirements for the degree of

MASTER OF SCIENCE

Approved as to style and content by:

_____
Dara W. Childs
(Chair of Committee)

_____
John M. Vance
(Member)

_____ _____
Hamn Ching Chen Dennis O'Neal
(Member) (Head of Department)

May 2005

Major Subject: Mechanical Engineering

ABSTRACT

Bulk-Flow Analysis for Force and Moment Coefficients of a Shrouded Centrifugal Compressor Impeller. (May 2005)
Manoj Kumar Gupta, B.Tech., Indian Institute of Technology-Madras
Chair of Advisory Committee: Dr. Dara W. Childs

An analysis is developed for a compressible bulk-flow model of the leakage path between a centrifugal compressor's impeller shroud and housing along the front and back side of the impeller. This is an extension of analysis performed first by Childs (1989) for a shrouded pump impeller and its housing considering an incompressible fluid, and then later by Cao (1993) using a compressible bulk flow model for the shroud of a cryogenic fluid pump. The bulk-flow model is used to develop a reaction force and moment model for the shroud of a centrifugal compressor by solving the derived governing equations and integrating the pressure and shear stress distribution. Validation is done by comparing the results to published measured moment coefficients by Yoshida et al. (1996). The comparison shows that the shroud casing clearance flow and the fluid force moment can be simulated by the bulk flow model fairly well. An Iwatsubo-based labyrinth seal code developed by Childs and Scharrer (1986) is used to calculate the rotordynamic coefficients developed by the labyrinth seals in the compressor. Tangential force and transverse moment components acting on the rotor are found to have a destabilizing influence on the rotor for a range of precession frequencies. Rotordynamic coefficients are derived for a single stage of a multistage centrifugal compressor, and a comparison is made to stability predictions using Wachel's coefficient using the XLTRC (rotordynamic FEA code). For the model employed, Wachel's model predicts a slightly lower onset speed of instability. The results also show that leakage that flows radially inwards on the back shroud has a greater destabilizing influence than leakage flow that is radially outwards. Seal rub conditions are simulated by increasing the clearance and simultaneously decreasing the tooth height, which increased the leakage and the swirl to

the eye seal inlet; and therefore reduced stability. Calculated results are provided for different seal clearances and tooth height, for seal and shroud forces and moments.

DEDICATION

This work is dedicated to my professor Dr. Dara Childs, in special recognition for the guidance, support and enthusiasm he gave me throughout my stay at Texas A&M University. His knowledge, guidance, energy, humour, openness, companionship and inspiration will always serve as an example of the perfect supervisor.

ACKNOWLEDGEMENTS

I would take this opportunity to express my sincere thanks and gratitude to Dr. Dara Childs for providing the opportunity to work on this special project. The guidance, support, and wisdom given by Dr. Childs has been of great personal benefit. He has been an ever-present force in helping me mature as a student and as a researcher. His dedication to helping me succeed and his patience and tolerance continue to amaze me.

I would also like to thank Dr. John Vance for his support and knowledge, especially in the field of rotordynamics, and Dr. Hamn Ching Chen for serving on my thesis panel. I must thank Dr. Bart Childs for helping me with stiff ordinary differential equations and Stephen Philips for helping with software. Dr. Yoshida and Dr. Tsujimito deserve a special mention for their immediate response with the emails.

Many thanks to my friends at the Texas A&M for all the fun and collaboration: Avijit Bhattacharya (who also helped so much in discussions and technical matters), Ganesh Mohan, Ashwin, Zachary Zutavern, Amit Pandey, Rowan Gontier, Yusuke Kawato, and Eric Hensley. These are only a few names, since I cannot adequately acknowledge all of the people to whom I am indebted. I hope the rest will know who they are and that I thank them very much.

TABLE OF CONTENTS

Page

LIST OF FIGURES

FIGURE Page

LIST OF TABLES

TABLE Page

NOMENCLATURE

A_{1s}, A_{2s}, A_{3s}, A_{4s}, A_{5s},	
$A_{1\theta}$, $A_{2\theta}$, $A_{3\theta}$, $A_{4\theta}$	Coefficients introduced in equation. (53-55)
$b = V_i/R\omega$	Nondimensional velocity ratio.
C_{de}	Discharge coefficient for the exit wearing ring seal.
C_i	Initial (s=0) clearance. (m)
$f=\Omega/\omega$	Nondimensional frequency ratio.
$h = H/C_i$	Nondimensional clearance.
H	Clearance between impeller shroud and housing. (m)
L	Axial path length. (m)
L_s	Leakage path length. (m)
M	Mach number-fluid velocity/acoustic velocity.
P	Fluid static pressure. (bar)
$P = P/\rho_i V_i^2$	Dimensionless pressure.
$P_s(\theta,t)$	Dimensionless inlet supply pressure. (s=0)
$P_e(\theta,t)$	Dimensionless seal exit pressure.
R	Radial coordinate. (m)
R_i	Initial radial coordinate. (m)
$R_\alpha = 2HU_s/\nu$	Reynolds number defined in equation. (18)
$R = R/R_i$	Dimensionless radial coordinate.
S	Path coordinate. (m)
$s = S/L_s$	Nondimensionalized path length.
$T = L_s/V_i$	Representative transit time for fluid traversing the leakage path. (s)
t	Time. (s)
$u_s = U_s/V_i$	Nondimensionalized path fluid velocity.
$u_\theta = U_\theta/R_i\omega$	Nondimensionalized circumferential fluid velocity.
U_s	Path velocity of fluid (m/s)
U_θ	Circumferential velocity of fluid (m/s)
V_i	Initial path velocity of fluid at s=0 (m/s)

ε	Perturbation parameter
λ_r, λ_s	Friction factor definitions provided in equations (29) and (30)
σ_r, σ_s	Wall friction factor defined in equation (28)
μ	Fluid viscosity (N-s/m^2)
ρ	Fluid density (Kg/m^3)
$\tilde{\rho} = \rho/\rho_i$	Nondimensionalized fluid density
$\tau = \omega t$	Nondimensionalized time
τ_w	Wall shear stress (N/m^2)
τ_s, τ_r	Shear stress on stator and rotor surfaces (N/m^2)
θ	Circumferential coordinate
ω	Rotor angular velocity (s^{-1})
Ω	Shaft precession angular velocity (s^{-1})
ξ	Inlet loss coefficient
ν	Kinematic viscosity (m^2/s)
j	$\sqrt{-1}$
I	Mass moment of inertia

Subscripts

r,s	Rotor and stator
z,θ	Axial and circumferential directions
0,1	Zeroth and first-order perturbations

INTRODUCTION

A centrifugal compressor is a device that pressurizes a working fluid, and the basic aim of using a centrifugal compressor is to compress the fluid and deliver it at a pressure higher than its original pressure. Centrifugal compressors are an integral part of the petrochemical industry, finding extensive use because of their higher reliability compared to other types of compressors. Fig. 1 shows a typical multistage centrifugal compressor.

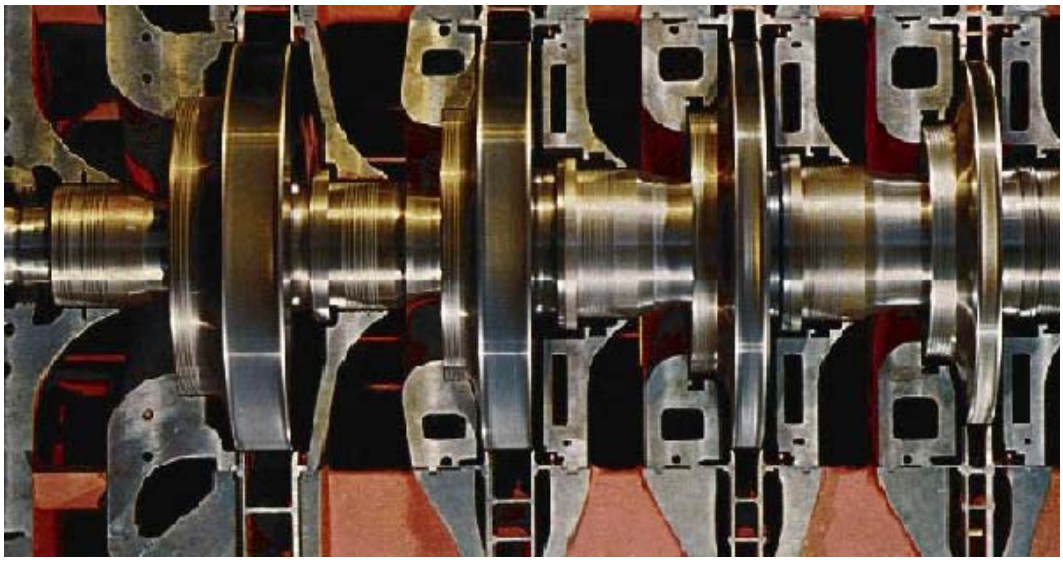

Fig. 1 Multistage centrifugal compressor [1]

Centrifugal Compressor Type

High-pressure compressors can use either the straight, flow-through (series) or back-to-back (parallel) designs as shown in Fig. 2. In the through-flow design, flow enters from the left and proceeds directly from impeller to impeller, discharging to the right.

The journal model is the Journal of Engineering for Gas Turbines and Power.

For the back-to-back design, flow enters at the left and proceeds from left to right through the first four stages, then follows a crossover duct to the right-hand side of the machine, and proceeds from right to left through the last four stages, discharging at the center. The advantages and disadvantages of the two configurations can best be described by paraphrasing Childs [2]: "Back-to-back machines obviously react a smaller axial thrust than series machines, but the back-to-back compressors are more sensitive to the forces from the central labyrinth than are the series machines to forces from the balance-drum labyrinth." The central labyrinth seal of Fig. 2 is normally called a division wall seal.

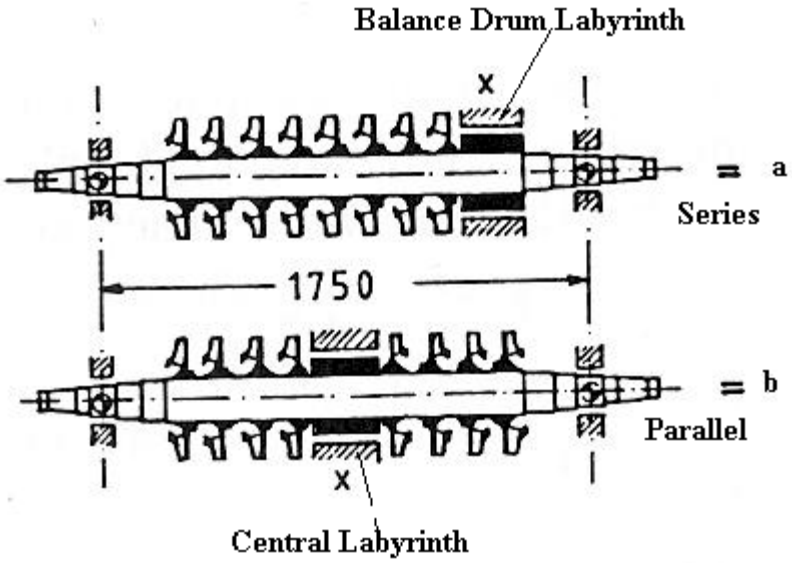

Fig. 2 (a) Flowthrough or series and (b) back-to-back or parallel compressor designs [2]

Fig. 3 shows various parts of a typical multistage centrifugal compressor with the standard nomenclature. Some of the important parts of a centrifugal compressor from the current research's point of view are: shrouded impellers, and eye-packing, interstage, balance-piston, and division wall seals.

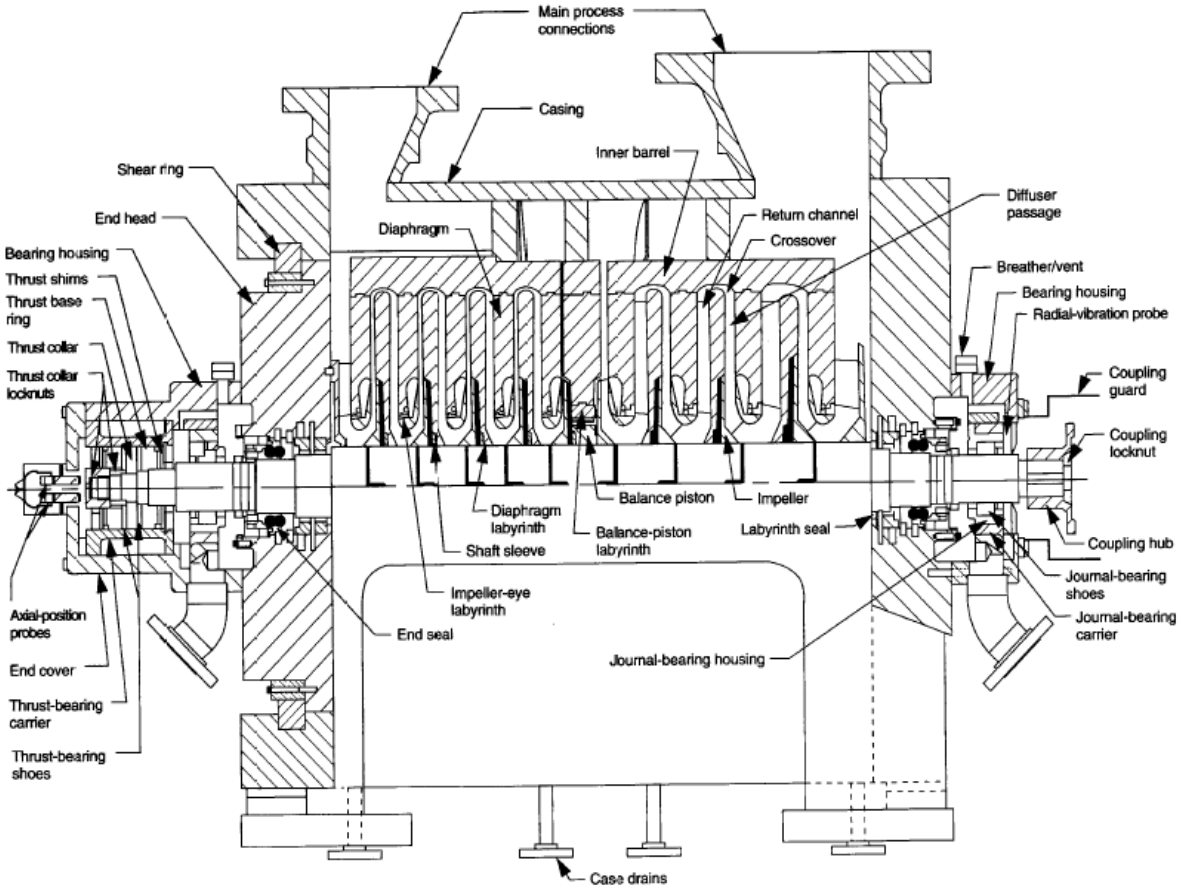

Fig. 3 Back-to-back centrifugal compressor nomenclature [3]

Shrouded impellers, as shown in Fig. 4, are the rotating parts that accelerate fluid to a high speed and imparts energy to the fluid. Flow enters the impeller in the axial direction and leaves in the radial direction. Fig. 5 shows the leakage path for front and back shroud along with the eye packing labyrinth and the shaft seal labyrinth. Eye packing seals restrict leakage flow along the front side of the impeller from impeller discharge to impeller inlet, and the interstage seal restricts flow along the shaft between stages. Balance piston labyrinth restricts leakage on the discharge end of the machine and in a series compressor, leakage flow through the balance piston is returned to the inlet; hence; the balance piston absorbs the full ΔP of the compressor. The division wall seal in a back-to-back compressor is employed to minimize leakage from the last stage of the compressor and the last stage of the initial series of impellers. Thus the division wall

absorbs about one half of compressor ΔP and is at a smaller diameter than a balance piston. Flow on the back shroud of impellers is normally radially outwards, but the leakage direction for the last stage is generally inwards.

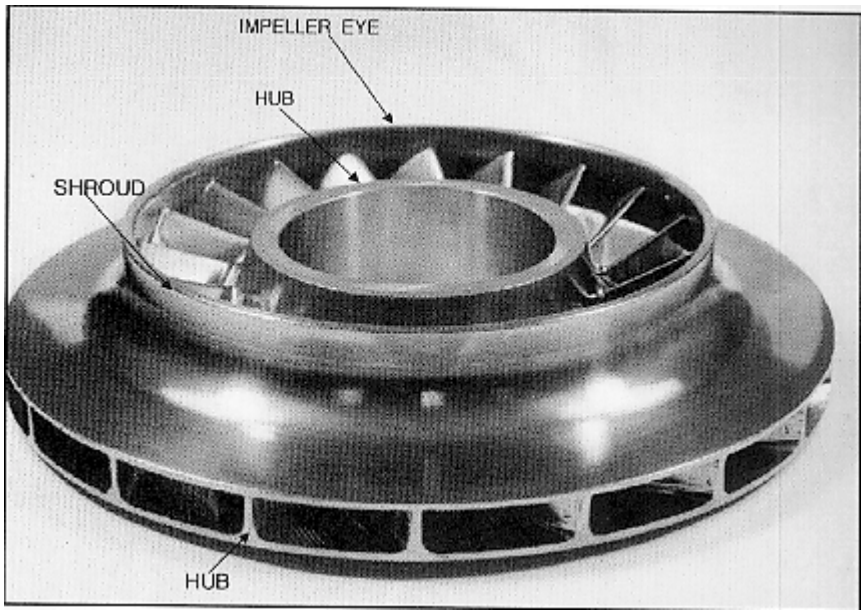

Fig. 4 Centrifugal closed-faced impeller [4]

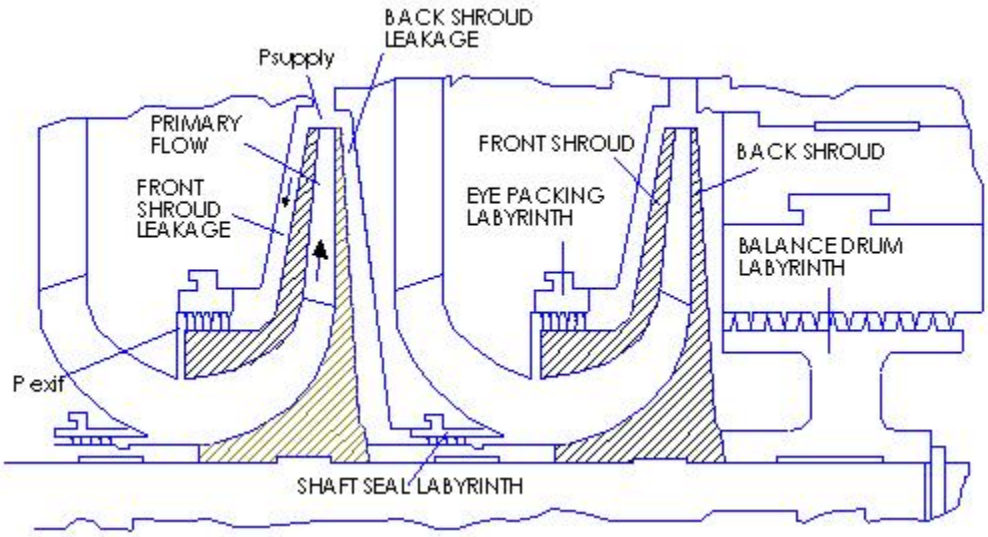

Fig. 5 Schematic of the centrifugal impeller with seals [2]

Shunt Hole Injection

Shunt holes (Fig. 6) are defined as a feature to bring gas from the discharge volute or diffuser to the entrance of the balance piston or division wall labyrinth seal. The intent is to prevent entry of swirling flow from the back of the impeller into the seal, since the destabilizing cross-coupling forces of the labyrinth seals are strongly dependent on inlet swirl of the leakage flow. Because of the diffuser's gain in static pressure, the shunt causes the flow behind the last impeller to go from the seal to the larger radius of the impeller tip, reversing the direction it would go without the shunt. The gas supplied by the shunt holes to the labyrinth comes in either radially or against the shaft rotation.

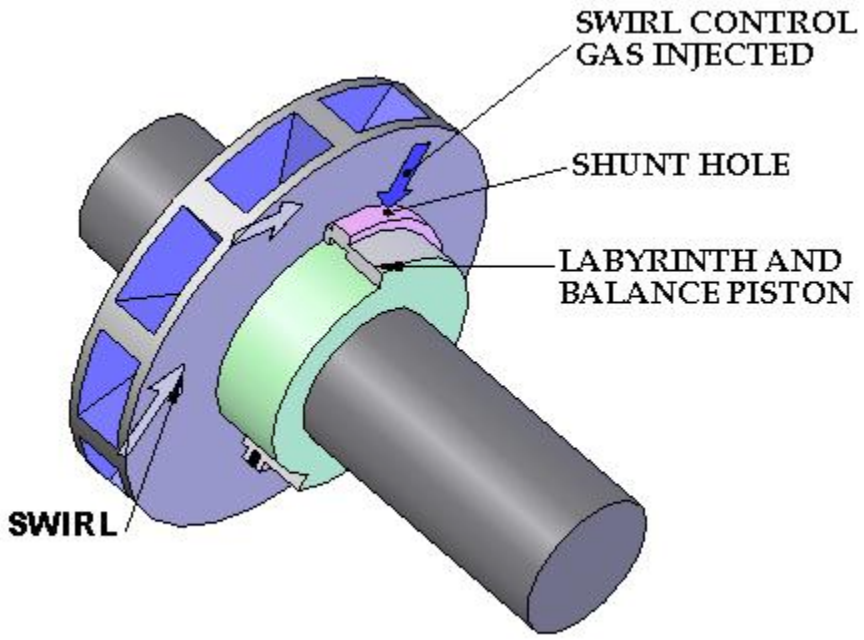

Fig. 6 Shunt hole configuration canceling flow

In the oil and gas sector of the petroleum industry, instability problems can be particularly acute for multistage centrifugal compressors used to inject natural gas into oil wells at pressures ranging from 100 bar (1500 psi) to 700 bar (10000 psi.). The instability problem is economically significant to both compressor manufacturers and users. Usually design changes are required to remedy the problem, and delays of several months are not

unusual. The only protection available today is full-pressure, full-speed factory testing. Thus it is important to predict instability and avoid costly downtime.

LITERATURE REVIEW

Unstable rotor vibrations in centrifugal compressors continue to occur and have caused costly downtime for several large projects. One of the earliest rotor instability vibrations in centrifugal compressors was at Chevron's Kaybob Gas Plant in west central Alberta, Canada in 1971 [5]. Destructive vibration whose frequency was substantially below the running speed of a centrifugal compressors delayed startup. Many minor design changes were tried, but major redesign was finally required, and it took 29 weeks to successfully run at the full speed. Another costly experience involving rotor instability was the Ekofisk case in the Norwegian sector of the North Sea in 1974 [6], where a reinjection compressor of back-to-back design (Fig. 2) could never reach the rated discharge pressure of 625 bar due to excessive subsynchronous rotor vibrations.

Rotordynamic stability of turbomachinery is of continuing interest, particularly predicting and avoiding instabilities. The following elements influence rotor stability: (1) hydrodynamic cross coupling in fluid film bearings, seals, and labyrinths, (2) cross coupling forces from seals in turbines and compressors due to change in clearance, (3) hysteretic or internal friction damping, (4) pulsations, (5) pulsating torque and axial loads, (6) asymmetric shafting, (7) fluid trapped in rotor, (8) stick-slip rubs and chatter, (9) dry friction whip. Of these, the influence of cross coupling impeller forces in pump vibration has gained a special momentum. There are two categories of forces acting on the impeller. One comes from the mechanical system, such as rotor mass unbalance, etc., the other one comes from the working fluid, called fluid-induced forces.

Several sources have been identified as contributing to the fluid-induced forces. One area that has received attention is the force generated by fluid in the annular seals separating the high pressure discharge from the relatively low pressure inlet fluid. Childs [7] developed a general model to define the reaction forces and moments for a long incompressible seal arising from small motion of the seal about its centered position, which is defined in equation (1) as:

$$-\begin{Bmatrix} F_X \\ F_Y \\ M_Y \\ M_X \end{Bmatrix} = \begin{bmatrix} K & k & K_{\varepsilon\alpha} & -k_{\varepsilon\alpha} \\ -k & K & -k_{\varepsilon\alpha} & -K_{\varepsilon\alpha} \\ K_{\alpha\varepsilon} & k_{\alpha\varepsilon} & K_{\alpha} & -k_{\alpha} \\ k_{\alpha\varepsilon} & -K_{\alpha\varepsilon} & k_{\alpha} & K_{\alpha} \end{bmatrix} \begin{Bmatrix} X \\ Y \\ \alpha_Y \\ \alpha_X \end{Bmatrix} + \begin{bmatrix} C & c & C_{\varepsilon\alpha} & -c_{\varepsilon\alpha} \\ -c & C & -c_{\varepsilon\alpha} & -C_{\varepsilon\alpha} \\ C_{\alpha\varepsilon} & c_{\alpha\varepsilon} & C_{\alpha} & -c_{\alpha} \\ c_{\alpha\varepsilon} & -C_{\alpha\varepsilon} & c_{\alpha} & C_{\alpha} \end{bmatrix} \begin{Bmatrix} \dot{X} \\ \dot{Y} \\ \dot{\alpha}_Y \\ \dot{\alpha}_X \end{Bmatrix}$$

$$+ \begin{bmatrix} M & m & M_{\varepsilon\alpha} & -m_{\varepsilon\alpha} \\ -m & M & -m_{\varepsilon\alpha} & -M_{\varepsilon\alpha} \\ M_{\alpha\varepsilon} & m_{\alpha\varepsilon} & M_{\alpha} & -m_{\alpha} \\ m_{\alpha\varepsilon} & -M_{\alpha\varepsilon} & m_{\alpha} & M_{\alpha} \end{bmatrix} \begin{Bmatrix} \ddot{X} \\ \ddot{Y} \\ \ddot{\alpha}_Y \\ \ddot{\alpha}_X \end{Bmatrix}, \qquad (1)$$

where (F_X, F_Y), (X,Y) define the components of the seal reaction forces and relative displacements, and (M_Y, M_X), (α_Y, α_X) define the components of the reaction moments and seal rotation (small yaw and pitch angles) vectors. Elements of the above square matrices in equation (1) are the rotordynamic coefficients. Childs [8] later extended the above model in equation (1) to define force and moment coefficients for pump impellers.

If the moments and the coupling between the forces and rotations, i.e. forces induced by rotations are neglected, then the resultant reduced equations to account only for forces due to displacement perturbations are given as:

$$-\begin{Bmatrix} F_X \\ F_Y \end{Bmatrix} = \begin{bmatrix} K & k \\ -k & K \end{bmatrix} \begin{Bmatrix} X \\ Y \end{Bmatrix} + \begin{bmatrix} C & c \\ -c & C \end{bmatrix} \begin{Bmatrix} \dot{X} \\ \dot{Y} \end{Bmatrix} + \begin{bmatrix} M & m \\ -m & M \end{bmatrix} \begin{Bmatrix} \ddot{X} \\ \ddot{Y} \end{Bmatrix} \qquad (2)$$

Considering the $r-\theta$ polar coordinates are precessing at the precession rate Ω, the reaction-force components in this system are:

$$F_{rq} + jF_{\theta q} = (F_{Xq} + jF_{Yq})e^{-j\Omega t} \qquad (3)$$

Simplifying the algebra in equation (3) gives the comparable results in terms of rotordynamic-coefficients definition of equation (2) as:

$$F_{rq}(\Omega) = -(K + \Omega c - \Omega^2 M)q \qquad (4)$$

$$F_{\theta q}(\Omega) = (k - \Omega C - \Omega^2 m)q\,, \qquad (5)$$

where q is the amplitude of rotor precessional motion.

The tangential force $F_{\theta q}(\Omega)$ in equation (5) is important for stability consideration, as it acts on the rotor in the tangential direction; feeding energy into the

rotor in the direction of rotor precession. The added mass matrix in equation (2) is negligible for gas labyrinth seals in compressors (Childs [2]).

Fulton [9] used test results from Picardo et al. [10] and [11] for labyrinth seals to obtain the effective cross-coupled stiffness Q_{aero}, defined as

$$Q_{aero} = \frac{F_{\theta q}}{g} = k - C\Omega, \qquad (6)$$

where g is the eccentricity, and suggested that the labyrinth effective cross-coupled stiffness model be used to calculate an empirical stability map, which plots mean gas density versus rotor flexibility ratio. He assumed that the destabilizing forces on the rotor are due solely to the tangential forces from the labyrinth seals on the balance piston and impeller eyes, and treated the impeller shroud forces and smaller labyrinths near the casing seals as negligible. He concluded that the labyrinth effective cross-coupled stiffness model suffices to calculate a stability map, and no change is recommended to the currently used API stability map.

A second source of fluid-induced forces for impellers is the hydrodynamic force that arises from the interaction between the impeller and its accompanying volute (Jery et al. [12]). A third area is the hydrodynamic force and moment caused by fluid trapped between the front and back shroud and the stationary casing of the rotating impeller, that is, the forces and moments generated by the shroud leakage flow, and disk friction (Childs [8], and Guinzburg et al.[13]). Hergt and Krieger, [14] measured the force on a centrifugal impeller centered and at various eccentric locations in a vaned diffuser. The measured force was directed radially outward with a small tangential component. Measurements of the unsteady force matrix have been made by Bolleter, et al. [15], from Sulzer Brother, Ltd., Shoji and Ohashi [16], from the University of Tokyo, and the researchers at the California Institute of Technology. Franz and Arndt [17] and Franz, et al. [18] demonstrated that the large shroud clearances reduce the magnitude of the rotordynamic forces for reverse whirl and for the region of destabilizing forward whirl. Bolleter et al. [19] presented the first test results for impellers with tighter clearances between the shroud and the housing.

A bulk-flow model of the leakage path between an impeller shroud and a pump casing was developed by Childs [8]. Rotordynamic coefficient predictions from his

analysis are in reasonable agreement with test results from Bolleter, et al. [19], for direct damping and cross-coupled stiffness coefficients. The model also predicted a resonance phenomenon of the fluid system at inlet tangential velocities higher than approximately half of the impeller tip speed. In this model the clearance between the impeller shroud and pump casing was assumed to be circumferentially symmetric, and the bulk-flow nature of the analysis restricts its applicability to impellers having fairly small clearances between the impeller shroud and casing.

Thomas [20], concerned with instability problems in steam turbines, initially suggested that nonsymmetric clearance caused by eccentric operation of a turbine can create destabilizing forces which he called *spälterregnung* (clearance-excitation) forces. Later Alford [21] identified the same mechanism when analyzing stability problems of aircraft gas turbines; hence, in the United States, excitation forces due to clearance changes around the periphery of a turbine are regularly called "Alford forces". Thomas' and Alford's formula for an unshrouded axial turbine stage is given by:

$$k = \frac{\beta T}{DH} \tag{7}$$

where k is the cross-coupled stiffness, β is the change in the thermodynamic efficiency per unit of rotor displacement, expressed as a fraction of blade height, T is the stage torque, D is the pitch diameter, and H is the vane height.

Wachel and Von Nimitz [22] converted Thomas' and Alford's formula for unshrouded axial turbine to the shrouded impellers for centrifugal compressors and proposed an empirical formula known as Wachel's cross-coupling coefficient [23] to evaluate the destabilizing forces. Wachel's empirical formula to calculate the cross-coupling coefficient k for the single stage in the compressor which includes the effects of eye seal labyrinth, front and back shrouds, and the interstage labyrinth is defined as:

$$k = \frac{(B)(Pwr)(MW)}{(D)(h)(f)} \times \frac{\rho_D}{\rho_S} \tag{8}$$

where,

k = cross-coupled stiffness coefficient, N/m (lb/in)

B = cross coupling constant, 16 SI Units (105 English Units)

Pwr = power, KW (HP)

MW = molecular weight of gas

D = impeller outside diameter, m (in)

h = restrictive dimension in flow path, m (in)

f =speed, Hz

ρ_D = density of fluid at discharge, Kg/m^3 (lb/cu ft)

ρ_S = density of fluid at suction, Kg/m^3 (lb/cu ft)

While Alford's force is caused by the variation of blade tip clearance around an unshrouded axial turbine and is appropriate, Wachel's extended formula is incorrect as there is no comparable blade clearance in the shrouded centrifugal compressor. Therefore, this research on the bulk-flow analysis for rotordynamic coefficients of a shrouded centrifugal compressor impeller aims to develop a more rational alternative for predicting the influence of impeller stages on the rotordynamic stability of shrouded centrifugal compressors. Rotordynamic coefficients are derived separately for both front and back shrouds, eye seal labyrinth, and interstage seal labyrinth, to examine the contribution of each part separately.

Ohashi et al. [24] and Yoshida et al [25] showed that fluid moments on the back shroud of a centrifugal impeller can have destabilizing effects, and stated that Childs' [8] model predicts these coefficients reasonably well. This research on the bulk-flow analysis for rotordynamic coefficients of a shrouded centrifugal compressor impeller investigates the rotordynamic fluid forces and moments on an impeller-shroud with labyrinth seals. Reaction forces and moments are determined for a range of precession frequency, and second order curves are fitted to the results to determine the rotordynamic coefficients of equation (1).

BULK FLOW MATHEMATICAL MODEL FOR SHROUD CLEARANCE FLOW

Childs' [8] governing equations are modified to account for compressibility using real gas properties. As in Childs' [8], and Cao's [26] analysis, these equations are nondimensionalized, and a perturbation expansion of the governing equations in the eccentricity ratio yields a set of zeroth and first-order governing equations.

General Governing Equations

Following the approach taken by Childs [8] using the path coordinate S and circumferential coordinate Rθ, as shown in Fig. 7, to locate a fluid differential element of thickness H(s,θ,t), the governing equations are derived as:

Continuity equation

$$\frac{\partial \rho H}{\partial t}+\frac{\partial(\rho U_S H)}{\partial S}+\frac{1}{R}\frac{\partial(\rho U_\theta H)}{\partial \Theta}+\frac{H}{R}\frac{\partial R}{\partial S}\rho U_S=0 \quad , \tag{9}$$

where U_s and U_θ are the path and circumferential bulk-velocity components, and H is the clearance function.

The *path momentum equation*

$$-H\frac{\partial P}{\partial S}=-\rho H\frac{U_\theta^2}{R}\frac{dR}{dS}+\tau_{ss}+\tau_{sr}+\rho H(\frac{\partial U_S}{\partial t}+\frac{\partial U_S}{\partial \Theta}\frac{U_\theta}{R}+\frac{\partial U_S}{\partial S}U_S). \tag{10}$$

The first subscripts (s,θ) in the shear stress definitions (τ_{ss}, τ_{sr}), ($\tau_{\theta s}$, $\tau_{\theta r}$) denote path and θ directions, respectively; the second subscripts (s,r) denoting stator and rotor surfaces respectively.

The *circumferential momentum equation*

$$-\frac{H}{R}\frac{\partial P}{\partial \Theta}=\tau_{\theta s}+\tau_{\theta r}+\rho H(\frac{\partial U_\theta}{\partial t}+\frac{\partial U_\theta}{\partial \Theta}\frac{U_\theta}{R}+\frac{\partial U_\theta}{\partial S}U_S+\frac{U_\theta U_S}{R}\frac{\partial R}{\partial S}) \quad . \tag{11}$$

An additional governing equation is obtained by using a thermophysical property code to obtain the properties of the working fluid.

The additional equation can simply be stated as:

$$\rho = \rho(P, \overline{T}^0) \tag{12}$$

$$\mu = \mu(P, \overline{T}^0) \tag{13}$$

where ρ is the density, and μ is the viscosity of the working fluid. The above governing equations are the same as Childs' [8], with the equation of state now being dependent on the thermophysical property code. The variation in density of the working fluid is modeled as a function of pressure and a constant temperature only. By providing pressure and temperature to the thermophysical property code, density and viscosity of the working fluid are obtained.

Hir's [27] definitions were used to define the shear stress components of the rotor and stator surfaces. The equations shown below define the shear stress acting on the impeller and its housing. The first subscript in the equations denotes the direction of fluid flow (path and circumferential), and the second subscript refers to the surface (stator and rotor), respectively.

$$\tau_{ss} = \frac{ns}{2}\rho U_S^2 R_\alpha^{ms}[1 + (U_\theta / U_S)^2]^{\frac{ms+1}{2}} \tag{14}$$

$$\tau_{sr} = \frac{nr}{2}\rho U_S^2 R_\alpha^{mr}\{1 + [(U_\theta - R\omega)/U_S]^2\}^{\frac{mr+1}{2}} \tag{15}$$

$$\tau_{\theta s} = \frac{ns}{2}\rho U_\theta U_S R_\alpha^{ms}[1 + (U_\theta / U_S)^2]^{\frac{ms+1}{2}} \tag{16}$$

$$\tau_{\theta r} = \frac{nr}{2}\rho U_S (U_\theta - R\omega) R_\alpha^{mr}\{1 + [(U_\theta - R\omega)/U_S]^2\}^{\frac{mr+1}{2}} \tag{17}$$

where $R_\alpha = 2HU_S / \upsilon$, is the path Reynolds' number. (18)

The empirical coefficients (ns,ms), (nr,mr) account for different surface roughness on the stator and rotor, respectively, and mr = ms = -0.25 and nr = ns = 0.079 account for the smooth impeller.

Similar to Childs' [8] analysis, an assumption is made that the impeller is nominally centered in its housing. Hence, in the centered position, the clearance function H_0 is only a function of the path coordinate S and does not depend on Rθ. The inlet

clearance function $H_0(0)$, the inlet path velocity $U_s(0)$, and the inlet radius R(0) are denoted, respectively, by C_i, V_i, and R_i. In terms of these variables, leakage volumetric flowrate is defined by:

$$\dot{Q} = 2\pi R_i C_i V_i \quad . \tag{19}$$

The length of the leakage path along the impeller face is defined by:

$$L_S = \int_{Z_I}^{Z_I+L} \sqrt{1+\left(\frac{dR}{dZ}\right)^2}\, dz \,. \tag{20}$$

As per Childs' [8], the clearance function between the impeller and the housing is given as:

$$\begin{aligned} H(S,\theta,t) &= H_0(S) - [(X+\alpha_Y Z)\cos\gamma - \alpha_Y R\sin\gamma]\cos\theta \\ &-[(Y-\alpha_X Z)\cos\gamma + \alpha_X R\sin\gamma]\sin\theta \end{aligned} \tag{21}$$

where X and Y gives the displacement of the impeller, α_X and α_Y gives the pitch and yaw rotations of the impeller, and the angle γ shown in Fig. 8 is defined as:

$$\tan\gamma = -\frac{dR}{dZ}, \cos\gamma = \frac{dZ}{dS}, \sin\gamma = -\frac{dR}{dS}. \tag{22}$$

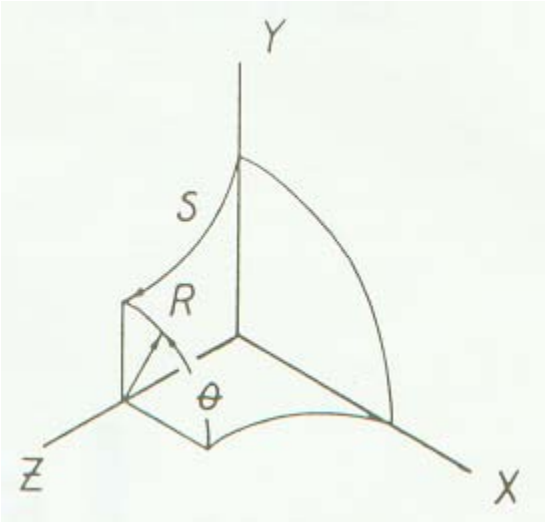

Fig. 7 Impeller surface geometry [8]

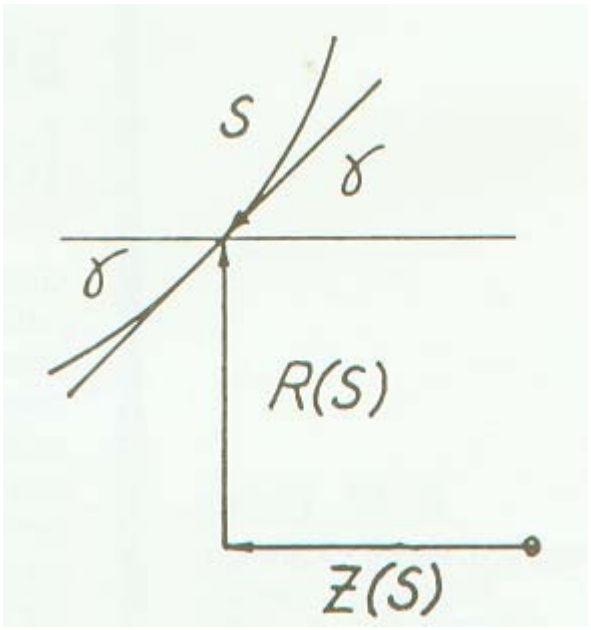

Fig. 8 Local attitude angle of impeller surface [8]

Nondimensionalization and Perturbation Analysis

The governing equations define the bulk-flow velocity components (U_s,U_θ) and the pressure P as a function of the coordinates (Rθ,S) and time, t. They are conveniently nondimensionalized by introducing the following variables:

$$u_s = U_S / V_i, \quad u_\theta = U_\theta / R_i\omega, \quad p = P / \rho_i V_i^2, \quad \tilde{\rho} = \rho / \rho_i$$

$$h = H / C_i, \quad s = S / L_S, \quad r = R / R_i \qquad (23)$$

$$\tau = \omega t, \quad b = V_i / R_i\omega \quad T = L_S / V_i$$

The present analysis examines the changes in (u_s, u_θ, p) due to changes in the clearance function h(θ,s,t) caused by small motion of the impeller within its housing. Perturbation variables used to obtain zeroth and first-order equations are defined as:

$$u_s = u_{s0} + \varepsilon u_{s1}, \; h = h_0 + \varepsilon h_1, \; \tilde{\rho} = \tilde{\rho}_0 + \varepsilon\tilde{\rho}_1 \qquad (24)$$

$$u_\theta = u_{\theta 0} + \varepsilon u_{\theta 1}, \; p = p_0 + \varepsilon p_1$$

where ε is the perturbation coefficient defined as $\varepsilon = e / C_i$.

Zeroth-Order Equations

Zeroth-order equations define the leakage rate and the circumferential and path velocity distributions and pressure distributions for a centered impeller position. The zeroth-order equations are given as:

Continuity equation

$$rh_0 u_{s0} \widetilde{\rho}_0 = 1 . \tag{25}$$

Path-momentum equation

$$-\frac{1}{\widetilde{\rho}_0}\frac{dp_0}{ds} = u_{s0}\frac{du_{s0}}{ds} - \frac{1}{r}\frac{dr}{ds}\left(\frac{u_{\theta 0}}{b}\right)^2 + \frac{(\sigma_s + \sigma_r)}{2}u_{s0}^2 \quad . \tag{26}$$

Circumferential-momentum equation

$$2\frac{du_{\theta 0}}{ds} + 2\frac{u_{\theta 0}}{r}\frac{dr}{ds} + [\sigma_r(u_{\theta 0} - r) + \sigma_s u_{\theta 0}] = 0 \tag{27}$$

where the quantities σ_s and σ_r are defined as

$$\sigma_s = (L_s / H_0)\lambda_s ,\ \sigma_r = (L_s / H_0)\lambda_r \tag{28}$$

where λ_s and λ_r are dimensionless stator and rotor friction factors defined by

$$\lambda_s = nsR_{\alpha 0}^{ms}[1 + (u_{\theta 0} / bu_{s0})^2]^{\frac{ms+1}{2}} , \tag{29}$$

$$\lambda_r = nrR_{\alpha 0}^{mr}\{1 + [(u_{\theta 0} - r) / bu_{s0}]^2\}^{\frac{mr+1}{2}} . \tag{30}$$

For a known flowrate, the continuity equation (25) completely defines u_{s0} to obtain

$$\frac{du_{s0}}{ds} = -u_{s0}\left[\frac{1}{h_0}\frac{dh_0}{ds} + \frac{1}{\widetilde{\rho}_0}\frac{d\widetilde{\rho}_0}{ds} + \frac{1}{r}\frac{dr}{ds}\right]. \tag{31}$$

This equation when substituted into the zeroth order path-momentum equation (26) yields

$$-\frac{1}{\widetilde{\rho}_0}\frac{dp_0}{ds} = -u_{s0}^2\left[\frac{1}{h_0}\frac{dh_0}{ds} + \frac{1}{\widetilde{\rho}_0}\frac{d\widetilde{\rho}_0}{ds} + \frac{1}{r}\frac{dr}{ds}\right] - \frac{1}{r}\frac{dr}{ds}\left(\frac{u_{\theta 0}}{b}\right)^2 + \frac{(\sigma_s + \sigma_r)}{2}u_{s0}^2 \quad . \tag{32}$$

Thus the governing zeroth-order equations are now reduced to two governing equations consisting of equations (27) and (32). Density $\tilde{\rho}_0$ is obtained by the equation of state (12) which is solely a function of pressure and temperature.

Equations (27) and (32) are coupled and nonlinear and are solved iteratively. The initial condition for the circumferential velocity $u_{\theta 0}(0)$ is obtained from the exit flow condition of the impeller. The inlet and discharge pressure of the impeller are known and serve, respectively, as the exit (P_e) and supply (P_s) pressures for the leakage flow along the impeller face. The inlet condition for p_0 is obtained from the inlet boundary condition (s=0) given by inlet pressure drop as:

$$P_S - P_0(0,\theta,t) = \rho(1+\xi)U_{S0}^2(0,\theta,t)/2\,, \tag{33}$$

where ξ is the inlet loss coefficient. From the above relationship, the zeroth-order pressure relationship is obtained as:

$$p_0(0) = P_s/\rho_i V_i^2 - (1+\xi)u_{s0}^2(0)/2\,. \tag{34}$$

The solution to the zeroth-order equations (27) and (32) are obtained iteratively since all of the coefficients depend on the local path velocity U_{s0}. An initial (s=0) fluid velocity V_i is estimated which then defines $u_{s0}(s)$. A specified $u_{\theta 00}(0)$ and the calculated p_0 from equation (34) are used to numerically integrate the zeroth-order equations (27) and (32) from the path entrance (s=0), to the path exit (s=1). The exit labyrinth seal at the leakage path exit also provides restriction, yielding a relationship of the form

$$P(L_S,\theta,t) - P_e = \frac{\rho}{2} C_{de} U_S^2(L_S,\theta,t)\,, \tag{35}$$

where C_{de} is the discharge coefficient , obtained by using the leakage rate through the labyrinth seal. The leakage through the labyrinth seal of the compressor is calculated using a labyrinth seal code developed by Childs and Scharrer [28], and this value is used to calculate the discharge coefficient at specific impeller operating conditions. The seal leakage code uses the geometry of the seal and the operating conditions, i.e. inlet and exit pressures, temperature, viscosity, density, etc. to calculate the leakage rate through the seal. Several discharge coefficients are tested in the model to match the flow rate through the impeller leakage path and the flow rate through the seal. Once the two flow rates converged, the resulting C_{de} is used in the model as an exit restriction boundary condition.

Based on the difference between a calculated exit pressure and the prescribed exit pressure, a revised value of V_i is calculated, and the procedure is repeated until convergence is achieved between the prescribed and the calculated exit pressure.

First-Order Equations

The first-order equations define the perturbations in the velocity and pressure distributions due to either a radial-displacement perturbation or a tilt perturbation of the impeller. Integration of the perturbed pressure and shear-stress distribution acting on the rotor yields the reaction forces and moments acting on the impeller face.

First order equations obtained by the perturbation expansion of equations (9), (10) and (11) are:

Continuity equation

$$\frac{\partial(\tilde{\rho}_0 h_1)}{\partial\tau}+\frac{\partial(h_0\tilde{\rho}_1)}{\partial\tau}+\frac{1}{\omega T}\left[\frac{\partial(\tilde{\rho}_0 h_0 u_{s1}+\tilde{\rho}_0 h_1 u_{s0}+\tilde{\rho}_1 h_0 u_{s0})}{\partial s}\right]$$
$$+\frac{1}{r}\left[\frac{\partial(\tilde{\rho}_0 u_{\theta 0} h_1+\tilde{\rho}_0 u_{\theta 1} h_0+\tilde{\rho}_1 u_{\theta 0} h_0)}{\partial\theta}\right]+\frac{1}{\omega T}\frac{dr}{rds}(u_{s0}\tilde{\rho}_0 h_1+u_{s1}\tilde{\rho}_0 h_0+u_{s0}\tilde{\rho}_1 h_0)=0 \tag{36}$$

Path momentum equation

$$-h_0\frac{\partial p_1}{\partial s}--h_1\frac{\partial p_0}{\partial s}=\frac{1}{b^2}\left[-u_{\theta 0}^2\left(\frac{\tilde{\rho}_1 h_0}{r}\frac{dr}{ds}+\frac{\tilde{\rho}_0 h_1}{r}\frac{dr}{ds}\right)-\frac{2\tilde{\rho}_0 h_0}{r}\frac{dr}{ds}u_{\theta 0}u_{\theta 1}\right]+\frac{L_s}{C_i\rho_i V_i^2}(\tau_{ss1}+\tau_{sr1})$$
$$+\omega L_s\tilde{\rho}_0 h_0\left[\frac{1}{V_i}\frac{\partial u_{s1}}{\partial\tau}+\frac{u_{\theta 0}}{rV_i}\frac{\partial u_{s1}}{\partial\theta}+\frac{u_{\theta 1}}{rV_i}\frac{\partial u_{s0}}{\partial\theta}+\frac{1}{\omega L_s}\left(u_{s0}\frac{\partial u_{s1}}{\partial s}+u_{s1}\frac{\partial u_{s0}}{\partial s}\right)\right] \tag{37}$$
$$+\frac{(\tilde{\rho}_0 h_1+\tilde{\rho}_1 h_0)L_s}{V_i}\left[\omega\frac{\partial u_{s0}}{\partial\tau}+\frac{\omega u_{\theta 0}}{r}\frac{\partial u_{s0}}{\partial\theta}+\frac{V_i u_{s0}}{L_s}\frac{\partial u_{s0}}{\partial s}\right]$$

where τ_{ss1} and τ_{sr1} are shear stress perturbation definitions.

Circumferential momentum equation

$$\begin{aligned}
&\tilde{\rho}_0 h_0 u_{s0}\frac{\partial u_{\theta 1}}{\partial s}+\tilde{\rho}_0 h_0 u_{s1}\frac{\partial u_{\theta 0}}{\partial s}+\tilde{\rho}_0 h_1 u_{s0}\frac{\partial u_{\theta 0}}{\partial s}+\tilde{\rho}_1 h_0 u_{s0}\frac{\partial u_{\theta 0}}{\partial s}+\frac{T\omega}{r}\tilde{\rho}_0 h_0 u_{\theta 0}\frac{\partial u_{\theta 1}}{\partial \theta}\\
&+\frac{T\omega}{r}\tilde{\rho}_0 h_0 u_{\theta 1}\frac{\partial u_{\theta 0}}{\partial \theta}+\frac{T\omega}{r}\tilde{\rho}_0 h_1 u_{\theta 0}\frac{\partial u_{\theta 0}}{\partial \theta}+\frac{T\omega}{r}\tilde{\rho}_1 h_0 u_{\theta 0}\frac{\partial u_{\theta 0}}{\partial \theta}+\omega T\tilde{\rho}_0 h_0\frac{\partial u_{\theta 1}}{\partial \tau}\\
&+\omega T\tilde{\rho}_0 h_1\frac{\partial u_{\theta 0}}{\partial \tau}+\omega T\tilde{\rho}_1 h_0\frac{\partial u_{\theta 0}}{\partial \tau}+\frac{\tilde{\rho}_0 h_0 u_{\theta 0}u_{s1}}{r}\frac{dr}{ds}+\frac{\tilde{\rho}_0 h_0 u_{\theta 1}u_{s0}}{r}\frac{dr}{ds}+\frac{\tilde{\rho}_0 h_1 u_{\theta 0}u_{s0}}{r}\frac{dr}{ds}\\
&+\frac{\tilde{\rho}_1 h_0 u_{\theta 0}u_{s0}}{r}\frac{dr}{ds}+\frac{T\tau_{\theta s1}}{\rho_i C_i R_i \omega}+\frac{T\tau_{\theta r1}}{\rho_i C_i R_i \omega}=\frac{-Tb^2\omega h_0}{r}\frac{\partial p_1}{\partial \theta}-\frac{Tb^2\omega h_1}{r}\frac{\partial p_0}{\partial \theta}
\end{aligned} \tag{38}$$

The dependency of $\tilde{\rho}$ with respect to s, τ, and θ in equations (36), (37) and (38) are eliminated by considering the following equation of state:

$$\frac{\partial \tilde{\rho}_1}{\partial s}=\frac{d\tilde{\rho}_1}{dp_1}\frac{\partial p_1}{\partial s},\ \frac{\partial \tilde{\rho}_1}{\partial \tau}=\frac{d\tilde{\rho}_1}{dp_1}\frac{\partial p_1}{\partial \tau},\ \frac{\partial \tilde{\rho}_1}{\partial \theta}=\frac{d\tilde{\rho}_1}{dp_1}\frac{\partial p_1}{\partial \theta}. \tag{39}$$

Since the temperature is considered constant, the density is only a function of pressure. The perturbed clearance function h_1 can be stated from equations (21) and (23) as

$$\begin{aligned}
\varepsilon h_1 &=\left\{-\left[x+\alpha_Y\left(\frac{L}{C_i}\right)z\right]\cos\gamma+\alpha_Y\left(\frac{R_i}{C_i}\right)r\sin\gamma\right\}\cos\theta\\
&+\left\{-\left[y-\alpha_X\left(\frac{L}{C_i}\right)z\right]\cos\gamma-\alpha_X\left(\frac{R_i}{C_i}\right)r\sin\gamma\right\}\sin\theta\\
&=h_{1c}(s,\tau)\cos\theta+h_{1s}(s,\tau)\sin\theta.
\end{aligned} \tag{40}$$

Following Childs' [8] approach, the theta dependency of the dependent variables is eliminated by assuming the following, comparable solution format to the perturbed clearance function

$$u_{s1}=u_{s1c}\cos\theta+u_{s1s}\sin\theta,\ u_{\theta 1}=u_{\theta 1c}\cos\theta+u_{\theta 1s}\sin\theta,\ p_1=p_{1c}\cos\theta+p_{1s}\sin\theta \tag{41}$$

Substituting these into equations (36), (37) and (38) and equating like coefficients of cosθ and sinθ yields six equations in the independent variables s, τ. By introducing the complex variables

$$\underline{u}_{s1}=u_{s1c}+ju_{s1s},\ \underline{u}_{\theta 1}=u_{\theta 1c}+ju_{\theta 1s},\ \underline{p}_1=p_{1c}+jp_{1s},\ \underline{h}_1=h_{1c}+jh_{1s}, \tag{42}$$

the six real equations can be reduced to three complex equations. Further simplification can be made by using the following definitions provided by Childs' [8]

$$\varepsilon \underline{h}_1 = -q\left(\frac{L}{L_s}\right)\frac{dz}{ds} - \alpha G_0 \tag{43}$$

where $q = x + jy$, $\alpha = \alpha_Y - j\alpha_X$, (44)

and $G_0 = \left(\frac{L^2}{C_i L_s}\right) z\frac{dz}{ds} + \left(\frac{R_i^2}{C_i L_s}\right) r\frac{dr}{ds}$ (45)

From equation (43) the following result is obtained:

$$\varepsilon \frac{\partial h_1}{\partial s} = -q\left(\frac{L}{L_s}\right)\frac{d^2 z}{ds^2} - \alpha F_1 \tag{46}$$

where F_1 is defined in Appendix A.

The time dependency of equations (36), (37) and (38) can be eliminated by assuming harmonic seal motion of the form

$$q = q_0 e^{jf\tau},\ \alpha = \alpha_0 e^{jf\tau},\ h_1 = h_{10} e^{jf\tau},\ f = \Omega/\omega \tag{47}$$

where Ω is the seal precession frequency, and q_0 and α_0 are real constants. The associated harmonic solution can then be stated as

$$\underline{u}_{s1} = \bar{u}_{s1} e^{jf\tau},\ \underline{u}_{\theta 1} = \bar{u}_{\theta 1} e^{jf\tau},\ \underline{p}_1 = \bar{p}_1 e^{jf\tau}. \tag{48}$$

Substitution from equations (43-48) into the governing partial differential equations (36-38) yields the following three complex ordinary differential equations in s

- *Continuity equation*

$$\begin{aligned} &\frac{d\bar{u}_{s1}}{ds} + \frac{u_{s0}}{\tilde{\rho}_0 k_1}\left(\frac{d\bar{p}_1}{ds}\right) + \bar{u}_{s1}(A_{6S}) + \bar{u}_{\theta 1}\left(\frac{-j\omega\Pi}{r}\right) + \\ &\bar{p}_1\left(\frac{j\Pi\Gamma}{\tilde{\rho}_0 k_1} - \frac{u_{s0}}{\tilde{\rho}_0^2 k_1}\frac{d\tilde{\rho}_0}{ds}\right) - \bar{p}_1\left(\frac{-j\Pi\Gamma}{h_0} - \frac{u_{s0}}{\tilde{\rho}_0 h_0}\frac{d\tilde{\rho}_0}{ds} - \frac{u_{s0}}{h_0 r}\frac{dr}{ds} - \frac{1}{h_0}\frac{du_{s0}}{ds}\right) = \frac{dh_1}{ds}\left(\frac{-u_{s0}}{h_0}\right) \end{aligned} \tag{49}$$

- *Path-momentum equation*

$$\frac{d\bar{p}_1}{ds} + \tilde{\rho}_0 u_{s0}\frac{d\bar{u}_{s1}}{ds} + \bar{u}_{s1}\left(j\tilde{\rho}_0\Pi\Gamma + \tilde{\rho}_0 A_{3S}\right) + \bar{u}_{\theta 1}\left(\tilde{\rho}_0 A_{2S}\right) + \bar{p}_1\left(A_{4S}\right) = h_1\tilde{\rho}_0 A_{1S}. \tag{50}$$

- *Circumferential-momentum equation*

$$\frac{d\overline{u}_{\theta 1}}{ds}+\overline{u}_{s1}\left(\frac{A_{3\theta}}{u_{s0}}\right)+\overline{u}_{\theta 1}\left(\frac{j\Pi\Gamma}{u_{s0}}+\frac{A_{2\theta}}{u_{s0}}\right)+\overline{p}_1\left(\frac{-jbL_s}{rR_i\widetilde{\rho}_0u_{s0}}+\frac{A_{4\theta}}{2\widetilde{\rho}_0k_1}\right)=h_1\left(\frac{A_{1\theta}}{u_{s0}}\right) \quad (51)$$

where A_{iS} and $A_{i\theta}$ coefficients are defined in the Appendix A.

Further simplification leads to the resulting matrix equation

$$\frac{d}{ds}\begin{Bmatrix}\overline{u}_{s1}\\ \overline{u}_{\theta 1}\\ \overline{p}_1\end{Bmatrix}+[A]\begin{Bmatrix}\overline{u}_{s1}\\ \overline{u}_{\theta 1}\\ \overline{p}_1\end{Bmatrix}=\left(\frac{q_0}{\varepsilon}\right)\begin{Bmatrix}g_1\\ g_2\\ g_3\end{Bmatrix}+\left(\frac{\alpha_0}{\varepsilon}\right)\begin{Bmatrix}g_4\\ g_5\\ g_6\end{Bmatrix} \quad (52)$$

where

$$[A]=\begin{bmatrix} A_{6S}/A_{5S}-\dfrac{u_{so}}{k_1A_{5S}}(A_{3S}+j\Pi\Gamma) & \dfrac{-j\omega\Gamma}{rA_{5s}}-\dfrac{u_{s0}A_{2S}}{k_1A_{5S}} & \dfrac{j\Pi\Gamma}{\widetilde{\rho}_0k_1A_{5S}}-\dfrac{u_{s0}A_{4S}}{\widetilde{\rho}_0k_1A_{5S}}-\dfrac{u_{s0}}{\widetilde{\rho}_0^2k_1A_{5S}}\dfrac{d\widetilde{\rho}_0}{ds}\\ \dfrac{A_{3\theta}}{u_{s0}} & \dfrac{A_{2\theta}+j\Pi\Gamma}{u_{s0}} & \dfrac{A_{4\theta}}{2\widetilde{\rho}_0k_1}-\dfrac{jbL_s}{ru_{s0}\widetilde{\rho}_0R_i}\\ \dfrac{\widetilde{\rho}_0A_{3S}}{A_{5S}}-\dfrac{\widetilde{\rho}_0u_{s0}A_{6S}}{A_{5S}}+\dfrac{j\widetilde{\rho}_0\Pi\Gamma}{A_{5S}} & \dfrac{\widetilde{\rho}_0A_{2S}}{A_{5S}}+\dfrac{j\omega\Pi u_{s0}\widetilde{\rho}_0}{rA_{5S}} & \dfrac{A_{4S}}{A_{5S}}+\dfrac{u_{s0}^2}{\widetilde{\rho}_0A_{5S}k_1}\dfrac{d\widetilde{\rho}_0}{ds}-\dfrac{j\Pi\Gamma u_{s0}}{A_{5S}k_1}\end{bmatrix} \quad (53)$$

$$\begin{Bmatrix}g_1\\ g_2\\ g_3\end{Bmatrix}=\left(\frac{L}{L_S}\right)\begin{Bmatrix}\dfrac{F_2}{A_{5S}}+\dfrac{j\Pi\Gamma}{h_0A_{5S}}\dfrac{dz}{ds}+A_{1S}\dfrac{u_{s0}}{k_1A_{5S}}\dfrac{dz}{ds}\\ \dfrac{-A_{1\theta}}{u_{s0}}\dfrac{dz}{ds}\\ \dfrac{-A_{1S}\widetilde{\rho}_0}{A_{5S}}\dfrac{dz}{ds}-\dfrac{u_{s0}F_2\widetilde{\rho}_0}{A_{5S}}-\dfrac{ju_{s0}\Gamma\Pi\widetilde{\rho}_0}{h_0A_{5S}}\dfrac{dz}{ds}\end{Bmatrix} \quad (54)$$

$$\begin{Bmatrix}g_4\\ g_5\\ g_6\end{Bmatrix}=\begin{Bmatrix}\dfrac{F_3}{A_{5S}}+\dfrac{jG_0\Gamma\Pi}{h_0A_{5S}}+\dfrac{G_0A_{1S}u_{s0}}{k_1A_{5S}}\\ \dfrac{-A_{1\theta}G_0}{u_{s0}}\\ \dfrac{-G_0A_{1S}\widetilde{\rho}_0}{A_{5S}}-\dfrac{u_{s0}F_3\widetilde{\rho}_0}{A_{5S}}-\dfrac{jG_0u_{s0}\Gamma\Pi\widetilde{\rho}_0}{h_0A_{5S}}\end{Bmatrix}. \quad (55)$$

Elements used in equations (53-55) can be found in appendix A. In the system matrix [A] in equation (53), the centrifugal acceleration term $\frac{2u_{\theta 0}}{b^2 r}\frac{dr}{ds}$ from the A_{2S} definition of Appendix A, is of the order of 10^5, while some terms in the matrix are of the order of 10^{-3}. This centrifugal acceleration term $\frac{2u_{\theta 0}}{b^2 r}\frac{dr}{ds}$ makes the system of equations stiff as there are three different scale first-order differential equations, and stiffness occurs in a problem where there are two or more very different scales of the independent variable on which the dependent variables are changing. These very different scales of the independent variables make the system of equations stiff and costly in computation with ordinary Runge-Kutta method or Predictor-Corrector methods. Therefore crucial to the success of a stiff integration scheme is an automatic stepsize adjustment algorithm and thus a multi-step automatic stepsize adjustment integrator is used. For better stability a user-supplied jacobian matrix obtained by analytic differentiation of the right hand side of equations $y' = f(s)$ is used instead of computing it by numerical differencing with appropriate increments in s. Further details in stiff integrators are given in [29].

Boundary Conditions

Three nondimensional first-order boundary conditions are given, and the first of these is that the entrance loss is defined by equation (34), and the corresponding perturbation-variable relationship is:

$$\overline{p}_1(0) = -\frac{(1+\xi)\overline{u}_{s1}(0)\widetilde{\rho}_0(0)}{\left(1+\frac{(1+\xi)}{2}\left.\frac{d\widetilde{\rho}}{dp}\right|_1\right)} \quad . \tag{56}$$

The relationship at the exit is provided by equation (35) and yields the following perturbation relationship:

$$\overline{p}_1(1) = -\frac{C_{de}\widetilde{\rho}_0(1)u_{s0}(1)\overline{u}_{s1}(1)}{\left(1+\frac{C_{de}u_{s0}^2(1)}{2}\left.\frac{d\widetilde{\rho}}{dp}\right|_1\right)} \quad . \tag{57}$$

Additionally, the entrance-perturbation, circumferential velocity is zero; i.e. the impeller motion does not perturb the inlet circumferential velocity, which can be stated as:

$$u_{\theta 1}(0) = 0 . \tag{58}$$

These first order complex differential equations (52) can be solved by using a transition-matrix approach, while satisfying the boundary conditions of equations (56-58). Using the same procedure followed by Childs' [8], the homogenous version of equations (52) are solved successively with the initial conditions (1,0,0), (0,1,0), (0,0,1) to obtain the transition matrix $[\Phi(f,s)]$. The particular solution is then solved for zero initial conditions. Further details of the solution can be found in Childs' [2]. The solution to equations (52), due to displacement perturbation, is obtained by setting $\alpha_0 = 0$, and can be stated as:

$$\begin{Bmatrix} \bar{u}_{s1} \\ \bar{u}_{\theta 1} \\ \bar{p}_1 \end{Bmatrix} = \left(\frac{q_0}{\varepsilon} \right) \begin{Bmatrix} f_{1c} + jf_{1s} \\ f_{2c} + jf_{2s} \\ f_{3c} + jf_{3s} \end{Bmatrix} = \left(\frac{q_0}{\varepsilon} \right) \begin{Bmatrix} f_1 \\ f_2 \\ f_3 \end{Bmatrix} . \tag{59}$$

The solution due to angular perturbations is obtained by setting $q_0 = 0$ and can be stated as:

$$\begin{Bmatrix} \bar{u}_{s1} \\ \bar{u}_{\theta 1} \\ \bar{p}_1 \end{Bmatrix} = \left(\frac{\alpha_0}{\varepsilon} \right) \begin{Bmatrix} f_{4c} + jf_{4s} \\ f_{5c} + jf_{5s} \\ f_{6c} + jf_{6s} \end{Bmatrix} = \left(\frac{\alpha_0}{\varepsilon} \right) \begin{Bmatrix} f_4 \\ f_5 \\ f_6 \end{Bmatrix} . \tag{60}$$

After the perturbations in pressure and shear stress are known by solving the governing equations, the perturbed pressure and shear-stress distribution acting on the impeller are integrated to yield the reaction forces and moments. The integral equations and the corresponding definitions for obtaining the reaction forces and moments are given in Childs' [8]. Rotordynamic coefficients are obtained by carrying out a least-square curve fit for the reaction forces and moments due to displacement and slope perturbations.

Rotordynamic coefficients for displacement perturbations:

$$f_{rq}(f) = \frac{F_r(f)}{q_0 F_0} = -(\tilde{K} + f\tilde{c} - f^2\tilde{M})$$

$$f_{\theta q}(f) = \frac{F_\theta(f)}{q_0 F_0} = (\tilde{k} - f\tilde{C} - f^2\tilde{m}) \tag{61}$$

$$m_{dq}(f) = \frac{M_d(f)}{q_0 F_0 L} = -(\tilde{K}_{\alpha\varepsilon} + f\tilde{c}_{\alpha\varepsilon} - f^2\tilde{M}_{\alpha\varepsilon})$$

$$-m_{tq}(f) = \frac{M_t(f)}{q_0 F_0 L} = (\tilde{k}_{\alpha\varepsilon} - f\tilde{C}_{\alpha\varepsilon} - f^2\tilde{m}_{\alpha\varepsilon})$$

Rotordynamic coefficients for slope perturbations:

$$f_{r\alpha}(f) = \frac{F_r(f)}{\alpha_0 F_0} = -(\tilde{K}_{\varepsilon\alpha} + f\tilde{c}_{\varepsilon\alpha} - f^2\tilde{M}_\alpha)$$

$$f_{\theta\alpha}(f) = \frac{F_\theta(f)}{\alpha_0 F_0} = (\tilde{k}_{\varepsilon\alpha} - f\tilde{C}_{\varepsilon\alpha} - f^2\tilde{m}_{\varepsilon\alpha}) \tag{62}$$

$$-m_{d\alpha}(f) = \frac{-M_d(f)}{\alpha_0 F_0 L} = (\tilde{K}_\alpha + f\tilde{c}_\alpha - f^2\tilde{M}_\alpha)$$

$$-m_{t\alpha}(f) = -\frac{M_t(f)}{\alpha_0 F_0 L} = (\tilde{k}_\alpha - f\tilde{C}_\alpha - f^2\tilde{m}_\alpha)$$

All the above are defined in Childs [8].

VALIDATIONS

A check on the validity of the program was made by comparing the numerical results to the experimental results by Yoshida et al. [25]. Yoshida et al. made flow and pressure measurements in the back shroud/casing clearance of a precessing centrifugal impeller. They integrated the unsteady pressure distribution between the radii r=47.5mm and r=165mm to obtain the fluid moment on the precessing impeller shroud for nondimensional precessing frequency ratio Ω/ω ranging from -1.4 to 1.4. The leakage flow in the back shroud clearance was radially inward. Since the seal data is unknown, but the leakage rate is known; initial path velocity Vi is calculated by using the given leakage rate.

Three important unsteady boundary conditions in this analysis are: the entrance loss was defined by equation (34), and the corresponding perturbation-variable relationship was defined in equation (56). This boundary condition assumes that there is leakage occurring, i.e. the path velocity u_S is non-zero. Tsujimoto et al. [30] used zero-leakage rate, which results in zero pressure fluctuation (p_1=0) by equation (56), and made a comparison between the theoretical predictions and the experimental results. They showed that for zero-leakage rate, the predicted moments were significantly smaller than the measured moments. With non zero leakage rate, the pressure fluctuation p_1 is never zero; thus, zero inlet pressure perturbation condition would not occur. This boundary condition is very similar to the boundary condition used by Tsujimoto et al. [30], except that it is valid only for non-zero leakage rate.

Since the leakage flow exits to a relatively large space without flow restriction, it is assumed to have zero pressure loss at the exit. This yields the exit boundary condition as:

$$P(L_S,\theta,t) - P_e = 0 \tag{63}$$

Taking the perturbation of equation (63) gives the exit perturbed pressure as:

$$\bar{p}_1(1) = 0 \tag{64}$$

As stated in equation (58), the entrance-perturbation circumferential velocity is zero. The impeller data and operating conditions are given in Table 1. Fig. 9 shows the impeller geometry for this test.

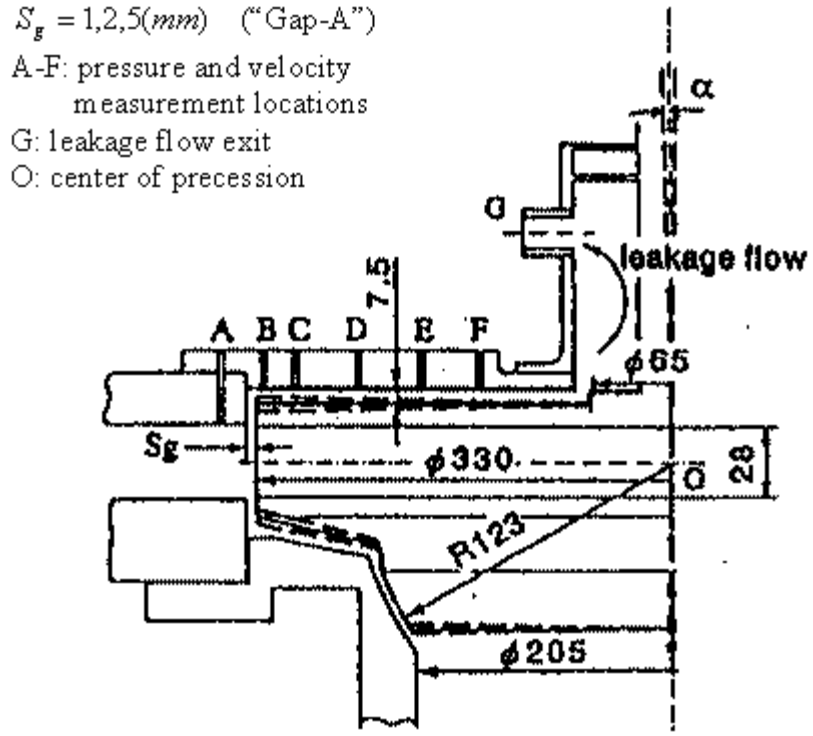

Fig. 9 Basic test impeller geometry [21]

Table 1 Geometry and operating conditions of the test

Supply pressure P_s (s=0)	1.1375 bar
Exit pressure P_e (s=1)	1.1329 bar
Running speed	677 rpm
Temperature	305 K
Working fluid	Air
Inlet tangential velocity ratio $u_{\theta 0}$	0.5
Leakage flow rate	3.0036×10^{-3} m^3/sec
Impeller outlet height b_2	28 mm
Impeller outer radius R_i	165 mm
Shroud casing clearance	7.5 mm

The following reduced model from equation (1) was used to define the reaction moments:

$$\begin{Bmatrix} M_X \\ M_Y \end{Bmatrix} = -\begin{bmatrix} M_\alpha & m_\alpha \\ -m_\alpha & M_\alpha \end{bmatrix} \begin{Bmatrix} \ddot{\alpha}_X \\ \ddot{\alpha}_Y \end{Bmatrix} - \begin{bmatrix} C_\alpha & c_\alpha \\ -c_\alpha & C_\alpha \end{bmatrix} \begin{Bmatrix} \dot{\alpha}_X \\ \dot{\alpha}_Y \end{Bmatrix} - \begin{bmatrix} K_\alpha & k_\alpha \\ -k_\alpha & K_\alpha \end{bmatrix} \begin{Bmatrix} \alpha_X \\ \alpha_Y \end{Bmatrix} \tag{65}$$

where M_α is the direct added inertia, C_α is the direct damping, K_α is the direct stiffness, m_α is the cross-coupled inertia, c_α is the cross coupled damping and k_α is the cross-coupled stiffness. Equation (65) is nondimensionalized by $I\omega^2$, where I is the moment of inertia of hypothetical fluid disk of thickness b_2 (Fig. 10) and radius R_i around the diameter, and is given as:

$$I = \rho\pi R_i^2 b_2 i^2 \tag{66}$$

where i is the radius of gyration:

$$i = \sqrt{R_i^2/4 + b_2^2/12} \quad . \tag{67}$$

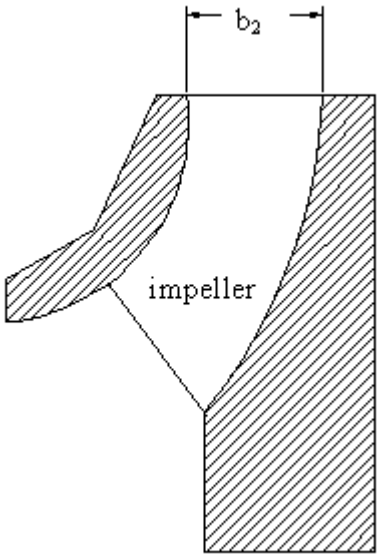

Fig. 10 Impeller outlet height

In this study, the geometrical condition around the impeller is symmetric, and therefore the nondimensional fluid moment is represented with its nondimensional transverse (m_t) and nondimensional direct (m_d) components as:

$$m_t = \left[\frac{m_\alpha}{I} \left(\frac{\Omega}{\omega} \right)^2 + \frac{C_\alpha}{I\omega} \left(\frac{\Omega}{\omega} \right) - \frac{k_\alpha}{I\omega^2} \right] \alpha \tag{68}$$

$$m_d = \left[\frac{M_\alpha}{I} \left(\frac{\Omega}{\omega} \right)^2 - \frac{c_\alpha}{I\omega} \left(\frac{\Omega}{\omega} \right) - \frac{K_\alpha}{I\omega^2} \right] \alpha \tag{69}$$

where the rotation vector α is related to the yaw and pitch angles (α_Y, α_X) by

$$\alpha_X = -\alpha \sin \Omega t \tag{70}$$

$$\alpha_Y = \alpha \cos \Omega t \, . \tag{71}$$

By using the leakage flow coefficient ϕ_l=8.85x10^{-3}, and gap between impeller side plate and casing S_g=2mm, rotordynamic coefficients were predicted using the compressible code. Leakage flow coefficient ϕ_l is defined as,

$$\phi_l = \text{volumetric leakage flow rate} / 2\pi R_i^2 b_2 \omega \, . \tag{72}$$

Table 2 gives the comparison of the measured results [25] to the calculated results for different inlet loss coefficient ξ. Figs. 11 and 12 show the comparison for the transverse moment coefficients, and Figs. 13 and 14 show the comparison for the direct moment coefficients for different inlet loss coefficient ξ. A moment-only whirl frequency ratio f_{wM} is useful in characterizing stability due to slope perturbations and is defined as:

$$f_{wM} = \frac{k_\alpha}{C_\alpha \omega} \, . \tag{73}$$

Table 2 Comparison of theory versus measured results for different ξ

Coefficients	Measured	Theory ξ=0.1	Theory ξ=0.3	Theory ξ=1.1	Theory ξ=1.5
M_α (Kgm^2)	0.32x10^{-3}	0.430x10^{-3}	0.428x10^{-3}	0.419x10^{-3}	0.414x10^{-3}
m_α (Kgm^2)	0.41x10^{-5}	0.12x10^{-4}	0.15x10^{-4}	0.25x10^{-4}	0.30x10^{-4}
C_α (NmS/rad)	0.022	0.009	0.011	0.016	0.019
c_α (NmS/rad)	0.016	0.049	0.049	0.048	0.048
K_α (Nm/rad)	0.258	-1.835	-1.870	-2.033	-2.132
k_α (Nm/rad)	1.016	0.811	0.904	1.276	1.460
f_{wM}	0.651	1.27	1.159	1.125	1.08

Table 2 shows that at lower values of inlet loss coefficient ξ, a close match is obtained between the prediction and measurement for the cross-coupled stiffness k_α. The calculated direct damping C_α is small compared to the measured coefficient at lower values of ξ, but the prediction improves at unrealistic high inlet loss coefficient ξ. The moment-only whirl frequency ratio f_{wM} decreases with increasing ξ. The calculated moment-only whirl frequency ratio f_{wM} is higher and is thus more destabilizing. Thus at lower values of ξ, the predicted moments are more destabilizing than the measured moments. Fig. 12 shows that the predicted transverse moment is sensitive to the inlet loss coefficient ξ. Figs. 11 and 12 show that the predictions match closely for the measured transverse moment especially at higher ξ. Fig.12 shows the predicted direct moment to be insensitive to ξ; thus the direct mass M_α, and direct stiffness K_α does not change with increasing ξ.

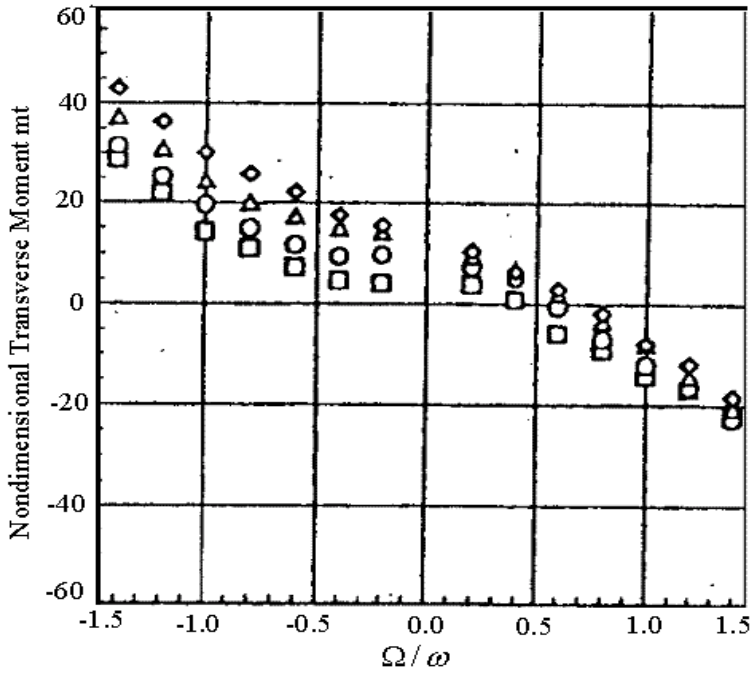

Fig. 11 Measured transverse moment [25]

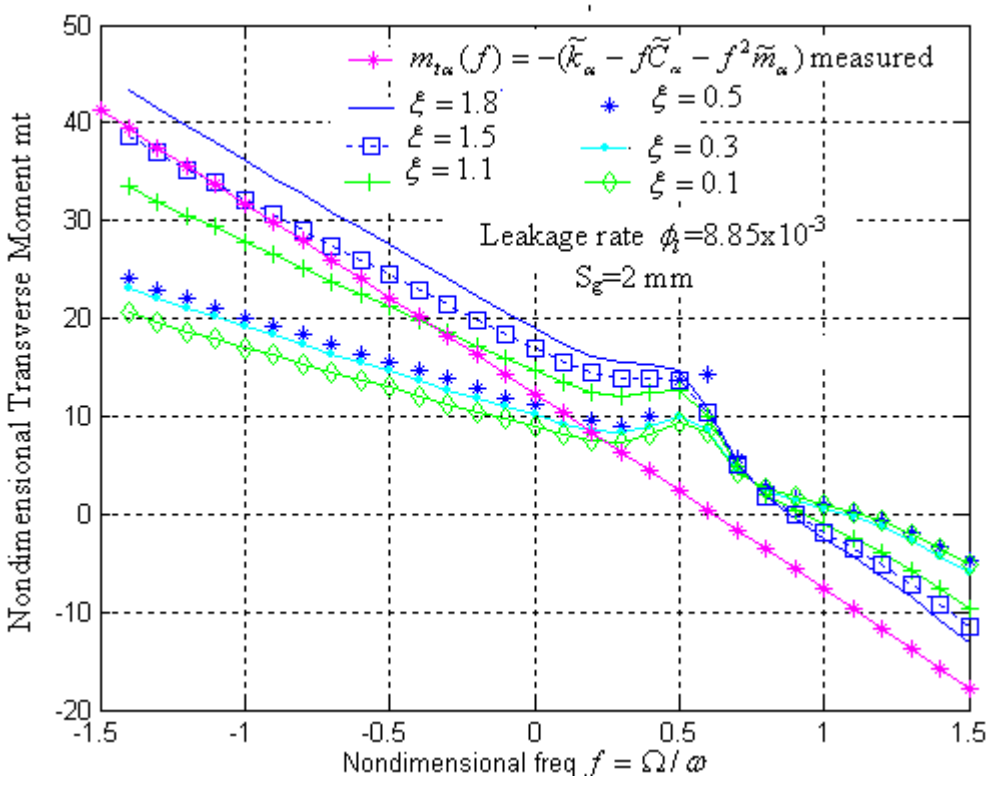

Fig. 12 Calculated transverse moment using compressible code

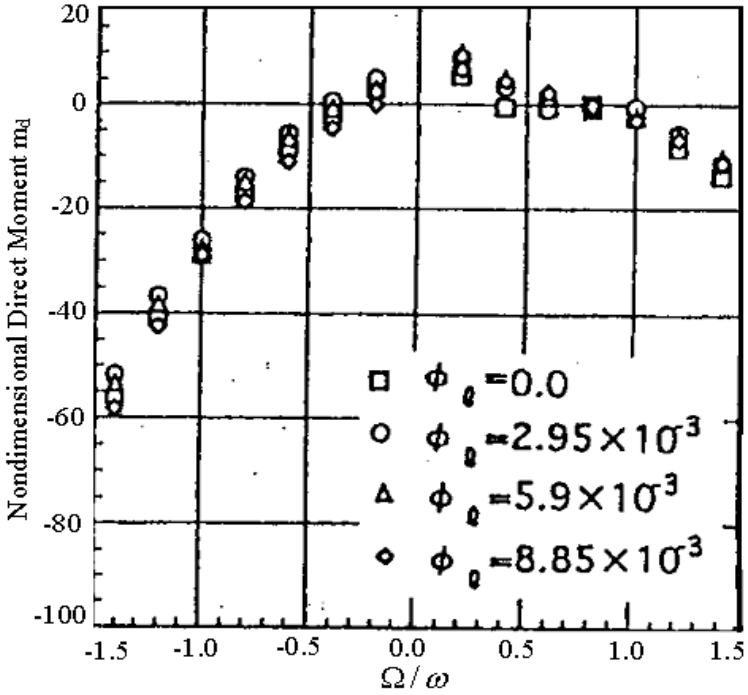

Fig. 13 Measured direct moment [25]

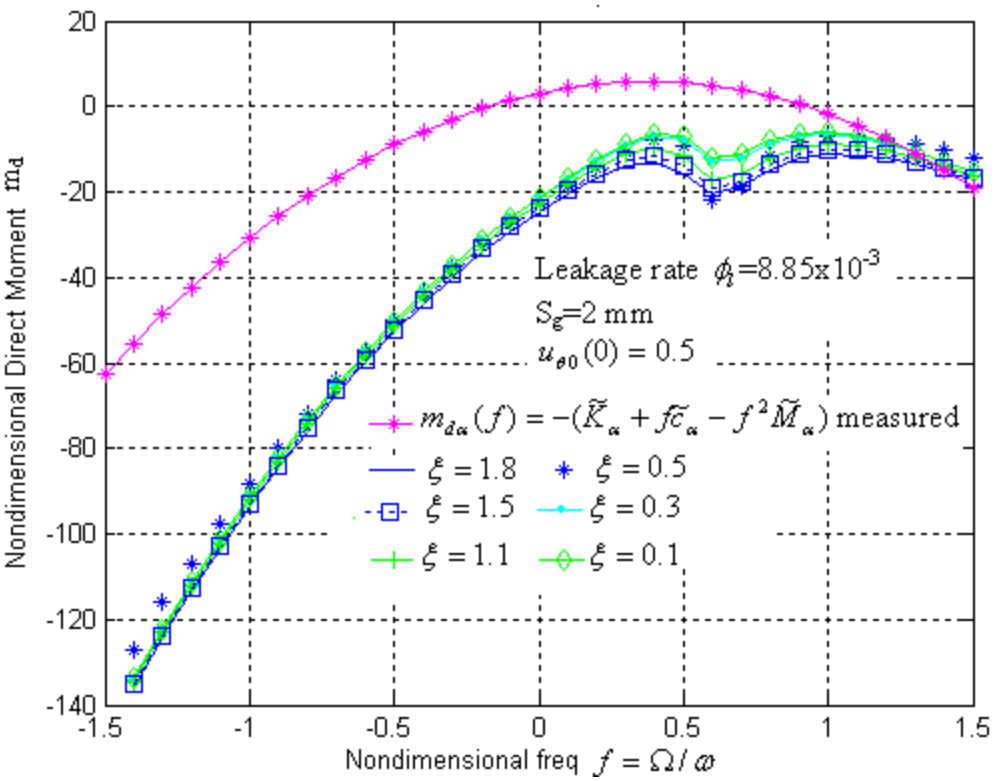

Fig. 14 Calculated direct moment using compressible code

For stability, the transverse moment plays the important role; thus, a bulk flow model does a reasonable job in predicting k_α and C_α, which are important for stability analysis. This shows that the bulk flow model provides a reasonable approximation of the pressure distribution especially for small clearances. Yoshida et al. [25] showed that the unsteady flow in the back shroud/casing clearance caused by the precessing motion is basically a 2-D inviscid flow with minor effects of unsteady wall shear stress. A reasonable match of the cross-coupled stiffness k_α and the direct damping C_α indicates that the bulk-flow model can simulate the destabilizing moments fairly well.

BASIC GEOMETRY AND OPERATING CONDITIONS

Fig. 15 shows the basic clearances of the front and back shroud along with operating pressures obtained from a compressor manufacturer. Operating conditions and working fluid are given in Table 3.

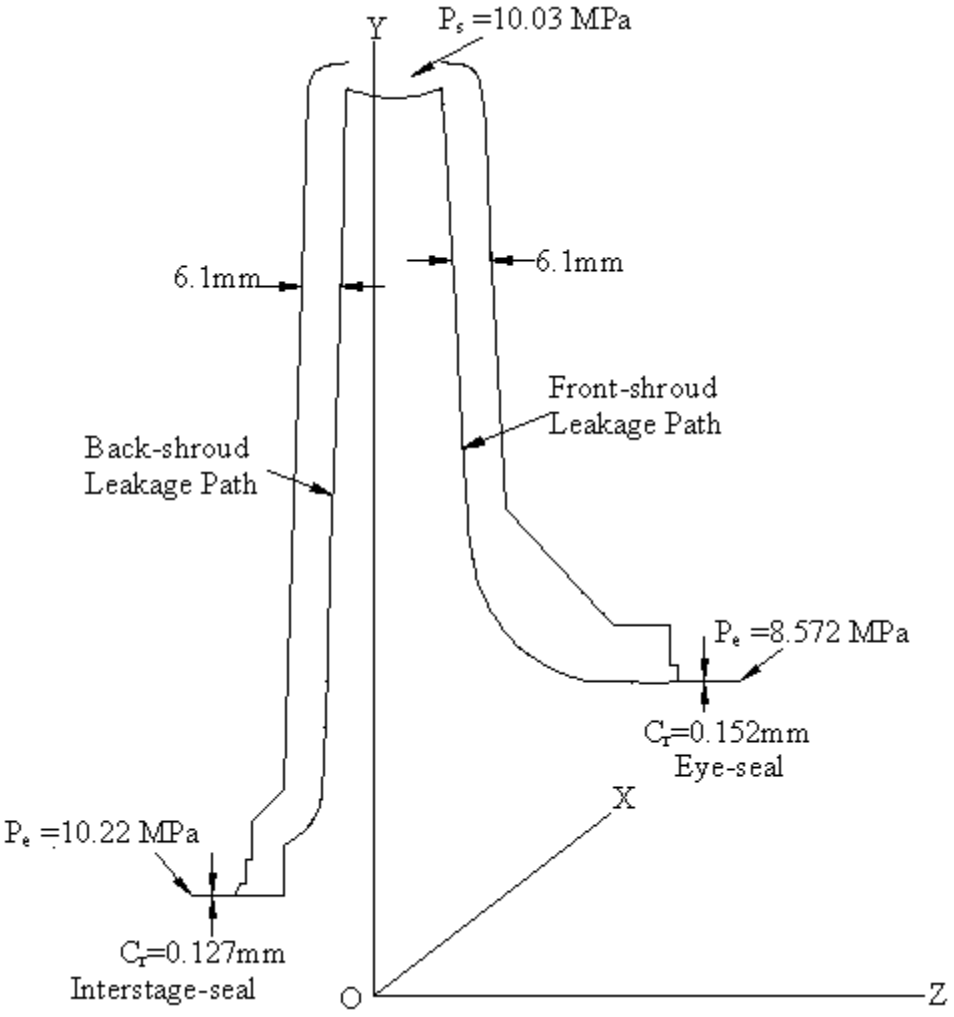

Fig. 15 Basic clearances and pressure conditions of the impeller

Table 3 Operating conditions of the impeller stage

Impeller inlet pressure	8.55 MPa
Impeller exit pressure	10.03 MPa
Impeller eye seal entrance pressure	9.42 MPa
Impeller eye seal exit pressure	8.57 MPa
Interstage seal exit pressure	9.88 MPa
Interstage seal entrance pressure	10.22 MPa
Operating temperature	115.5^0C
Operating Gas	Methane
Inlet Tangential Velocity $u_{\theta 0}$	0.48
Running Speed	11,218 rpm
Eye seal number of teeth	5
Eye seal radial clearance	1.52×10^{-4} m
Eye seal tooth height	2.79×10^{-3} m
Eye seal tooth pitch	2.79×10^{-3} m
Interstage seal number of teeth	5
Interstage seal radial clearance	1.27×10^{-4} m
Interstage seal tooth height	1.78×10^{-3} m
Interstage seal tooth pitch	1.78×10^{-3} m

FRONT SHROUD

Leakage on the front shroud is inward as shown by the arrow in the Fig. 5. Basic impeller geometry for the front shroud is given in Table 4. Basic theory and boundary conditions used are the same as discussed in bulk-flow mathematical model in equations (52), and (56-58).

Table 4 Front shroud basic impeller geometry

Z-coordinate (m)	Radius R (m)	Clearance H (m)
1.1000e-02	0.2545e+00	0.6199e-02
1.2500e-02	0.2280e+00	0.6100e-02
1.4000e-02	0.2010e+00	0.6200e-02
1.5500e-02	0.1810e+00	0.8300e-02
1.7000e-02	0.1749e+00	1.0380e-02
2.3000e-02	0.1656e+00	1.3910e-02
2.9000e-02	0.1615e+00	1.3200e-02
3.5000e-02	0.1600e+00	1.2460e-02
3.8000e-02	0.1600e+00	0.9130e-02
4.1000e-02	0.1597e+00	0.9000e-02
4.7000e-02	0.1597e+00	0.9200e-02

Figs. 16 and 17 illustrate the predicted radial and tangential force coefficients f_{rq} and $f_{\theta q}$, for displacement perturbations, versus the frequency ratio $f = \Omega / \omega$ for the front shroud. A comparison is shown between the compressible and incompressible predictions, and there is not much difference except for some sharper peaks in the compressible predictions. Fig. 17 shows that the tangential force $f_{\theta q}$ has a destabilizing influence for a nondimensional frequency range of 0.0 to 0.71, in which both the tangential force $f_{\theta q}$ and the frequency ratio are positive; therefore acting in the direction of whirling.

Figs. 18 and 19 illustrate the predicted transverse and direct moment coefficients $m_{r\alpha}$ and $m_{\theta\alpha}$, for slope perturbations, versus the precession frequency ratio $f = \Omega/\omega$ for the front shroud. Fig. 18 shows that the transverse moment M_t has a destabilizing affect as both the transverse moment M_t and the precession frequency ratio $f = \Omega/\omega$ are of the same sign except for the precession frequency ratio $0 \le f \le 0.6$, where they are of opposite sign. Also the transverse moment M_t increases with increasing precession frequency ratio f. The sharp peaks predicted occur because of the centrifugal acceleration term in the path-momentum equation. If the term $\frac{2u_{\theta 0}}{b^2 r}\frac{dr}{ds}$ is dropped from the A_{2S} definition of appendix A, the peaks are substantially eliminated. These peaks which were first predicted by Childs [8] in the force coefficients; however, measurements from Caltech researchers [13] did not show these peaks. Since the bulk-flow model neglects any variation in dependent variables across the fluid, and takes the average between the tangential velocity at the stationary wall and the tangential velocity at the rotating shroud, recirculating flow in the leakage path cannot be predicted. Calculated rotordynamic coefficients are given in equations (74-76).

The rotordynamic coefficient matrix for the front shroud in SI units:

$$[m_{FS}] = \begin{bmatrix} 0.27767\text{x}10^{-1} & -0.86271\text{x}10^{-3} & -0.15958\text{x}10^{-1} & -0.18064\text{x}10^{-3} \\ 0.86271\text{x}10^{-3} & 0.27767\text{x}10^{-1} & -0.18064\text{x}10^{-3} & 0.15958\text{x}10^{-1} \\ -0.15057\text{x}10^{-1} & 0.70180\text{x}10^{-4} & 0.16908\text{x}10^{-1} & 0.46401\text{x}10^{-5} \\ 0.70180\text{x}10^{-4} & 0.15057\text{x}10^{-1} & -0.46401\text{x}10^{-5} & 0.16908\text{x}10^{-1} \end{bmatrix} \tag{74}$$

$$[c_{FS}] = \begin{bmatrix} 29.084 & 43.000 & -8.0607 & 22.433 \\ -43.000 & 29.084 & 22.433 & 8.0607 \\ -9.6792 & -21.232 & 3.6161 & -22.357 \\ -21.232 & 9.6792 & 22.357 & 3.6161 \end{bmatrix} \tag{75}$$

$$[k_{FS}] = \begin{bmatrix} -7507.9 & 21972 & 2806.5 & 5635.3 \\ -21972. & -7507.9 & 5635.3 & -2806.5 \\ 4283.6 & -6853.3 & -57.997 & -2218.4 \\ -6853.3 & -4283.6 & 2218.4 & -57.997 \end{bmatrix} \tag{76}$$

Force-only whirl frequency ratio f_w =0.64

Moment-only whirl frequency ratio f_{wM} =0.52

Max. Mach no. M=0.28

Reynolds no. R_α =50,450.

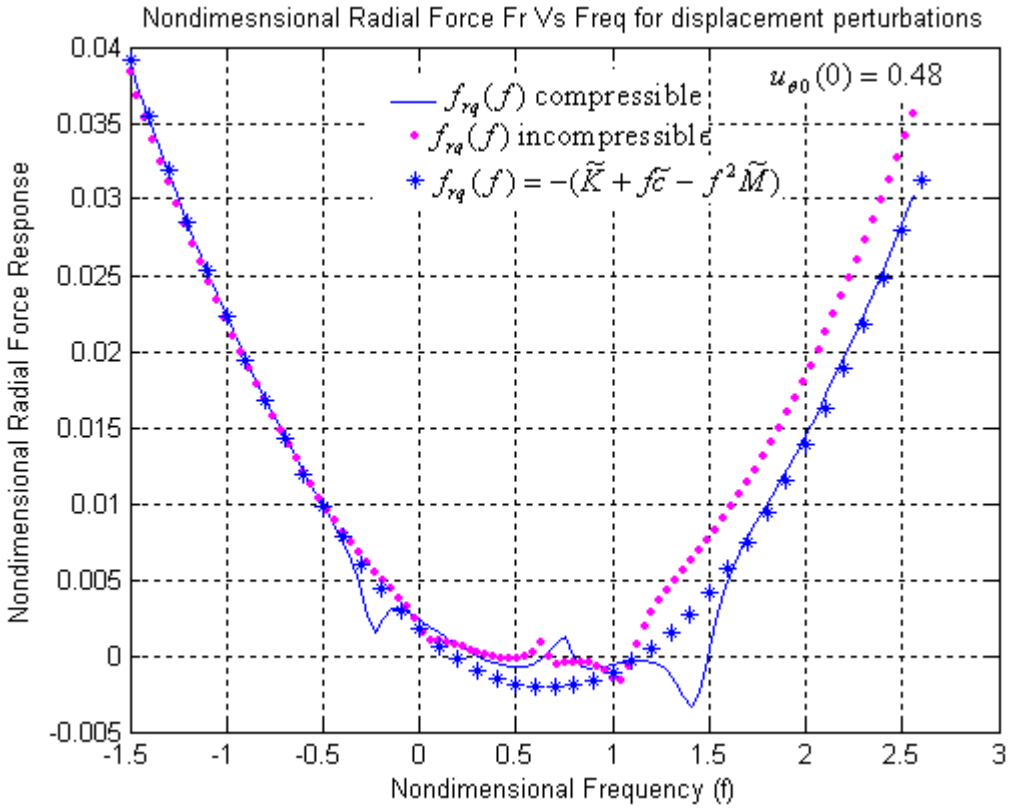

Fig. 16 Nondimensional radial force coefficients for the front shroud

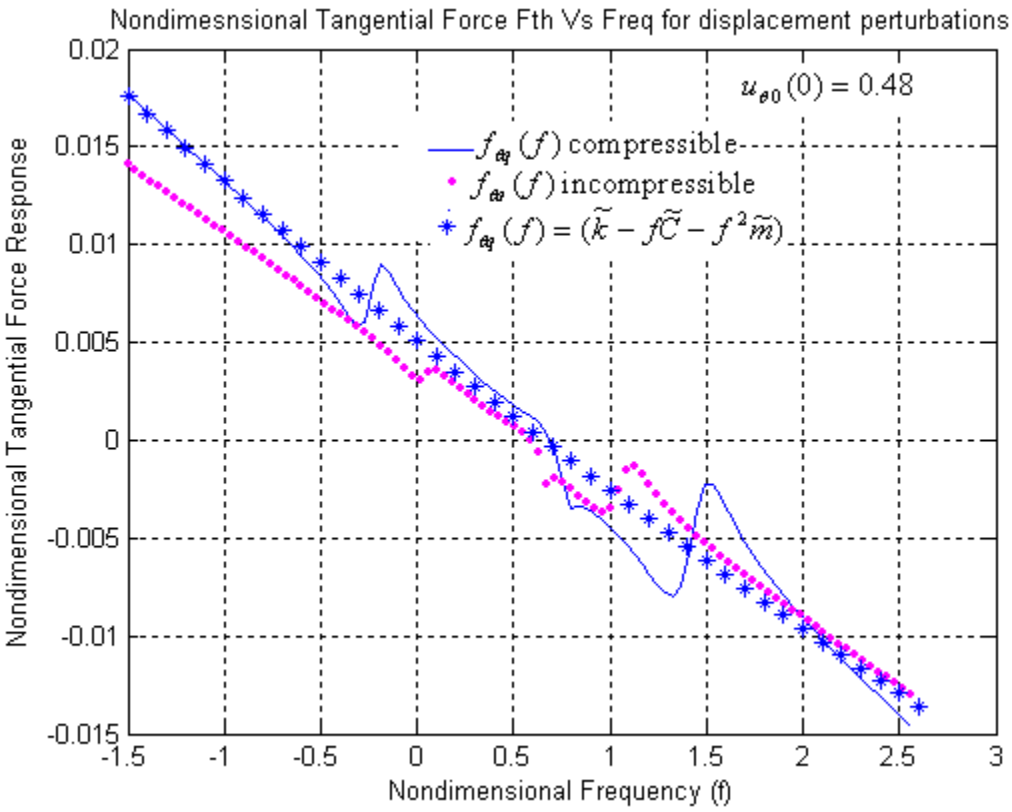

Fig. 17 Nondimensional tangential force coefficients for the front shroud

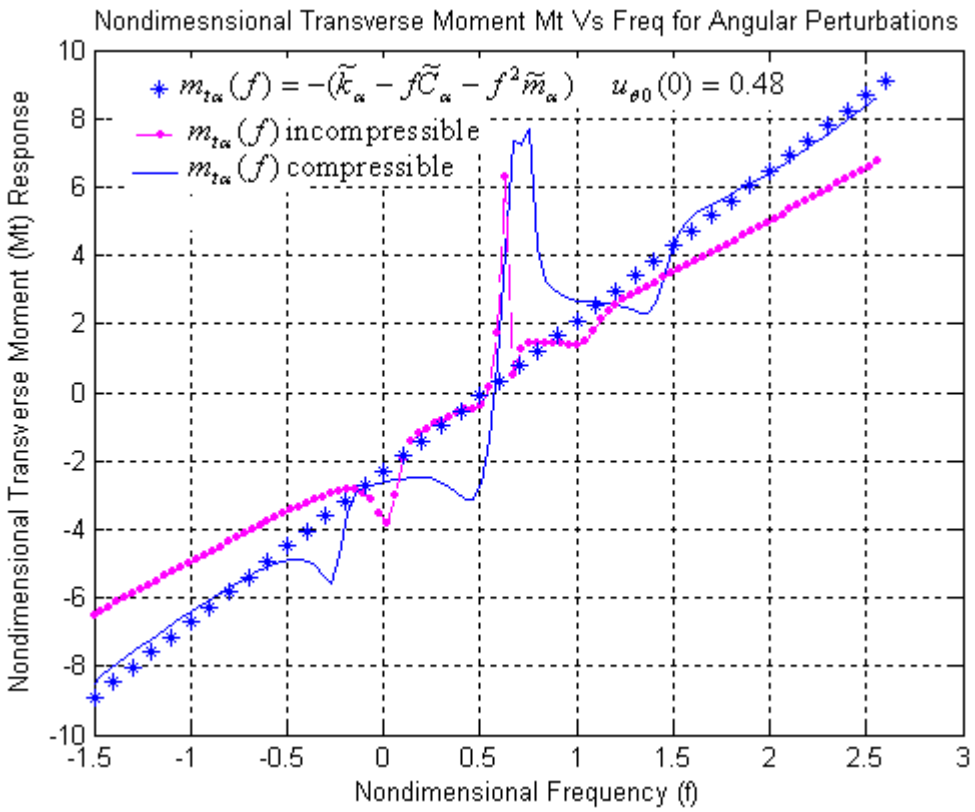

Fig. 18 Nondimensional transverse moment coefficients for the front shroud

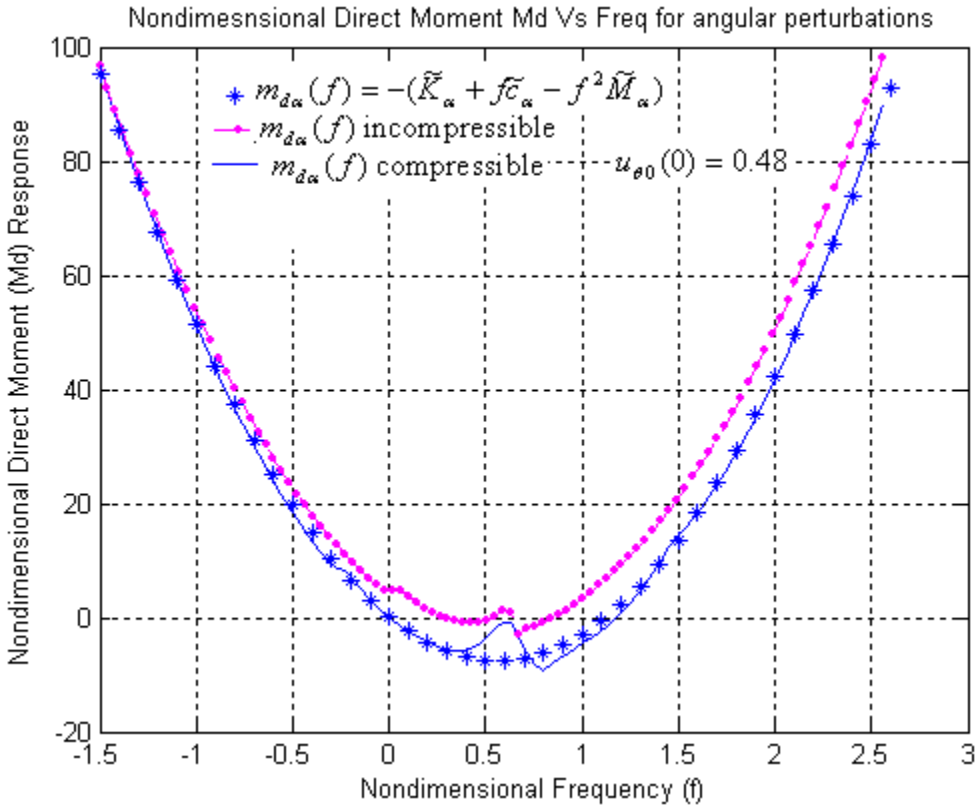

Fig. 19 Nondimensional direct moment coefficients for the front shroud

BACK SHROUD

Flow on the back shroud can be either radially inward, i.e., down the back shroud or radially outward, up the back shroud with circulation taking place. Based on the pressure conditions supplied from a compressor manufacturer, flow on the back shroud was upward. Three important first order boundary conditions for the back shroud are different from that of the front shroud. Interstage labyrinth seal provides restriction, yielding a relationship of the form given by equation (35) and the corresponding perturbation-variable relationship was defined in equation (57). Equations (64) and (58) define the other two boundary conditions for the perturbed pressure and circumferential velocity.

Figs. 20 and 21 give the predicted radial and tangential force coefficients f_{rq} and $f_{\theta q}$ for displacement perturbations, versus the precession frequency ratio $f = \Omega / \omega$ for the back shroud. Rotordynamic force coefficients for the back shroud are much smaller when compared to the front shroud. Fig. 21 illustrate that the tangential force has a destabilizing affect on the shroud for a range of precession frequency ratio $f = \Omega / \omega$, but then these coefficients are much smaller when compared to the front shroud. This outcome is explained by the small projected area of the back shroud in the z-x and y-z plane. Figs. 22 and 23 give the predicted transverse and direct moment coefficients $m_{r\alpha}$ and $m_{\theta\alpha}$, for slope perturbations, versus the precession frequency ratio $f = \Omega / \omega$ for the back shroud. Again these coefficients are much smaller in comparison to the front shroud rotordynamic coefficients. By carrying out a least-square curve fit to the plotted graphs in Figs. 20-23 and using the equations (57) and (58), rotordynamic coefficients are obtained for the back shroud. Second order curve fits for the back shroud results are difficult compared to the front shroud results.

Rotordynamic coefficients for back shroud in SI units:

$$[m_{BS}]=\begin{bmatrix} -0.22724\text{x}10^{-4} & -0.12167\text{x}10^{-4} & -0.28338\text{x}10^{-4} & 0.16291\text{x}10^{-4} \\ 0.12167\text{x}10^{-4} & -0.22724\text{x}10^{-4} & 0.16291\text{x}10^{-4} & 0.28338\text{x}10^{-4} \\ 0.42060\text{x}10^{-6} & -0.55974\text{x}10^{-6} & 0.52222\text{x}10^{-6} & 0.70749\text{x}10^{-6} \\ -0.55974\text{x}10^{-6} & -0.42060\text{x}10^{-6} & -0.70749\text{x}10^{-6} & 0.52222\text{x}10^{-6} \end{bmatrix} \quad (77)$$

$$[c_{BS}]=\begin{bmatrix} 0.68020\text{x}10^{-1} & -0.26607\text{x}10^{-1} & -0.62297\text{x}10^{-2} & 0.34362\text{x}10^{-1} \\ 0.26607\text{x}10^{-1} & 0.68020\text{x}10^{-1} & 0.34362\text{x}10^{-1} & 0.62297\text{x}10^{-2} \\ 0.14386\text{x}10^{-2} & 0.50673\text{x}10^{-3} & 0.67944\text{x}10^{-3} & -0.65192\text{x}10^{-3} \\ 0.50673\text{x}10^{-3} & -0.14386\text{x}10^{-2} & 0.65192\text{x}10^{-3} & 0.67944\text{x}10^{-3} \end{bmatrix} \quad (78)$$

$$[k_{BS}]=\begin{bmatrix} -40.933 & 31.527 & -49.786 & -147.41 \\ -31.527 & -40.933 & -147.41 & 49.786 \\ 0.56878 & 1.2018 & 0.74027 & -2.9707 \\ 1.2018 & -0.56878 & 2.9707 & 0.74027 \end{bmatrix} \quad (79)$$

Force-only whirl frequency ratio f_w =0.39

Moment-only whirl frequency ratio f_{wM} =0.42

Max. Mach no. M=0.25

Reynolds no. R_α =33,205.

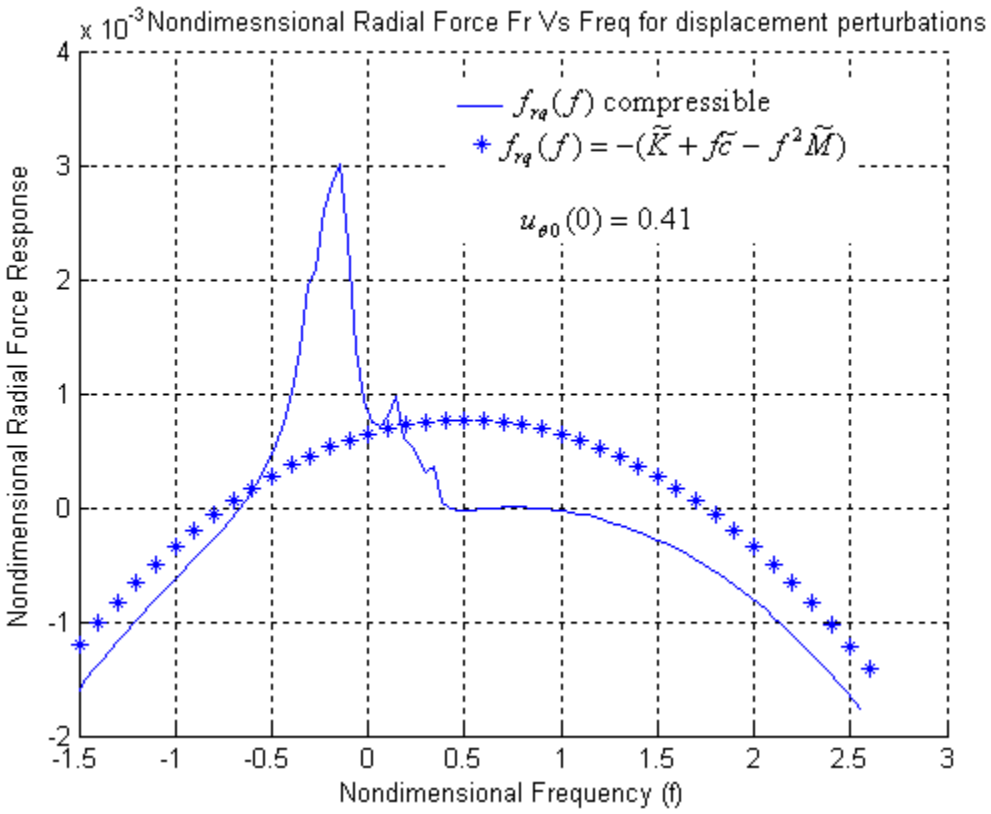

Fig. 20 Nondimensional radial force coefficients for the back shroud

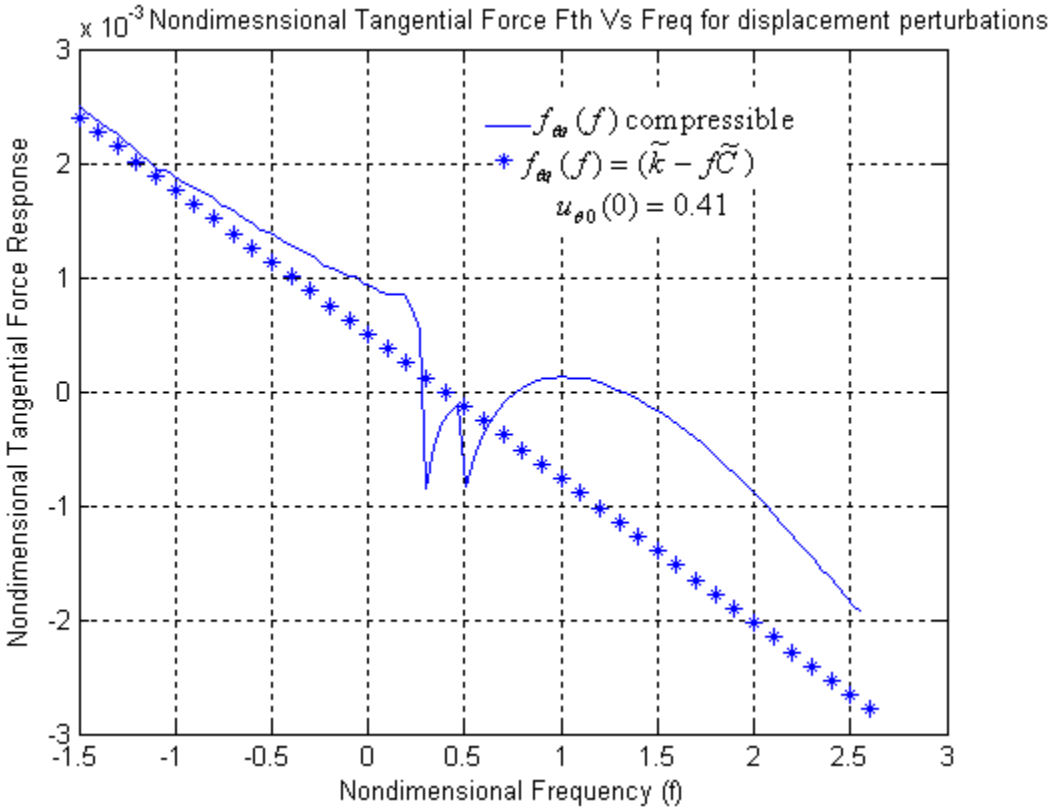

Fig. 21 Nondimensional tangential force coefficients for the back shroud

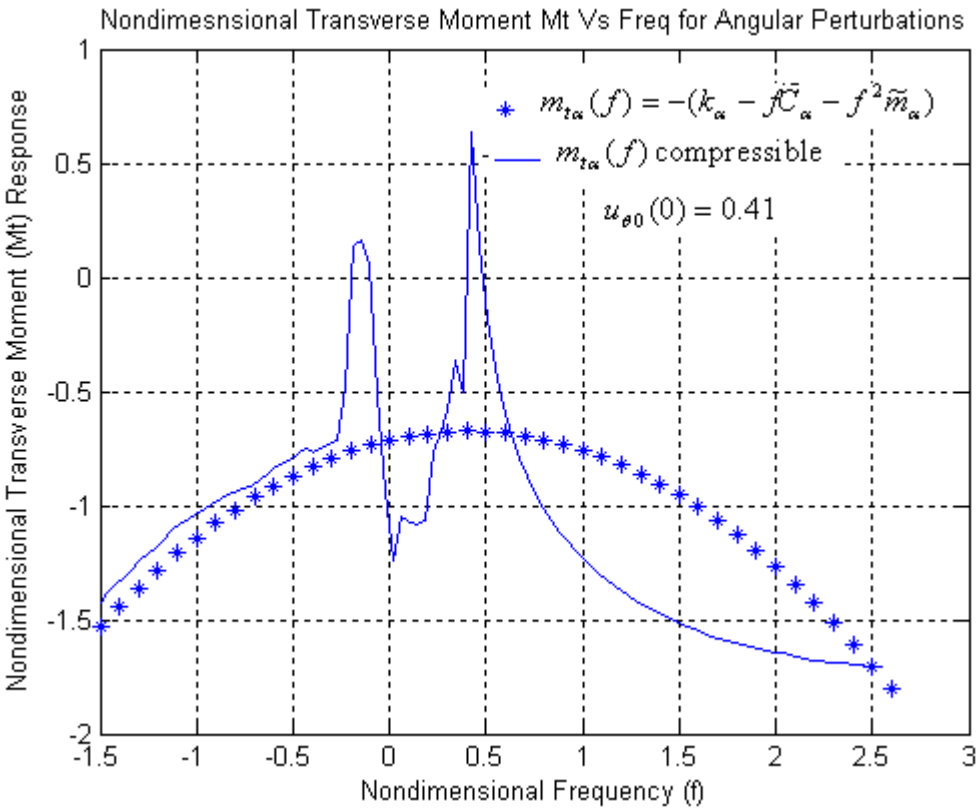

Fig. 22 Nondimensional transverse moment coefficients for the back shroud

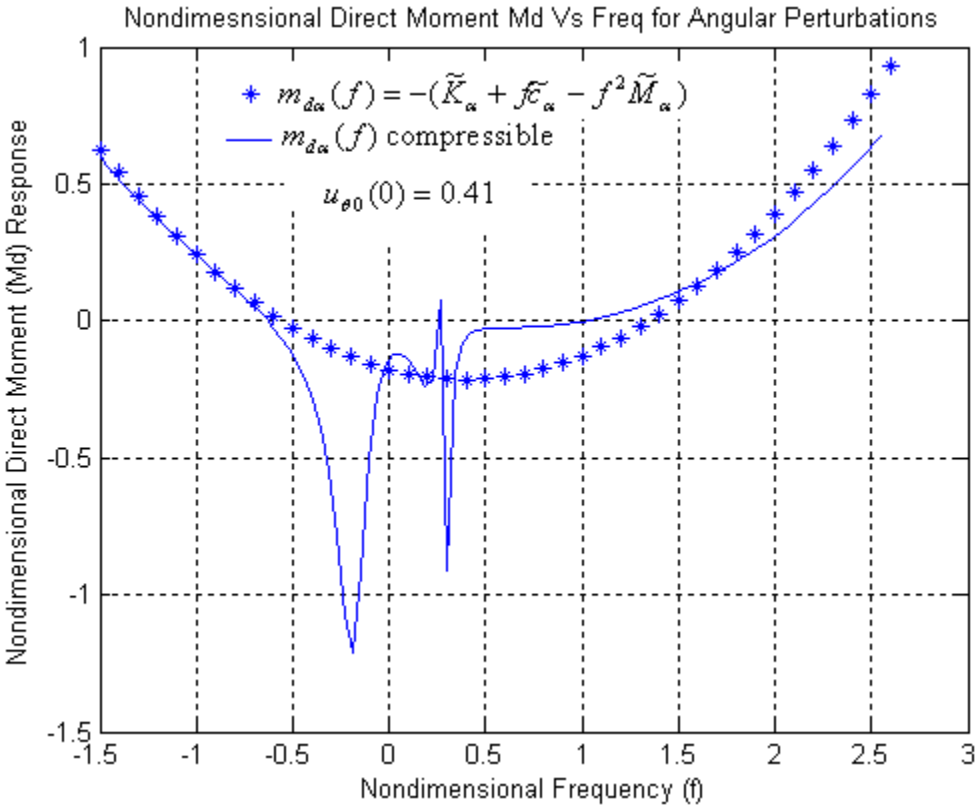

Fig. 23 Nondimensional direct moment coefficients for the back shroud

LABYRINTH SEALS

Forces developed by the labyrinth seals are roughly proportional to the pressure drop across the seals and the fluid density within the seal. Fig. 5 illustrates a typical sealing arrangement for a multi-stage centrifugal compressor. The eye-packing seal limits return-flow leakage down the front of the impeller, and the shaft seal restricts leakage along the shaft to the preceding stage. Labyrinths have negligible added-mass terms and are typically modeled by the reaction-force/motion model defined in equation (2) (Childs [2]).

The first model containing essential physical elements to predict the seal coefficients was published by Iwatsubo [31]. Iwatsubo wrote the circumferential-momentum and continuity equations to define the average (bulk-flow) circumferential velocity within a labyrinth cavity. He used a leakage equation to define the axial velocity. Childs and Scharrer [28] used Iwatsubo's analysis and included variation of the area in the circumferential direction and also presented measurements of both stiffness and damping coefficients used in rotordynamic analysis.

Considering X_s, Y_s and $\dot{X}_s$ and $\dot{Y}_s$ as the displacement and velocity of the seal's center in the x and y directions, X_s and Y_s are related to impeller's relative displacements (X,Y) and impeller's relative small pitch and yaw rotation vectors (α_X, α_Y) by the following relations:

$$X_s = X + l\alpha_Y \tag{80}$$

$$Y_s = Y - l\alpha_X,$$

where l is the z distance between the seal center and the origin of the impeller axis system of Fig. 15.

Differentiating the above relations we get:

$$\dot{X}_s = \dot{X} + l\dot{\alpha}_Y \tag{81}$$

$$\dot{Y}_s = \dot{Y} - l\dot{\alpha}_X$$

Also, considering the moment about impeller's origin, we get

$$M_{Y_S} = F_{X_S} l \tag{82}$$

$$M_{X_S} = -F_{Y_S} l$$

Therefore the resulting rotordynamic matrix becomes

$$-\begin{Bmatrix} F_{X_S} \\ F_{Y_S} \\ M_{Y_S} \\ M_{X_S} \end{Bmatrix} = \begin{bmatrix} K & k & Kl & -kl \\ -k & K & -kl & -Kl \\ Kl & kl & Kl^2 & -kl^2 \\ kl & -Kl & kl^2 & Kl^2 \end{bmatrix} \begin{Bmatrix} X \\ Y \\ \alpha_Y \\ \alpha_X \end{Bmatrix} + \begin{bmatrix} C & c & Cl & -cl \\ -c & C & -cl & -Cl \\ Cl & cl & Cl^2 & -cl^2 \\ cl & -Cl & cl^2 & Cl^2 \end{bmatrix} \begin{Bmatrix} \dot{X} \\ \dot{Y} \\ \dot{\alpha}_Y \\ \dot{\alpha}_X \end{Bmatrix} \qquad (83)$$

Basic geometry and operating conditions of the eye seal and interstage seal are given in Table 3. Table 5 gives the rotordynamic coefficients for the eye seal considering zero inlet perturbations in the pressure p_1 and tangential velocity $u_{\theta 1}$. Table 6 gives the leakage rate and rotordynamic coefficients for the interstage seal with leakage upward. By comparison of eye seal and interstage seal coefficients, we see that the eye seal coefficients are bigger than the interstage seal, and thus eye seal has greater influence on the stability. Since the origin of the inertial co-ordinate system is between the two seals, the moment caused by the two seals are in opposite direction. Thus l in equation (74) is positive for eye seal, and is negative for interstage seal. The labyrinth seal code predicted high force whirl frequency ratio f_w than is seen experimentally for short seals; therefore the cross-coupled stiffness k was modified such that $f_w \cong u_{\theta 0}(0)$.

Table 5 Eye seal results

Leakage rate $\dot{m}$ (Kg/sec)	0.539
Seal inlet tangential velocity $u_{\theta 0}$	0.6
Direct stiffness K (N/m)	0.12627×10^6
Cross-coupled stiffness k (N/m)	7.734×10^5
Direct damping C (N-sec/m)	1097.5
Cross-coupled damping c (N-sec/m)	-247.28
Whirl frequency ratio f_w	0.6
l z-length from origin (m)	0.0549
Cross-coupled stiffness k_α (N-m/rad)	2331.03
Direct damping C_α (N-m-s/rad)	3.308

Table 6 Interstage seal results

Leakage rate $\dot{m}$ (Kg/sec)	0.226
Seal inlet tangential velocity $u_{\theta 0}$	0.5
Direct stiffness K (N/m)	4152.8
Cross-coupled stiffness k (N/m)	0.1736×10^{6}
Direct damping C (N-sec/m)	306.06
Cross-coupled damping c (N-sec/m)	-5.4530
Whirl frequency ratio f_w	0.48
l z-length from origin (m)	-0.0265
Cross-coupled stiffness k_α (N-m/rad)	121.9
Direct damping C_α (N-m-s/rad)	0.214

Tables 5 and 6 show that seals produce greater direct stiffness K than the impeller. It is also seen that the cross-coupled stiffness k and direct damping C are greater for the seals. Thus for displacement perturbations, seals influence the stability more than the impellers.

Radially Inward Leakage Flow

Based on the data provided, the leakage on the back shroud was found to be radially outward. Inward leakage flow was forced by dropping the exit pressure at the interstage seal. Table 7 gives the rotordynamic coefficients and leakage rate for different exit pressures and shows that the leakage rate increases, and the seal inlet tangential velocity $u_{\theta 0}$ decreases with additional decreases in the seal exit pressure. A high pressure at the interstage seal exit reduces the stability of the rotor, which is evident from the high whirl frequency ratio. Predicted rotordynamic coefficients are larger for radially inward leakage than with radially outward leakage. Stability of the system is reduced with inward leakage because of high swirl entering the seal which increases as it approaches the impeller hub on the back side. The cross-coupled stiffness k in Table 7 was modified so that $f_w \cong u_{\theta 0}(0)$.

Table 7 Operating conditions and rotordynamic coefficients for different interstage seal exit pressure with radially inward flow

Seal Exit Pressure	97 bar (down)	95 bar (down)	90 bar (down)	(upward)
$\dot{m}$ (Kg/sec)	0.290377	0.345	0.4139	0.226
Seal inlet $u_{\theta 0}$	0.8973	0.881	0.8478	0.5
Seal k (N/m)	3.994E+05	4.403E+05	5.15E+05	1.736×10^5
Seal C (N-s/m)	379.17	425.55	517.22	306.06
Impeller k (N/m)	134.57	141.62	169.62	31.527
Impeller C (N-s/m)	0.20535	0.22266	0.25311	0.068
Impeller WFR f_w	0.55784	0.54142	0.57048	0.39
Seal WFR f_w	0.897	0.881	0.847	0.48
Seal k_α (N-m/rad)	280.47	309.2	361.65	121.9
Seal C_α (N-m-s/rad)	0.266	0.298	0.363	0.214

FULL-STAGE PREDICTIONS

Rotordynamic coefficients derived for individual components are assembled to get the full-stage predictions. Forces and moments due to front and back shroud add, but the forces for the seals add and, the moments subtract. Table 8 gives the complete rotordynamic coefficients for eye seal, interstage seal, and front and back shroud. Table 8 shows that the eye-seal has bigger rotordynamic coefficients followed by the interstage seal, and therefore seals are more likely to influence stability than the shrouds. Rotordynamic coefficient matrices including eye seal, interstage seal, and front and back shrouds are given in SI units in equations (84-86).

$$[m_{\sum}] = \begin{bmatrix} 0.027 & -0.001 & -0.016 & -0.000 \\ 0.001 & 0.027 & -0.000 & 0.016 \\ -0.015 & 0.000 & 0.017 & 0.000 \\ 0.000 & 0.015 & -0.000 & 0.017 \end{bmatrix} \tag{84}$$

$$[k_{\sum}] = 10^5 \begin{bmatrix} 1.229 & 9.69 & 0.095 & -0.323 \\ -9.69 & 1.229 & -0.323 & -0.095 \\ 0.11 & 0.31 & 0.003 & -0.046 \\ 0.31 & -0.11 & 0.046 & 0.003 \end{bmatrix} \tag{85}$$

$$[c_{\sum}] = 10^3 \begin{bmatrix} 1.432 & -0.209 & 0.044 & 0.035 \\ 0.209 & 1.432 & -0.035 & -0.044 \\ 0.042 & -0.034 & 0.007 & -0.021 \\ -0.034 & -0.042 & 0.021 & 0.007 \end{bmatrix} \tag{86}$$

Table 8 Complete rotordynamic coefficients for eye seal, interstage seal, and front and back shroud

Coefficients	Eye seal	Interstage seal	Frontshroud	Backshroud	Total (Σ)
K (N/m)	$1.263\text{x}10^{5}$	$4.152\text{x}10^{3}$	$-7.507\text{x}10^{3}$	-40.933	$1.229\text{x}10^{5}$
k (N/m)	$7.734\text{x}10^{5}$	$1.736\text{x}10^{5}$	$2.197\text{x}10^{4}$	31.527	$9.69\text{x}10^{5}$
C (N-s/m)	1097.5	306.06	29.084	0.068	$1.43\text{x}10^{3}$
c (N-s/m)	-247.28	-5.453	43.000	-0.026	-209.8
M (Kg)	0.0	0.0	0.027	$-0.22\text{x}10^{-4}$	0.0270
m (Kg)	0.0	0.0	$-0.86\text{x}10^{-3}$	$-0.12\text{x}10^{-4}$	$-8.72\text{x}10^{-4}$
K_{α} (N-m/rad)	380.66	2.915	-57.997	0.74027	326.32
k_{α} (N-m/rad)	2331.03	121.9	$2.218\text{x}10^{3}$	2.9707	$4.67\text{x}10^{3}$
C_{α} (N-m-s/rad)	3.308	0.214	3.6161	$0.67\text{x}10^{-3}$	7.138
c_{α} (N-m-s/rad)	-0.75	-0.004	22.357	$0.65\text{x}10^{-3}$	21.60
M_{α} (Kg-m^2)	0.0	0.0	0.016	$0.52\text{x}10^{-6}$	0.016
m_{α} (Kg-m^2)	0.0	0.0	$-0.46\text{x}10^{-5}$	$-0.70\text{x}10^{-6}$	$-5.3\text{x}10^{-6}$
$K_{\varepsilon\alpha}$ (N/rad)	$6.93\text{x}10^{3}$	-110	$2.806\text{x}10^{3}$	-49.786	$9.58\text{x}10^{3}$
$k_{\varepsilon\alpha}$ (N/rad)	$4.25\text{x}10^{4}$	$-4.6\text{x}10^{3}$	$-5.635\text{x}10^{3}$	147.41	$3.241\text{x}10^{4}$
$C_{\varepsilon\alpha}$ (N-s/rad)	60.25	-8.11	-8.0607	-0.006	44.07
$c_{\varepsilon\alpha}$ (N-s/rad)	-13.57	0.14	-22.43	-0.034	-35.89
$M_{\varepsilon\alpha}$ (Kg-m)	0.0	0.0	-0.016	$-0.28\text{x}10^{-4}$	-0.016
$m_{\varepsilon\alpha}$ (Kg-m)	0.0	0.0	$0.18\text{x}10^{-3}$	$-0.16\text{x}10^{-4}$	$1.64\text{x}10^{-4}$
$K_{\alpha\varepsilon}$ (N)	$6.93\text{x}10^{3}$	-110	$4.283\text{x}10^{3}$	0.56878	$1.11\text{x}10^{4}$
$k_{\alpha\varepsilon}$ (N)	$4.25\text{x}10^{4}$	$-4.6\text{x}10^{3}$	$-6.853\text{x}10^{3}$	1.2018	$3.10\text{x}10^{4}$
$C_{\alpha\varepsilon}$ (N-s)	60.25	-8.11	-9.6792	0.001	42.46
$c_{\alpha\varepsilon}$ (N-s)	-13.57	0.14	-21.232	$0.5\text{x}10^{-3}$	-34.6
$M_{\alpha\varepsilon}$ (N-s^2)	0.0	0.0	-0.015	$0.42\text{x}10^{-6}$	-0.015
$m_{\alpha\varepsilon}$ (N-s^2)	0.0	0.0	$0.7\text{x}10^{-4}$	$-0.55\text{x}10^{-6}$	$6.95\text{x}10^{-5}$

WACHEL'S MODEL

Wachel's coefficient defined by equation (8) is calculated by using the parameters given in Table 9.

Table 9 Impeller data for Wachel's coefficient calculation at 11,218 rpm

B: cross coupling constant (SI)	16
hp: power (KW)	1256.48
MW: molecular weight	16
D: impeller diameter (m)	0.5064
h: restrictive dimension in flow path (m)	0.0152
f: speed (Hz)	186.96
ρ_D : density of fluid at discharge conditions, kg/m^3	50.43
ρ_S : density of fluid at suction conditions, kg/m^3	43.02

From the values given in Table 9, Wachel's coefficient is calculated to be: K_{xy} =2.62006x10^5 N/m. This model does not give damping; thus, a comparison for stability predictions between Wachel's model and the compressible model is difficult. XLTRC is used to make a comparison between the two models. Data for lower speeds are obtained by extrapolation by using the compressor performance curves which are discussed in the next topic.

DATA EXTRAPOLATION

Since the impeller stage data given are only for a single running speed, pressure conditions are extrapolated by using the typical centrifugal compressor performance curves with respect to speed. Fig. 24 shows that for a typical centrifugal compressor, the compressor torque varies linearly with speed, especially at higher speeds near the design speed. When a curve fit was done for the pressure ratio and the speed points obtained from Fig 25, which gives the flow rate versus the pressure ratio for different speeds, a linear fit was obtained. Thus the pressure is assumed to rise linearly with the increasing speed. This assumption is further justified as we are interested in the static pressure at the impeller discharge and not the total stagnation pressure, which can change quadratically with speed because of the dynamic pressure coming from the kinetic energy which squares with speed. Since power is defined as product of torque and the running speed, i.e. $Power = T\omega$, power is assumed to vary quadratically with speed.

Table 10 gives the pressure conditions, rotordynamic coefficients and Wachel's coefficient for various speeds for front shroud and eye seal. Pressure conditions and rotordynamic coefficients for various speeds for the back shroud and interstage seal with flow upward and downward are given in Tables 11 and 12 respectively. Most of the rotordynamic coefficients are proportional to Δp across the impeller. Increasing Δp also increases the leakage.

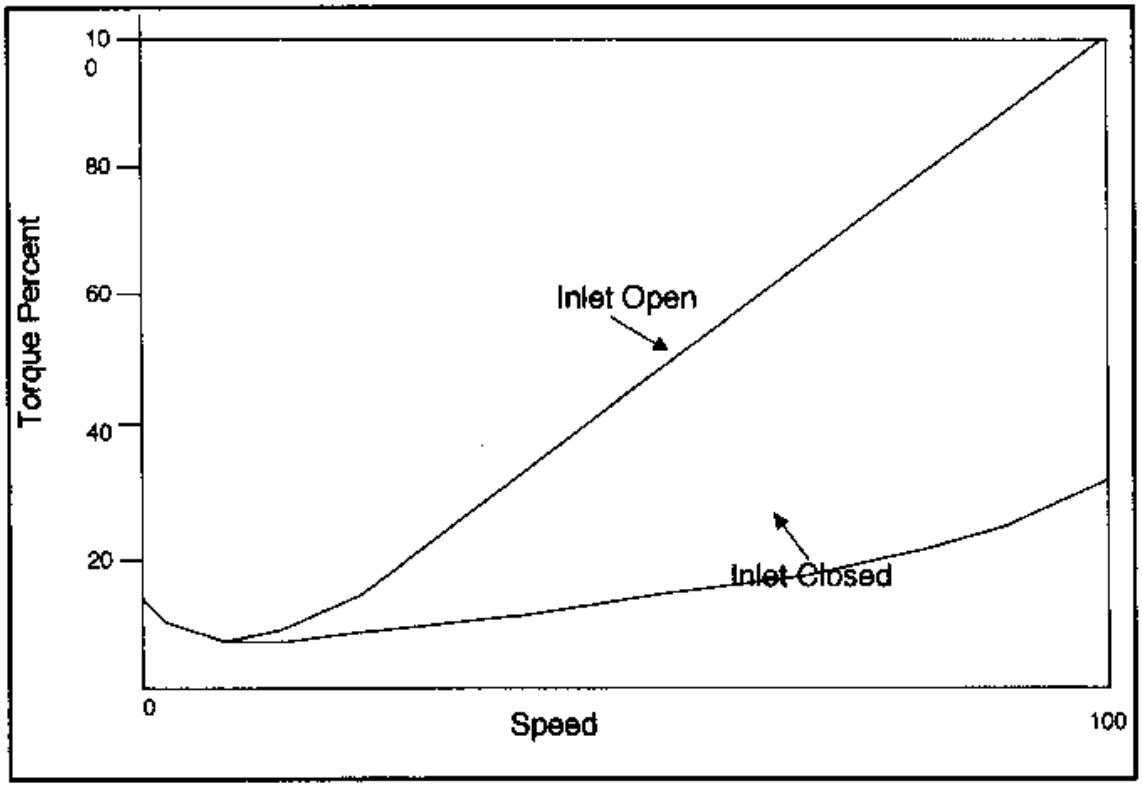

Fig. 24 Typical compressor speed-torque curve [4]

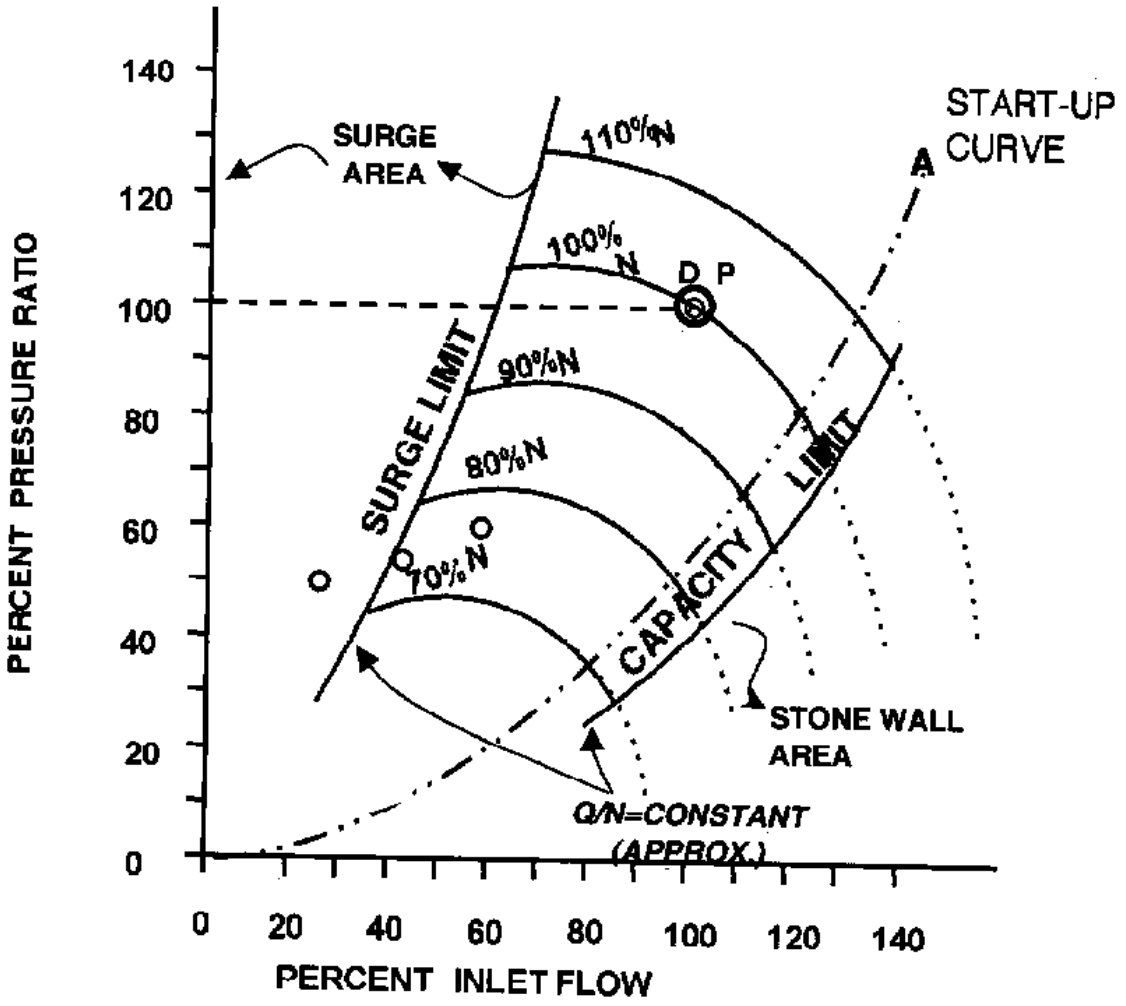

Fig. 25 Typical compressor performance characteristics [4]

Table 10 Operating conditions and calculated rotordynamic coefficients for various speeds for front shroud and eye seal

Running speed →	11,218 rpm	8,000 rpm	6,000 rpm	4,000 rpm
Psupply (Bar)	100.347	71.52	53.67	35.78
Pseal-exit (Bar)	85.72	61.05	45.84	30.56
$\dot{m}$ (Kg/sec)	0.542	0.425	0.331	0.227
Seal inlet $u_{\theta 0}$	0.646	0.699	0.740	0.793
Seal k (N/m)	8.335E+05	4.715E+05	2.768E+05	1.275E+05
Seal C (N-s/m)	1098.5	804.63	595.46	383.50
Impeller k (N/m)	21972	13210.	8044.5	3767.7
Impeller C (N-s/m)	29.084	21.558	16.129	10.486
Impeller WFR f_w	0.643	0.731	0.793	0.857
Seal WFR f_w	0.646	0.699	0.74	0.793
Power (KW)	1256.48	639.005	359.44	159.75
Wachel's Coeff. Kxy (N/m)	2.62E+05	1.867E+05	1.399E+05	9.3267E+04

Table 11 Operating conditions and calculated rotordynamic coefficients for various speeds for back shroud and interstage seal with leakage upward

Running speed →	11,218 rpm	8,000 rpm	6,000 rpm	4,000 rpm
Psupply (Bar)	100.347	71.52	53.67	35.78
Pseal-exit (Bar)	102.2	72.88	54.662	36.441
$\dot{m}$ (Kg/sec)	0.226	0.161	0.1211	0.0808
Seal inlet $u_{\theta 0}$	0.5	0.5	0.5	0.5
Seal k (N/m)	1.736E+06	9.625E+04.	4.9118E+04	2.109E+04
Seal C (N-s/m)	306.06	213.25	156.38	100.72
Impeller k (N/m)	31.527	26.464	15.424	6.1314
Impeller C (N-s/m)	0.6802E-01	0.26029E-01	0.117E-01	0.3988E-02
Impeller WFR f_w	0.39454	1.2136	2.0950	3.6733
Seal WFR f_w	0.4829	0.5388	0.5	0.5

Table 12 Operating conditions and rotordynamic coefficients for various speeds for back shroud and interstage seal with leakage inward

Running speed →	11,218 rpm	8,000 rpm	6,000 rpm	4,000 rpm
Psupply (Bar)	100.347	71.52	53.67	35.78
Pseal-exit (Bar)	97	69.13	51.87	34.586
$\dot{m}$ (Kg/sec)	0.290377	0.188	0.1298	0.083
Seal inlet $u_{\theta 0}$	0.8973	0.8891	0.8809	0.862
Seal k (N/m)	3.996E+05	1.741E+05	8.974E+04	3.621E+04
Seal C (N-s/m)	379.17	233.87	162.17	100.31
Impeller k (N/m)	134.57	61.612	31.590	12.560
Impeller C (N-s/m)	0.20535	0.12058	0.7784E-01	0.4406E-01
Impeller WFR f_w	0.55784	0.60993	0.64586	0.68052
Seal WFR f_w	0.897	0.889	0.88	0.862

XLTRC COMPARISON

A semi cantilevered rotor carrying the impeller with a first backward critical at 5389 cpm i.e. about one half running speed was developed for the comparison. One end of the rotor is fixed for both displacement and rotation, represented by bearing 1 as shown in the geoplot (Fig. 26). Direct stiffness $K_{XX} = K_{YY} =$ 1.05x10^8 N/m for displacement constraint and $K_{\alpha x \alpha x} = K_{\alpha y \alpha y} =$1.14x10^6 N-m/rad for rotation constraint are used to constraint both the displacement and rotation at bearing 1. External damping $C_{xx} = C_{yy} = 6650$ N-s/m and $C_{\alpha x \alpha x} = C_{\alpha y \alpha y} = 1.15$ N-ms/rad are considered at the bearing 1, so that Wachel's cross-coupled stiffness K_{XY} caused it to become just unstable at the running speed. Another dummy bearing is placed at station 3 with zero stiffness for displacement and rotation, i.e. $K_{XX} = K_{YY} = 0$ N/m and $K_{\alpha x \alpha x} = K_{\alpha y \alpha y} =0$ N-m/rad, and a direct damping $C_{xx} = C_{yy} = 0$ N-s/m. Table13 gives the damped natural frequencies for different running speeds with Wachel's model. The rotor goes unstable at the design running speed with the log decrement $\delta = -0.0004$ and a 1st forward whirling frequency of 7093 cpm. First backward and forward modes of the cantilevered rotor at the running speed are shown in Figs.27-29.

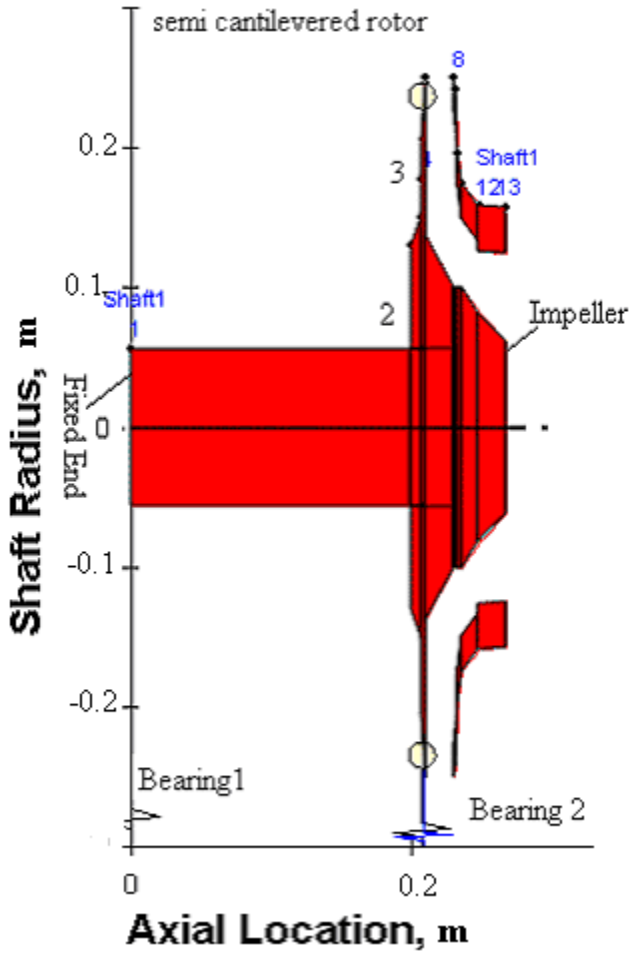

Fig. 26 Semi-cantilevered impeller model

Table 13 Damped eigenvalues with Wachel's model

Speed	logd1	cpm1	logd2	cpm2
1000.	0.025	6159.8	0.020	6313.8
2000.	0.028	6082.9	0.017	6390.9
3000.	0.031	6006.2	0.015	6467.9
4000.	0.034	5929.8	0.013	6544.9
5000.	0.037	5853.6	0.010	6621.7
6000.	0.041	5777.7	0.008	6698.3
7000.	0.044	5702.3	0.006	6774.7
8000.	0.048	5627.2	0.005	6850.8
9000.	0.051	5552.6	0.003	6926.5
10000.	0.055	5478.6	0.001	7001.9
11000.	0.059	5405.1	-0.0001	7076.8
11218.	0.060	5389.1	**-0.0004**	**7093.1**
13000.	0.067	5259.9	-0.003	7225.3

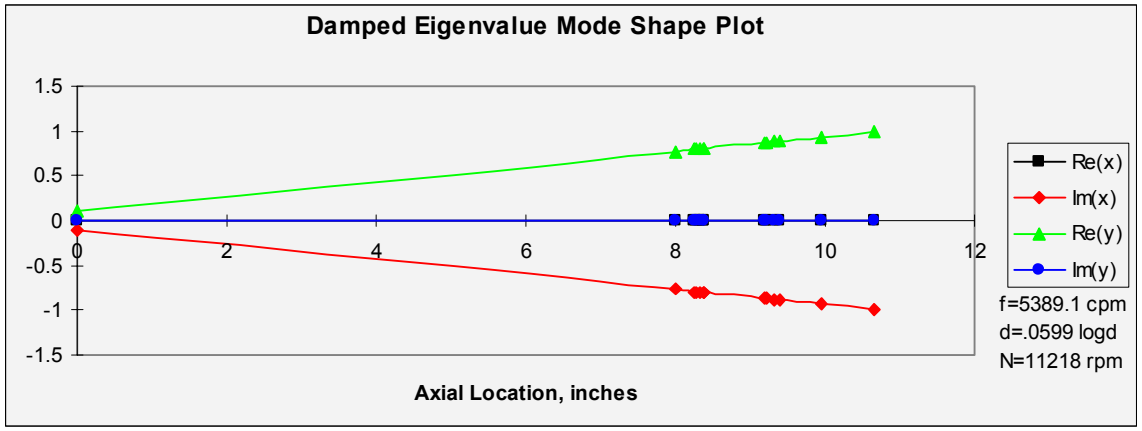

Fig. 27 1st backward mode shape plot at the running speed of 11,218 rpm with Wachel's model

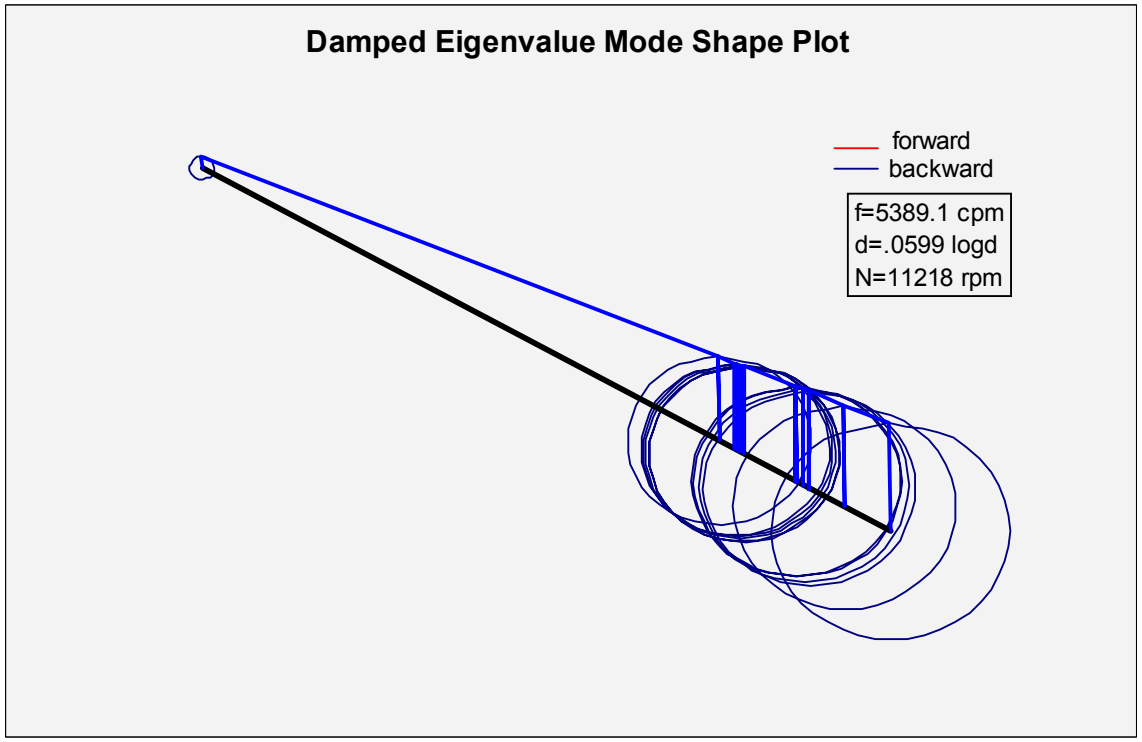

Fig. 28 3D 1st backward mode shape plot at the running speed of 11,218 rpm with Wachel's model

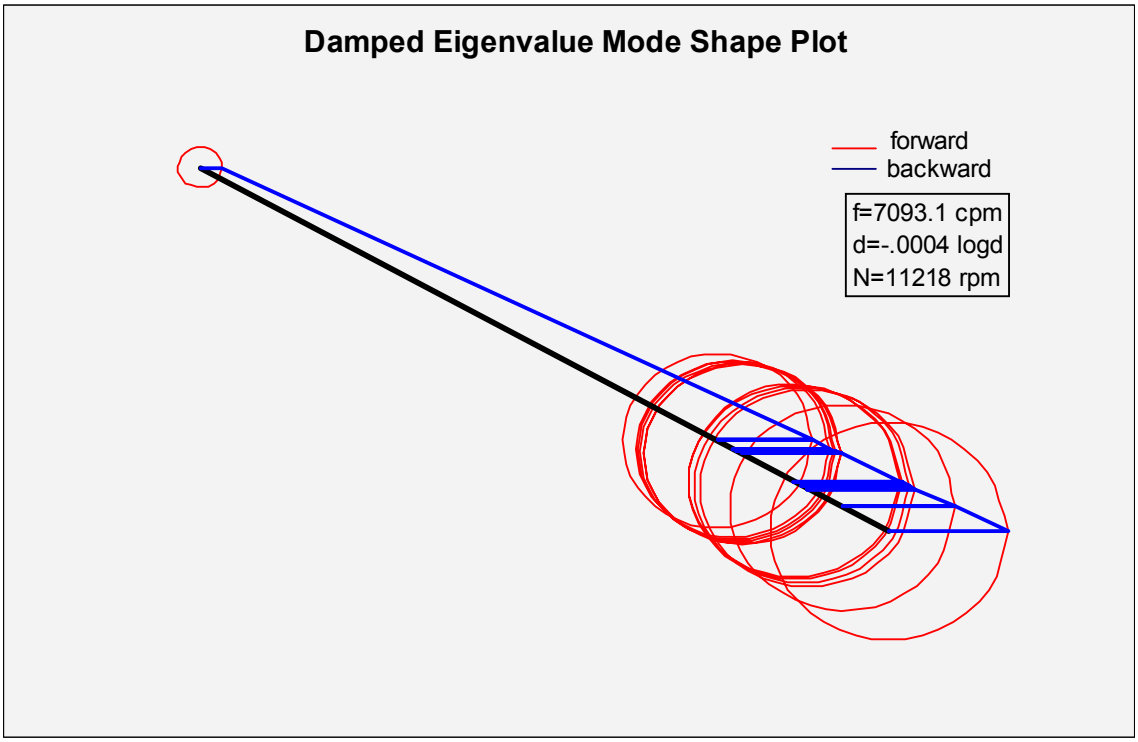

Fig. 29 3D 1st forward mode shape plot at the running speed of 11,218 rpm with Wachel's model

XLTRC analysis of the same rotor model is done with the compressible code model having radially upward flow on the back shroud, and the rotordynamic matrices for changing speed is given in Appendix B. Damping used to make the rotor go unstable at the design running speed is retained and Wachel's model is replaced by the compressible code model. Table 14 gives the damped natural frequencies for different running speeds with the compressible code model having upward flow on the back shroud. The compressible code model predicts a higher margin of stability. At a speed of 11,218 rpm, the log decrement δ is still positive with the 1st forward critical at 7093 cpm as shown in Fig. 30. Thus the Wachel's model predicts a lower onset speed of instability when compared to the full model of force and moment with radially outward flow.

Table 14 Damped eigenvalues with radially outward leakage on the back shroud for complete force and moment model

Speed	logd1	cpm1	logd2	cpm2
1000.	0.048	6157.6	0.024	6315.5
2000.	0.062	6078.7	0.039	6388.5
3000.	0.083	6001.3	0.049	6461.9
4000.	0.111	5925.1	0.054	6535.7
5000.	0.144	5849.9	0.056	6610.0
6000.	0.182	5775.5	0.055	6685.0
7000.	0.224	5701.7	0.051	6760.9
8000.	0.267	5628.5	0.047	6837.7
9000.	0.311	5555.5	0.041	6915.7
10000.	0.356	5482.8	0.035	6994.9
11000.	0.399	5410.2	0.030	7075.4
11218.	0.407	5394.4	**0.029**	**7093.2**
13000.	0.474	5264.7	0.021	7241.1

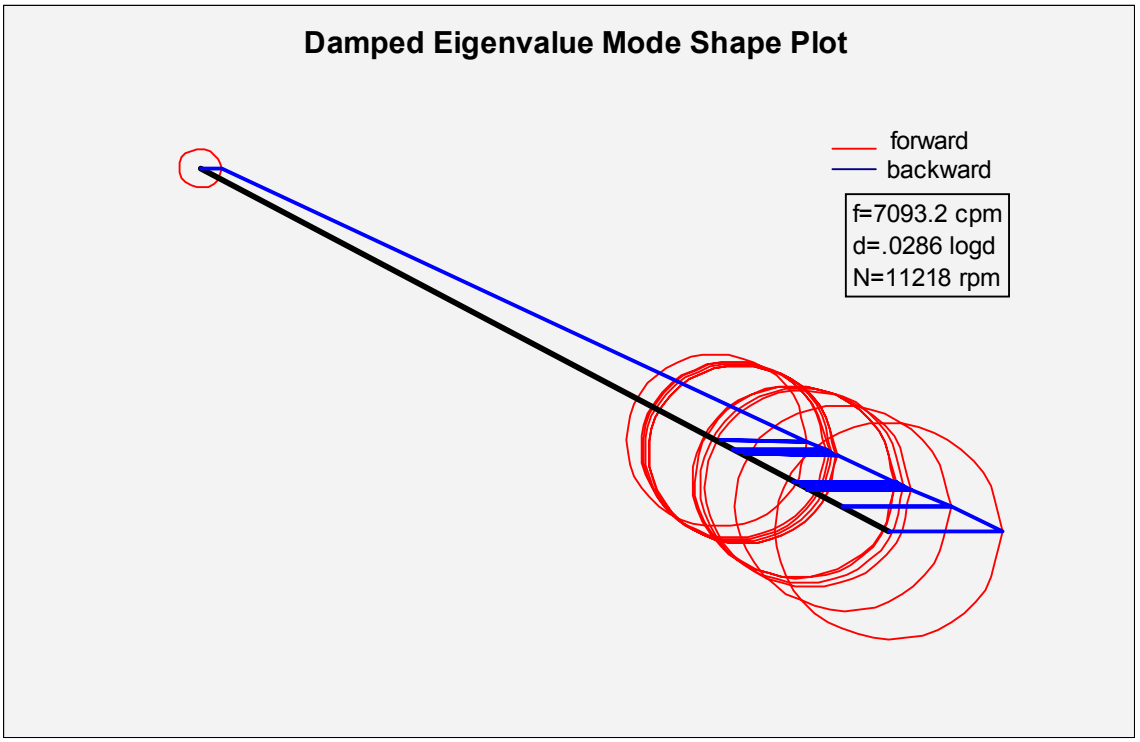

Fig. 30 3D 1st forward mode shape plot at 11,218 rpm with radially outward leakage on the back shroud for complete force and moment model

To examine the influence of leakage downward on the back shroud, XLTRC analysis of the same rotor model with the damping $C_{xx} = C_{yy} = 6650$ N-s/m and $C_{\alpha x \alpha x} = C_{\varepsilon y \alpha y} = 1.15$ N-ms/rad retained at the bearing 1, and rotordynamic matrices

replaced by new rotordynamic matrices (Appendix B) corresponding to upward leakage on back shroud is done**.** Table 15 gives the damped eigenvalues with compressible code model with radially inward leakage on the back shroud. Table 15 shows that at about 11,218 rpm, the log decrement δ corresponding to first forward mode is 0.005, which is smaller than that predicted for the radially outward flow at the same speed (δ = 0.029). Thus the model predicts a greater destabilizing affect with flow downward on the back shroud than with flow upward on the back shroud. Mode shape plot at 11,218 rpm for the 1st forward is shown in Fig. 31, which is a typical cantilever mode shape having maximum displacement at the free end.

Table 15 Damped eigenvalues with radially inward leakage on the back shroud for complete force and moment model

Speed	logd1	cpm1	logd2	cpm2
1000.	0.039	6155.1	0.033	6314.4
2000.	0.058	6075.9	0.043	6386.4
3000.	0.084	5997.9	0.049	6459.2
4000.	0.115	5921.1	0.052	6533.1
5000.	0.152	5845.4	0.052	6608.2
6000.	0.193	5771.0	0.050	6684.8
7000.	0.239	5697.8	0.045	6763.3
8000.	0.288	5626.0	0.038	6843.8
9000.	0.340	5555.7	0.029	6926.5
10000.	0.395	5486.8	0.019	7011.8
11000.	0.451	5419.5	0.008	7099.8
11218.	0.464	5405.1	**0.005**	**7119.3**
13000.	0.566	5290.2	-0.018	7284.6

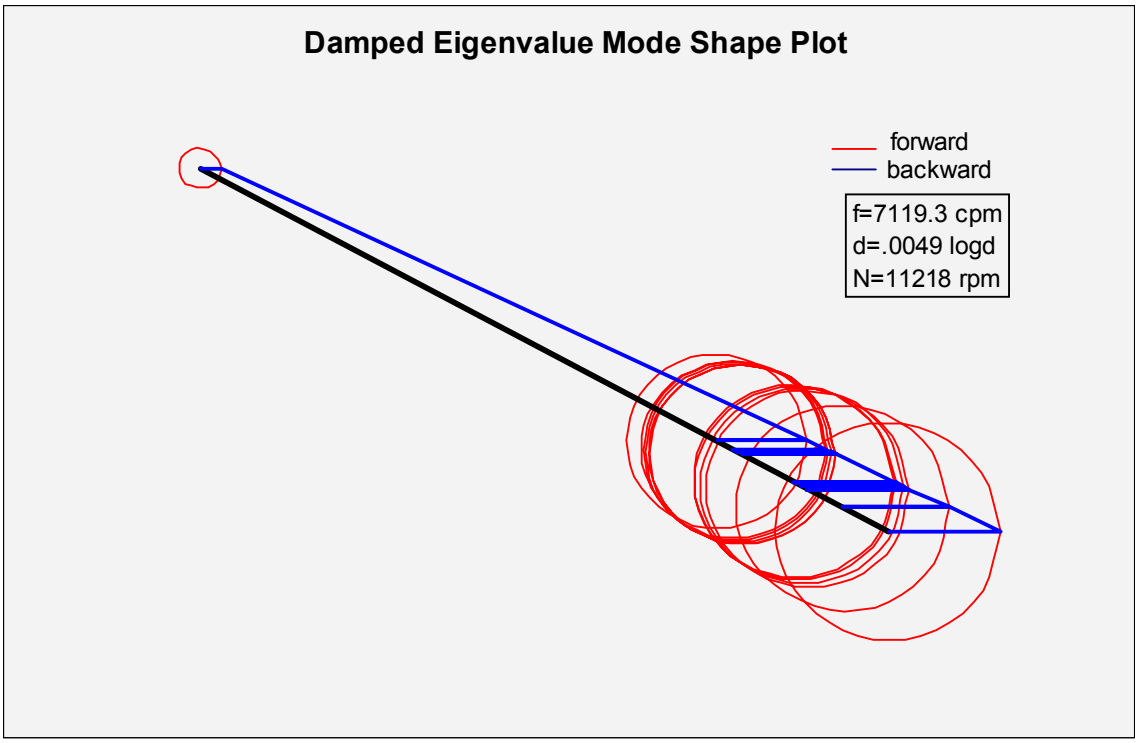

Fig. 31 3D 1st forward mode shape plot at 11,218 rpm with radially inward leakage on the back shroud for complete force and moment model

Since Wachel's model only considers the forces acting on the rotor and neglects any moment acting on the rotor, it would raise a simple question; "what affect would only a force model (equation 2) have on the rotor neglecting the moments from the complete force and moment compressible code model?" Therefore to examine the influence of only the forces, only the rotordynamic force coefficients in equation (1) are retained. The rotordynamic matrices used for this case is given in Appendix B. Table 16 gives the damped eigenvalues for this reduced model with upward leakage on the back shroud. At about 11,218 rpm, the predicted log decrement δ is 0.041, which is higher than that predicted by the complete force and moment model (δ=0.029) in Table 14. Thus a reduced model for forces due to displacement perturbations only predicts a higher margin of stability (bigger log decrement δ). Mode shape plot of the rotor (Fig. 32) with the force-only model at 11,218 rpm shows a forward precession of 7084 cpm and a typical cantilever mode shape.

Table 16 Damped eigenvalues with leakage upward on the back shroud and considering only the forces due to displacement perturbations

Speed	logd1	cpm1	logd2	cpm2
1000.	0.046	6160.2	0.023	6317.2
2000.	0.057	6083.2	0.038	6391.3
3000.	0.073	6008.0	0.049	6465.5
4000.	0.096	5934.3	0.055	6539.8
5000.	0.123	5861.9	0.059	6614.2
6000.	0.153	5790.6	0.060	6688.9
7000.	0.187	5720.1	0.059	6763.8
8000.	0.223	5650.2	0.056	6839.1
9000.	0.260	5580.8	0.052	6914.8
10000.	0.298	5511.6	0.047	6991.1
11000.	0.334	5442.3	0.042	7068.0
11218.	0.342	5427.2	**0.041**	**7084.9**
13000.	0.401	5303.1	0.033	7224.1

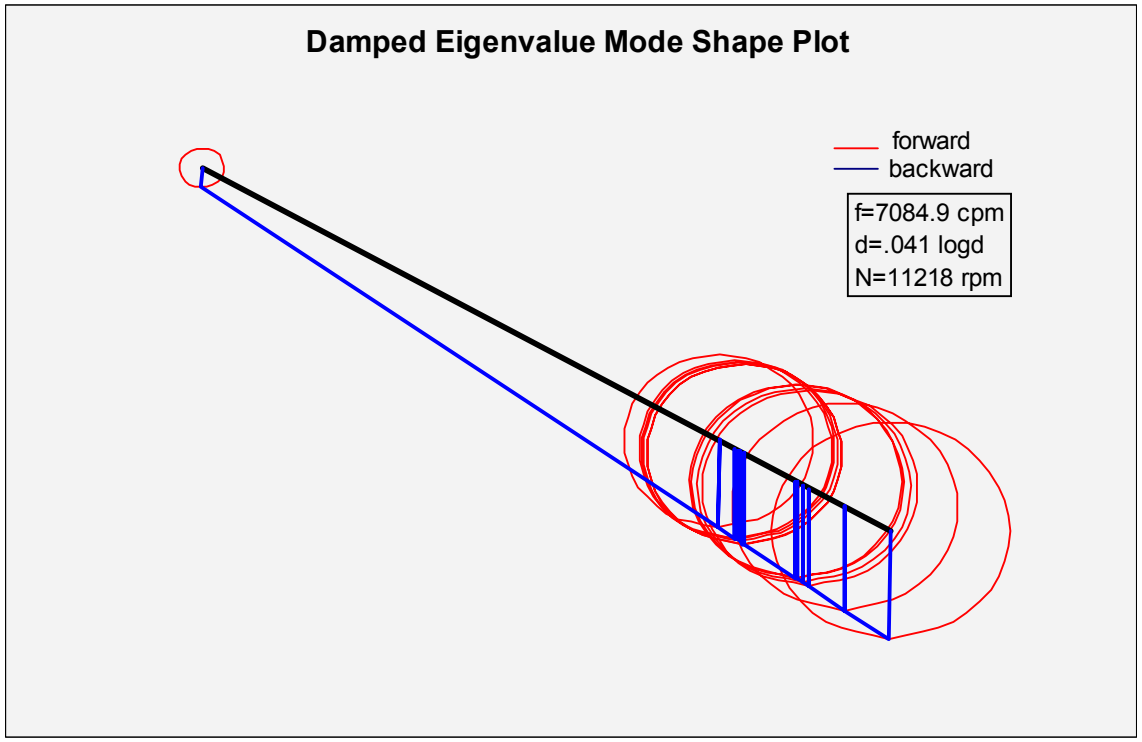

Fig. 32 3D 1st forward mode shape plot at 11,218 rpm with a force-only model having outward flow on back shroud

Having answered the question that the reduced model including only forces has a higher margin of stability with flow upward on the back shroud, we will now check if the same result is true for the case with flow downward. Table 17 gives the damped eigenvalues with reduced force model considering only the forces due to displacement perturbations and leakage on back shroud inward. The model predicts the rotor will go unstable at 13,000 rpm, and the log decrement δ is 0.017 at the design speed. Thus a force-only model is less conservative than the complete force and moment model. 1st forward mode shape plot in Fig. 33 predicts that at 11,218 rpm the rotor would have a forward precession at 7085 cpm.

Table 17 Damped eigenvalues with leakage inward on the back shroud and considering only the forces due to displacement perturbations

Speed	logd1	cpm1	logd2	cpm2
1000.	0.037	6158.8	0.032	6317.1
2000.	0.052	6083.1	0.041	6390.9
3000.	0.073	6009.2	0.049	6464.8
4000.	0.098	5936.8	0.053	6538.7
5000.	0.127	5865.9	0.055	6612.9
6000.	0.161	5796.4	0.054	6687.3
7000.	0.198	5728.0	0.051	6762.2
8000.	0.238	5660.7	0.046	6837.6
9000.	0.282	5594.4	0.039	6913.7
10000.	0.328	5529.0	0.030	6990.6
11000.	0.377	5464.4	0.020	7068.4
11218.	0.388	5450.4	**0.017**	**7085.5**
13000.	0.480	5337.2	-0.007	7227.5

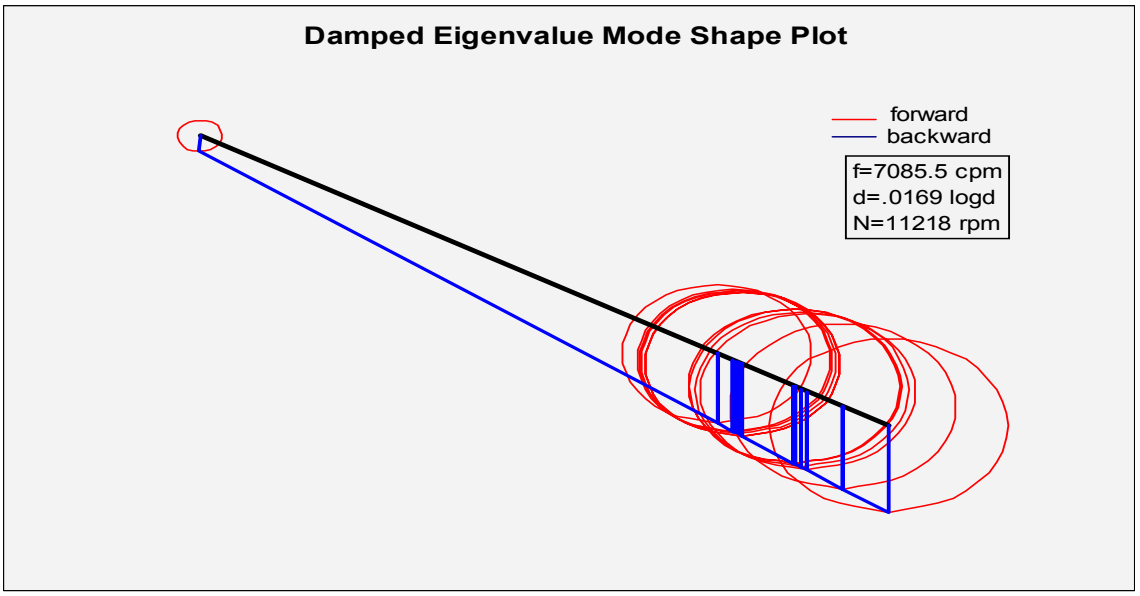

Fig. 33 3D 1st forward mode shape plot at the 11,218 rpm with a force-only model having inward flow on back shroud

If only the moment due to slope perturbations (equation 65) were considered on the rotor system with no damping retained from the original model at bearing 2, we see that the model predicts the rotor to go unstable at 11,000 rpm (Table 18) with radially outward leakage. Thus the moments due to slope perturbations have a destabilizing influence on the rotor. 1st forward mode shape at 11,000 rpm is shown in Fig. 34. Negative log decrement is not seen if damping is retained.

Table 18 Damped eigenvalues with leakage outward on the back shroud and considering only the moments due to slope perturbations

Speed	logd1	cpm1	logd2	cpm2
1000.	0.001	6156.1	0.000	6310.8
2000.	0.002	6077.3	0.001	6387.5
3000.	0.003	5997.8	0.001	6464.3
4000.	0.005	5917.8	0.001	6541.4
5000.	0.007	5837.5	0.001	6618.8
6000.	0.009	5757.0	0.000	6696.4
7000.	0.012	5676.4	0.000	6774.4
8000.	0.014	5596.0	0.000	6852.7
9000.	0.017	5515.8	0.000	6931.3
10000.	0.020	5436.0	0.000	7010.3
11000.	0.022	5356.9	-0.001	7089.6
11218.	0.023	5339.8	**-0.001**	**7107.0**
13000.	0.027	5201.2	-0.001	7249.3

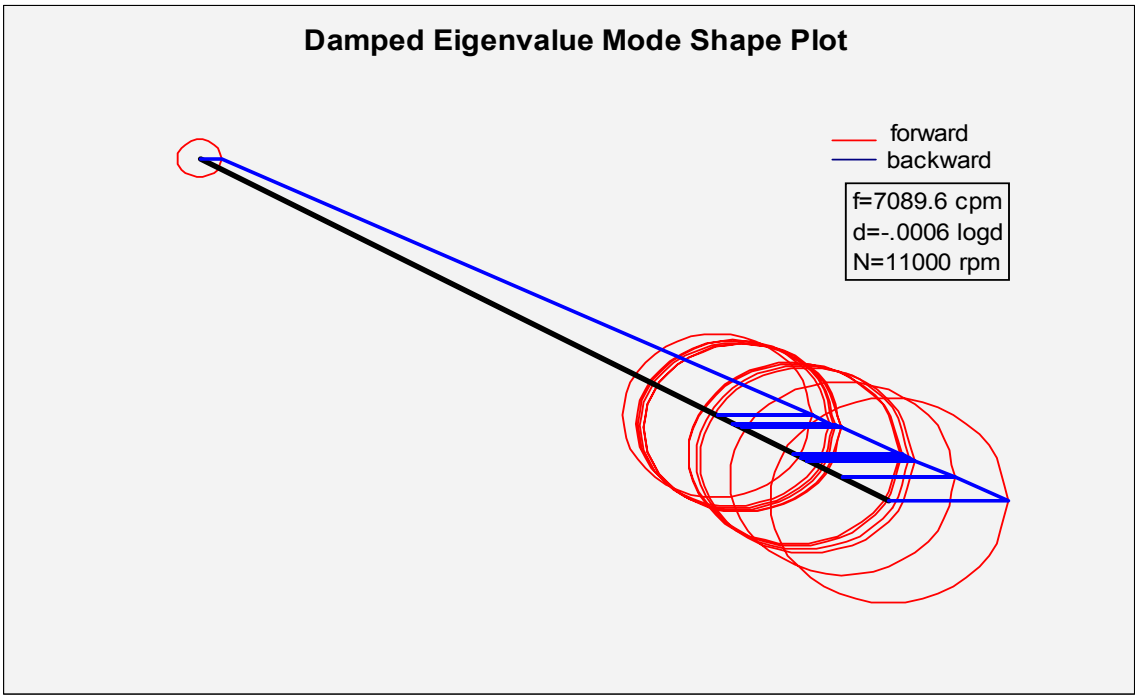

Fig. 34 3D 1st forward mode shape plot at the 11,000 rpm with a moment-only model having outward flow on back shroud

With a moment-only model for the inward leakage on the back shroud, and no damping retained from the original model at bearing 2, rotor is predicted to be stable (Table 19). Thus the moment due to slope perturbations are less destabilizing for the inward leakage on the back shroud than the upward leakage on the back shroud.

Table 19 Damped eigenvalues with leakage inward on the back shroud and considering only the moments due to slope perturbations

Speed	logd1	cpm1	logd2	cpm2
1000.	0.001	6155.1	5.77E-04	6309.8
2000.	0.002	6074.6	9.61E-04	6385.8
3000.	0.003	5993.3	1.18E-03	6462.4
4000.	0.005	5911.4	1.28E-03	6539.7
5000.	0.007	5829.1	1.28E-03	6618.0
6000.	0.010	5746.9	1.22E-03	6697.3
7000.	0.013	5664.8	1.11E-03	6777.7
8000.	0.016	5583.3	9.90E-04	6859.2
9000.	0.019	5502.5	8.73E-04	6941.9
10000.	0.022	5422.8	7.79E-04	7026.0
11000.	0.025	5344.5	7.24E-04	7111.3
11218.	0.025	5327.6	7.19E-04	7130.1

INFLUENCE OF SURGE CONDITIONS

Surge is a phenomenon of considerable interest; yet is not fully understood. It is a form of unstable operation and unfortunately it occurs frequently in the process industry, sometimes with damaging results. This condition occurs when there is sufficient aerodynamic instability from the cross-coupling forces within the compressor that the compressor is unable to produce adequate pressure to deliver continuous flow to the downstream system. The underlying cause of surge is aerodynamic stall, which may occur in either the impeller or the diffuser. With high-pressure compressors, operation in the incipient surge range is accompanied by asynchronous vibrations which can reach predominant amplitudes, and result in thrust and journal bearing failure, impeller and seal rub, impeller hub and/or shroud failures. Surge conditions frequently result in rubbed labyrinth seals. A labyrinth seal rub condition is simulated by simultaneously increasing the labyrinth clearance and reducing the tooth height. Table 20 shows the change in the leakage rate, seal inlet tangential velocity, and the rotordynamic coefficients for the front shroud and eye seal with increased clearance and reduced tooth height for the eye seal. Note that both the leakage rate $\dot{m}$ and the eye seal inlet tangential velocity $u_{\theta 0}$ increases with the simultaneous increase in clearance and decrease in tooth height for the eye seal. Whirl frequency ratio f_w, which is a direct measure of stability, also increases with the increase in leakage and the tangential velocity $u_{\theta 0}$. This result predicts that a surge event that rubs the labyrinths will decrease the system's margin of stability.

For the back shroud and interstage seal, Table 21 shows the change in the leakage rate, rotordynamic coefficients and the whirl frequency ratio with increased clearance and reduced tooth height of the interstage seal having an upward flow. It is seen that the leakage rate $\dot{m}$ increases but the whirl frequency ratio f_w of the combined impeller and seal nearly remains constant, because in the case of upward flow on the back shroud, the seal inlet tangential velocity $u_{\theta 0}$ does not change.

Table 20 Front shroud – eye seal results for varying clearance and tooth height

Clearance (Cr) Tooth Height (B)	Cr x1=0.1524 mm B/1=2.794mm	Cr x2=0.3048 mm B/2=1.397mm	Cr x3=0.4572 mm B/3=0.9313mm
$\dot{m}$ (Kg/sec)	0.539	1.1364	1.722
Seal inlet $u_{\theta 0}$	0.646	0.80	0.895
Seal k (N/m)	8.3348E+05	5.375E+05	3.793E+05
Seal C (N-s/m)	1098.5	571.99	360.79
Impeller k (N/m)	21972	48684	74411
Impeller C (N-s/m)	29.084	48.684	67.646
Impeller WFR f_w	0.64309	0.85124	0.93637
Seal WFR f_w	0.646	0.8	0.895

Table 21 Back shroud – interstage seal results for varying clearance and tooth height with flow upwards

Clearance (Cr) Tooth Height (B)	Cr x1=0.127 mm B/1=1.778mm	Cr x2=0.254 mm B/2=0.889mm	Cr x3=0.381 mm B/3=0.5926mm
$\dot{m}$ (Kg/sec)	0.226	0.493	0.764
Seal inlet $u_{\theta 0}$	0.5	0.5	0.5
Seal k (N/m)	0.17361E+06	82076	53689
Seal C (N-s/m)	306.06	146.72	93.840
Impeller k (N/m)	31.527	25.583	9.6746
Impeller C (N-s/m)	0.68020E-01	0.12937E-01	0.51717E-01
Impeller WFR f_w	0.39454	1.6833	0.15924
Seal WFR f_w	0.4829	0.4762	0.4870
Combined WFR f_w	0.482	0.4764	0.4874

Table 22 shows the change in the leakage rate, rotordynamic coefficients and the whirl frequency ratio with increased clearance and reduced tooth height of the interstage seal having an inward flow. It is seen that the leakage rate $\dot{m}$ increases but the whirl frequency ratio f_w of the combined impeller and seal decreases. This is because in the case of inward flow on the back shroud, the seal inlet tangential velocity $u_{\theta 0}$ decreases. The overall influence of seal rub is increased leakage and reduced stability as the eye seal coefficients are bigger than the interstage seal coefficients.

Table 22 Back shroud – interstage seal results for varying clearance and tooth height with flow inwards

Clearance (Cr) Tooth Height (B)	Cr x1=0.127 mm B/1=1.778mm	Cr x2=0.254 mm B/2=0.889mm	Cr x3=0.381 mm B/3=0.5926mm
$\dot{m}$ (Kg/sec)	0.290377	0.6182	0.944
Seal inlet $u_{\theta 0}$	0.8973	0.796	0.715
Seal k (N/m)	3.996E+05	1.73E+05	9.767E+04
Seal C (N-s/m)	379.17	185.82	116.31
Impeller k (N/m)	134.57	222.50	308.43
Impeller C (N-s/m)	0.20535	0.30426	0.39152
Impeller WFR f_w	0.55784	0.62249	0.67059
Seal WFR f_w	0.897	0.796	0.715

CODE APPLICATIONS

Some of the important applications of this code are:

1. Destabilizing forces and moments due to eye seal, interstage seal, and front and back shroud obtained separately, as opposed to Wachel's all in one force-only model.
2. Influences of surge conditions can be examined by changing the seal clearances and decreasing the tooth height to simulate rub conditions.
3. Shunt hole injection feature can be examined for the balance piston or division wall labyrinth seal.
4. Impeller geometry and clearances can be optimized.
5. Reasonable estimation of the leakage can be known.
6. Labyrinth seal design can be optimized.

SUMMARY AND CONCLUSIONS

An analysis has been developed for the forces and moments on the shroud of an impeller using a compressible bulk flow model. Validation steps include making direct comparisons to measured moment coefficients by Japanese researchers at Osaka University [25] and [30]. The comparison show that the bulk-flow model can simulate the flow fairly well, and a reasonable match is obtained for the cross-coupled stiffness k and the direct damping C. Keeping in mind that the cross-coupled stiffness k and direct damping C are important for stability; the bulk-flow model does an adequate job. The compressible flow model is also verified by comparing to Child's [8] incompressible flow model.

Stability predictions of Wachel's empirical model and the compressible code model are done by using XLTRC. It is shown that there is a reasonable match between the two models, especially if inward leakage is considered. It is also found that inlet swirl can increase the cross-coupled stiffness and therefore influence stability, something Wachel's model does not account for. Based on the analysis done, the following conclusions can be made:

1) Wachel's model predicts a slightly lower onset speed of instability.
2) Fluid forces become more destabilizing with increasing leakage due to increase in the eye seal clearance and decrease in tooth height.
3) Increasing interstage seal clearance with radially outward flow on the back shroud is insensitive to interstage seal whirl frequency ratio f_w.
4) Swirl and mass flow rate increases with increasing eye seal clearances.
5) Rotordynamic force coefficients for the back shroud are negligible compared to the front shroud and seal coefficients.
6) Interstage seal coefficients are comparable to the eye seal coefficients and cannot be ignored, as otherwise suggested by Fulton [9]
7) Front shroud rotordynamic coefficients are small compared to the labyrinth seals, but the values become comparable for increased seal clearances.
8) Radially inward flow on the back shroud is more destabilizing than radially outward flow.

9) Good estimation of the cross coupled stiffness k and direct damping C is possible using bulk-flow model.
10) Reasonable estimation of the destabilizing transverse moment is possible using the bulk-flow model.
11) Based on the predictions, shunt hole injection has the affect of changing the flow field of the division wall or balance piston, and has no major influence on the back shroud. This change of flow field can easily be accomplished by a swirl brake.

By using variable impeller geometry and calculating the pressure and velocity distribution along the impeller and seal leakage path, a physically meaningful interpretation of what happens inside the leakage path can be known. Improvements in the model might be achieved by incorporating energy equation to account for changing temperature. Different speed data would be needed to have a better comparison of the two models. Another drawback of the code is that it works only when there is leakage. Thus an alternative procedure would have to be developed to account for zero leakage.

In conclusion this compressible model would be an important improvement, since the currently used Wachel's model does not give the separate contribution of seals and impellers nor does it gives a physical interpretation of the flow along impeller and seal geometry. Thus overall using a simple bulk flow approach, it is possible to calculate the rotordynamic coefficients for rotor stability and predict the stability.

REFERENCES

[1] http://www.dresser-rand.com/newsroom/photo_gallery.asp (Picture accessed on 15th Dec 2005.)

[2] Childs, D., 1993, *Turbomachinery Rotordynamics: Phenomena, Modeling, & Analysis*, John Wiley & Sons, New York.

[3] API, 2002, *Axial and Centrifugal Compressors and Expander-Compressors for Petroleum, Chemical and Gas Industry Services*, API Standard 617, Seventh Edition, American Petroleum Institute, Washington, D.C.

[4] Boyce, M. P., 2003, *Centrifugal Compressors: A Basic Guide*, PennWell Corporation, Tulsa, Oklahoma.

[5] Fowlie, D. W., and Miles, D. D., 1975, "Vibration Problems with High Pressure Centrifugal Compressors," ASME Paper, n75-Pet-28.

[6] Wyssmann, H. R., 1988, "Rotor Stability of High Pressure Multistage Centrifugal Compressors," ASME Journal of Vibration, Acoustics, Stress, and Reliability in Design, **110**, pp.185-192.

[7] Childs, D. W., 1982, "Finite-Length Solutions for Rotordynamic Coefficients of Turbulent Annular Seals," ASME Paper, 82-LUB-42.

[8] Childs, D., 1989, "Fluid-Structure Interaction Forces at Pump-Impeller-Shroud Surfaces for Rotordynamic Calculations," Journal of Vibrations, Acoustics, Stress, and Reliability in Design, **111**, pp. 216-225.

[9] Fulton, J. W., 2003, "Rotor Stability Criteria for Multi-Stage Centrifugal Compressors," Proceedings of the ASME Design Engineering Technical Conference, **5 B**, pp. 1327-1336.

[10] Picardo, A, Wade, J. L., Phillips, S. G., and Childs, D. W., 2002, "High Pressure Experimental Rotordynamic Coefficient Results for 0.207 mm Radial Clearance Labyrinth Seals with High Pre-Swirl," Texas A&M University.

[11] Picardo, A, Wade, J. L., Phillips, S. G., and Childs, D. W., 2002, "High Pressure Experimental Rotordynamic Coefficient Results for 0.207 mm Radial Clearance Labyrinth Seals with Medium Pre-Swirl," Texas A&M University.

[12] Jery, B., Acosta, A. J., Brennen, C. E., and Caughy, T. K., 1985, "Forces on Centrifugal Pump Impellers," Proceedings of the 2nd International Pump Symposium, Houston, Texas, pp. 21-32.

[13] Guinzburg, A., 1992, "Rotordynamic Forces Generated by Discharge-to-Suction Leakage Flows in Centrifugal Pumps," California Institute of Technology, Division of Engineering and Applied Science, Report No. E249.14, Pasadena, California.

[14] Hergt, P. and Krieger, P., 1970, "Radial Forces in Centrifugal Pumps with Guide Vanes," Advance Class Boiler Feed Pumps, Proceedings of the Institute of Mechanical Engineers, **184**(3N), pp. 101-107.

[15] Bolleter, U., Wyss, A., Welte, I., and Sturchler, R., 1987, "Measurement of Hydrodynamic Interaction Matrices of Boiler Feed Pump Impellers," ASME Journal of Vibration, Acoustics, Stress, and Reliability in Design, **109**(2), pp.144-151.

[16] Shoji, H., and Ohasi, H., 1980, "Fluid Forces on Rotating Centrifugal Impeller with Whirling Motion," Rotodynamic Instability Problems in High Performance Turbomachinery, NASA CP No. 2133.

[17] Franz, R. and Arndt, N., 1986, "Measurements of Hydrodynamic Forces on a Two-Dimensional Impeller and a Modified Centrifugal Pump," California Institute of Technology, Division of Engineering and Applied Science, Report No. E249.4, Pasadena, California.

[18] Franz, R., Arndt, N., Caughey, T. K., Brennen, C .E., and Acosta, A. J., 1987, "Rotordynamic Forces on Centrifugal Pump Impellers," Proceedings of the Eight Conference on Fluid Machinery, Akademiai Kiado, Budapest, Hungary, **1**, pp.252-258.

[19] Bolleter, U., Wyss, A., Welte, I., and Sturchler, R., 1985, "Measurement of Hydrodynamic Matrices of Boiler Feed Pump Impellers," ASME Paper 85-DET-147.

[20] Thomas, H., 1958, "Instabile Eigenschwingungen von Turbinenlaufern angefacht durch die Spaltstromungen Stopfbuschen und Beschauflungen," Bull de L'AIM, **71**, pp.1039-1063.

[21] Alford, J., 1965, "Protecting Turbomachinery from Self-Excited Rotor Whirl," Journal of Engineering for Power, **87**, pp.333-344.

[22] Wachel, J. C., and von Nimitz, W. W., 1981, "Ensuring the Reliability of Offshore Gas Compressor Systems," Journal of Petroleum Technology, Nov., pp.2252-2260.

[23] Wachel, J.C., 1982, "Rotordynamic Instability Field Problems," Rotordynamic Instability Problems in High-Performance Turbomachinery, NASA Conference Publications, College Station, Texas, pp.1-18.

[24] Ohashi, H., Imai, H. and Tsuchihashi, T., 1991, "Fluid Force and Moment on Centrifugal Impellers in Precession Motion," ASME Fluid Engineering Division **119**, pp.57-60.

[25] Yoshida, Y., Saito, A., Ishizaki, S., and Tsujimoto, Y., 1996, "Measurement of the Flow in the Backshroud/Casing Clearance of a Precessing Centrifugal Impeller," Proceedings of the 6th International Symposium on Transport Phenomena and Dynamics of Rotating Machinery, Honolulu, Hawaii, **2**, pp. 151-160.

[26] Cao, N.T., 1993, "Compressibility Effects on Rotor Forces in the Leakage Path between a Shrouded Pump Impeller and Its Housing," M.S. Thesis, Texas A&M University, Mechanical Engineering Department, College Station.

[27] Hirs, G.G., 1973, "A Bulk-Flow Theory for Turbulence in Lubricant Film," ASME Journal of Lubrication Technology, April, pp. 137-146.

[28] Childs, D. W., and Scharrer, J. K., 1986, "An Iwatsubo-Based Solution for Labyrinth Seals: Comparison to Experimental Results," ASME Journal of Engineering for Gas Turbines and Power, **108**, pp. 325-330.

[29] Press, W. H., Teukolsky, S. A., Vetterling, W. T., and Flannery, B. P., 1997, *Numerical Recipes in FORTRAN: The Art of Scientific Computing*, Cambridge University Press, New York.

[30] Tsujimoto, Y., Yoshida, Y., Ohashi H., Teramoto, N., and Ishizaki, S., 1997, "Fluid Force Moment on a Centrifugal Impeller Shroud in Precessing Motion," ASME Trans., Journal of Fluids Engineering, **119**, pp. 366-371.

[31] Iwatsubo, T., 1980, "Evaluation of Instability Forces of Labyrinth Seals in Turbines or Compressors," Rotordynamic Instability Problems in High-Performance Turbomachinery, NASA CP No.2133.

APPENDIX A

$$A_{1S} = [\sigma_s(1-ms) + \sigma_r(1-mr)]u_{s0}^2 / 2h_0 \quad \textbf{(A.1)}$$

$$A_{2S} = -\frac{2u_{\theta 0}}{b^2 r}\frac{dr}{ds} + [\sigma_s(1+ms)\beta_1 + \sigma_r(1+mr)\beta_0]u_{s0}/2 \quad \textbf{(A.2)}$$

$$A_{3S} = \frac{du_{s0}}{ds} + [(2+ms)\sigma_s + (2+mr)\sigma_r]u_{s0}/2 \quad \textbf{(A.3)}$$
$$-[(1+mr)\sigma_r\beta_0(u_{\theta 0} - r) + (1+ms)\sigma_s\beta_1 u_{\theta 0}]/2$$

$$A_{4s} = [(\sigma_r mr + \sigma_s ms)]u_{s0}^2 / 2k_1 - \frac{1}{\widetilde{\rho}_0 k_1}\frac{dp_0}{ds} \quad \textbf{(A.4)}$$

$$A_{5S} = 1 - u_{s0}^2 / k_1 \quad \textbf{(A.5)}$$

$$A_{6S} = \frac{1}{h_0}\frac{dh_0}{ds} + \frac{1}{\widetilde{\rho}_0}\frac{d\widetilde{\rho}_0}{ds} + \frac{1}{r}\frac{dr}{ds} \quad \textbf{(A.6)}$$

$$A_{1\theta} = u_{s0}\left[(1-mr)(u_{\theta 0} - r)\sigma_r + (1-ms)u_{\theta 0}\sigma_s\right]/2h_0 \quad \textbf{(A.7)}$$

$$A_{2\theta} = u_{s0}(\sigma_r + \sigma_s)/2 + \sigma_r(mr+1)(u_{\theta 0} - r)\beta_0/2 \quad \textbf{(A.8)}$$
$$+\sigma_s(ms+1)u_{\theta 0}\beta_1/2 + \frac{u_{s0}}{r}\frac{dr}{ds}$$

$$A_{3\theta} = \frac{\sigma_r (u_{\theta 0} - r)}{2}\left[mr - (1+mr)\beta_0 (u_{\theta 0} - r)/u_{s0}\right] \quad \textbf{(A.9)}$$

$$+\frac{\sigma_s u_{\theta 0}}{2}\left[ms - (1+ms)\beta_1 u_{\theta 0}/u_{s0}\right]$$

$$A_{4\theta} = [\sigma_r (u_{\theta 0} - r)mr + \sigma_s u_{\theta 0} ms] \quad \textbf{(A.10)}$$

$$\sigma_s = (L_s / H_0)\lambda_s \ , \ \sigma_r = (L_s / H_0)\lambda_r \quad \textbf{(A.11)}$$

$$\lambda_s = nsR_{\alpha 0}^{ms}[1 + (u_{\theta 0}/bu_{s0})^2]^{\frac{ms+1}{2}} \quad \textbf{(A.12)}$$

$$\lambda_r = nrR_{\alpha 0}^{mr}\{1 + [(u_{\theta 0} - r)/bu_{s0}]^2\}^{\frac{mr+1}{2}} \quad \textbf{(A.13)}$$

$$\beta_0 = \frac{(u_{\theta 0} - r)}{b^2 u_{s0}}\left\{1 + [(u_{\theta 0} - r)/bu_{s0}]^2\right\}^{-1} \quad \textbf{(A.14)}$$

$$\beta_1 = \frac{u_{\theta 0}}{b^2 u_{s0}}\left\{1 + (u_{\theta 0}/bu_{s0})^2\right\}^{-1} \quad \textbf{(A.15)}$$

$$\Gamma = \omega(f - u_{\theta 0}/r) \quad \textbf{(A.16)}$$

$$F_1 = \left(\frac{L^2}{C_i L_s}\right)\left[\left(\frac{dz}{ds}\right)^2 + z\frac{d^2 z}{ds^2}\right] + \left(\frac{R_i^2}{C_i L_s}\right)\left[\left(\frac{dr}{ds}\right)^2 + r\frac{d^2 r}{ds^2}\right] \quad \textbf{(A.17)}$$

$$F_2 = \frac{u_{s0}}{h_0}\left(\frac{d^2 z}{ds^2} - \frac{1}{h_0}\frac{dh_0}{ds}\frac{dz}{ds}\right) \quad \textbf{(A.18)}$$

$$F_3 = \frac{u_{s0}}{h_0}\left(F_1 - \frac{G_0}{h_0}\frac{dh_0}{ds}\right) \quad \textbf{(A.19)}$$

$$G_0 = \left(\frac{L^2}{C_i L_s}\right)z\frac{dz}{ds} + \left(\frac{R_i^2}{C_i L_s}\right)r\frac{dr}{ds} \quad \textbf{(A.20)}$$

APPENDIX B

Speed: 4000 rpm

Front shroud and eye seal results in SI units.

Stiffness matrix from seal

8589.2	0.30900E+06
-0.30900E+06	8589.2

Damping matrix from seal

383.50	-51.424
51.424	383.50

Stiffness matrix front shroud

-616.47	3767.7	321.05	872.83
-3767.7	-616.47	872.83	-321.05
462.03	-1190.8	-237.15	-326.64
-1190.8	-462.03	326.64	-237.15

Damping matrix front shroud

10.486	7.5403	-2.7104	3.4593
-7.5403	10.486	3.4593	2.7104
-3.4772	-2.8844	1.1253	-2.9344
-2.8844	3.4772	2.9344	1.1253

Mass matrix front shroud

0.13260E-01	-0.93219E-03	-0.67886E-02	-0.15223E-03
0.93219E-03	0.13260E-01	-0.15223E-03	0.67886E-02
-0.57678E-02	-0.21354E-03	0.60240E-02	-0.13180E-03
-0.21354E-03	0.57678E-02	0.13180E-03	0.60240E-02

Speed: 6000 rpm

Front shroud and eye seal results in SI units:

Stiffness matrix from seal

29025.	0.62710E+06
-0.62710E+06	29025.

Damping matrix from seal

595.46	-116.51
116.51	595.46

Stiffness matrix front shroud

-1608.1	8044.5	805.51	1951.6
-8044.5	-1608.1	1951.6	-805.51
1214.8	-2540.9	-495.86	-738.52
-2540.9	-1214.8	738.52	-495.86

Damping matrix front shroud

16.129	14.605	-4.2912	7.0383
-14.605	16.129	7.0383	4.2912
-5.3574	-6.3113	1.8141	-6.5096
-6.3113	5.3574	6.5096	1.8141

Mass matrix front shroud

0.17005E-01	-0.69372E-03	-0.91408E-02	-0.63509E-04
0.69372E-03	0.17005E-01	-0.63509E-04	0.91408E-02
-0.82081E-02	-0.21629E-03	0.89226E-02	-0.14028E-03
-0.21629E-03	0.82081E-02	0.14028E-03	0.89226E-02

Speed: 8000 rpm

Front shroud and eye seal results in SI units:

Stiffness Matrix from seal

63528.	0.97474E+06 .
-0.97474E+06	63528.

Damping matrix from seal

804.63	-182.64
182.64	804.63

Stiffness matrix front shroud

-3300.8	13210.	1491.7	3274.9
-13210.	-3300.8	3274.9	-1491.7
2284.8	-4170.7	-667.88	-1263.1
-4170.7	-2284.8	1263.1	-667.88

Damping matrix front shroud

21.558	23.916	-5.8502	11.930
-23.916	21.558	11.930	5.8502
-7.1643	-11.042	2.5246	-11.478
-11.042	7.1643	11.478	2.5246

Mass matrix front shroud

0.21017E-01 -0.74886E-03 -0.11677E-01 -0.10969E-03
0.74886E-03 0.21017E-01 -0.10969E-03 0.11677E-01
-0.10772E-01 -0.12120E-03 0.11912E-01 -0.98922E-04
-0.12120E-03 0.10772E-01 0.98922E-04 0.11912E-01

BACK SHROUD UPWARD LEAKAGE:

Units: SI

Speed: 4000 rpm

Stiffness matrix from seal

-583.54 26156.
-26156. -583.54

Damping matrix from seal

100.72 -0.90355
0.90355 100.72

Stiffness matrix back shroud

-2.7952 6.1314 -2.9701 -19.587
-6.1314 -2.7952 -19.587 2.9701
0.308E-01 0.62253 0.40777E-01 -1.0159
0.62253 -0.30890E-01 1.0159 0.40777E-01

Damping matrix back shroud

0.39848E-02 -0.15470E-02 -0.16824E-02 0.19202E-02
0.15470E-02 0.39848E-02 0.19202E-02 0.16824E-02
0.41433E-03 0.31341E-04 0.27270E-03 -0.39595E-04
0.31341E-04 -0.41433E-03 0.39595E-04 0.27270E-03

Mass matrix back shroud

-0.64762E-05 -0.21987E-05 -0.78738E-05 0.29316E-05
0.21987E-05 -0.64762E-05 0.29316E-05 0.78738E-05
0.11019E-06 -0.60732E-06 0.13447E-06 0.82420E-06
-0.60732E-06 -0.11019E-06 -0.82420E-06 0.13447E-06

Speed: 6000 rpm

Stiffness matrix from seal

-540.19 56898.
-56898. -540.19

Damping matrix from seal

156.38 -2.4188
2.4188 156.38

Stiffness matrix back shroud

-8.1179 15.424 -9.2178 -48.359
-15.424 -8.1179 -48.359 9.2178
0.9967E-01 1.0569 0.12950 -1.7246
1.0569 -0.99671E-01 1.7246 0.12950

Damping matrix back shroud

0.11718E-01 -0.49736E-02 -0.36075E-02 0.62985E-02
0.49736E-02 0.11718E-01 0.62985E-02 0.36075E-02
0.51792E-03 0.95988E-04 0.32822E-03 -0.12192E-03
0.95988E-04 -0.51792E-03 0.12192E-03 0.32822E-03

Mass matrix back shroud

-0.10407E-04	-0.38919E-05	-0.12725E-04	0.54860E-05
0.38919E-05	-0.10407E-04	0.54860E-05	0.12725E-04
0.18265E-06	-0.42513E-06	0.22315E-06	0.62783E-06
-0.42513E-06	-0.18265E-06	-0.62783E-06	0.22315E-06

Speed: 8000 rpm

Stiffness matrix from seal

299.02	96256.
-96256.	299.02

Damping matrix from seal

213.25	-3.7887
3.7887	213.25

Stiffness matrix back shroud

-16.791	26.464	-19.967	-86.114
-26.464	-16.791	-86.114	19.967
0.21712	1.1171	0.28612	-2.0903
1.1171	-0.21712	2.0903	0.28612

Damping matrix back shroud

0.26029E-01	-0.10607E-01	-0.50461E-02	0.13694E-01
0.10607E-01	0.26029E-01	0.13694E-01	0.50461E-02
0.87411E-03	0.20300E-03	0.57004E-03	-0.26140E-03
0.20300E-03	-0.87411E-03	0.26140E-03	0.57004E-03

Mass matrix back shroud

-0.14533E-04	-0.64473E-05	-0.18027E-04	0.93959E-05
0.64473E-05	-0.14533E-04	0.93959E-05	0.18027E-04
0.26158E-06	-0.55199E-06	0.32336E-06	0.75905E-06
-0.55199E-06	-0.26158E-06	-0.75905E-06	0.32336E-06

BACK SHROUD INWARD LEAKAGE:

Units: SI

Speed: 4000 rpm

Stiffness matrix from seal

4622.5	81005.
-81005.	4622.5

Damping matrix from seal

100.31	-18.163
18.163	100.31

Stiffness matrix back shroud

5.0606	12.560	40.714	-34.719
-12.560	5.0606	-34.719	-40.714
49.086	0.69243	261.46	-11.272
0.69243	-49.086	11.272	261.46

Damping matrix back shroud

0.44060E-01	0.13036	0.12071	-0.40900
-0.13036	0.44060E-01	-0.40900	-0.12071
0.42370E-01	0.39408	0.21746	-1.6504
0.39408	-0.42370E-01	1.6504	0.21746

Mass matrix back shroud

0.32717E-03	-0.13177E-04	0.10392E-02	0.50635E-04
0.13177E-04	0.32717E-03	0.50635E-04	-0.10392E-02
0.10426E-02	-0.13537E-04	0.44405E-02	0.55614E-04
-0.13537E-04	-0.10426E-02	-0.55614E-04	0.44405E-02

Speed: 6000 rpm

Stiffness matrix from seal

14491.	0.19628E+06
-0.19628E+06	14491.

Damping matrix from seal

162.17	-37.827
37.827	162.17

Stiffness matrix back shroud

23.725	31.590	165.37	-89.913
-31.590	23.725	-89.913	-165.37
191.65	-2.2409	1024.8	-23.756
-2.2409	-191.65	23.756	1024.8

Damping matrix back shroud

0.77844E-01	0.29924	0.21811	-0.94140
-0.29924	0.77844E-01	-0.94140	-0.21811
0.88379E-01	0.91974	0.42426	-3.8641
0.91974	-0.88379E-01	3.8641	0.42426

Mass matrix back shroud

0.49881E-03 -0.18013E-04 0.15874E-02 0.64799E-04
0.18013E-04 0.49881E-03 0.64799E-04 -0.15874E-02
0.15964E-02 -0.22720E-04 0.68106E-02 0.79235E-04
-0.22720E-04 -0.15964E-02 -0.79235E-04 0.68106E-02

Speed: 8000 rpm

Stiffness matrix from seal

32002. 0.37123E+06
-0.37123E+06 32002.

Damping matrix from seal

233.87 -62.222
62.222 233.87

Stiffness matrix from seal

62.615 61.612
-61.612 62.615

Damping matrix back shroud

0.12058 0.53718 0.34271 -1.6974
-0.53718 0.12058 -1.6974 -0.34271
0.15001 1.6631 0.69664 -7.0274
1.6631 -0.15001 7.0274 0.69664

MASS MATRIX

0.67053E-03 -0.22790E-04 0.21442E-02 0.80243E-04
0.22790E-04 0.67053E-03 0.80243E-04 -0.21442E-02
0.21521E-02 -0.32186E-04 0.92245E-02 0.11016E-03
-0.32186E-04 -0.21521E-02 -0.11016E-03 0.92245E-02

SPEED: 11218 rpm

Pexit: 97 bar

Stiffness matrix from seal

86147.	0.82646E+06
-0.82646E+06	86147.

Damping matrix from seal

379.17	-117.18
117.18	379.17

Stiffness matrix back shroud

192.99	134.57	1275.0	-397.11
-134.57	192.99	-397.11	-1275.0
1410.0	-37.012	7649.5	-81.803
-37.012	-1410.0	81.803	7649.5

Damping matrix back shroud

0.20535	1.0721	0.58948	-3.4109
-1.0721	0.20535	-3.4109	-0.58948
0.28177	3.3589	1.2470	-14.219
3.3589	-0.28177	14.219	1.2470

Mass matrix back shroud

0.95645E-03	-0.30882E-04	0.30796E-02	0.10420E-03
0.30882E-04	0.95645E-03	0.10420E-03	-0.30796E-02
0.30833E-02	-0.48943E-04	0.13243E-01	0.15466E-03
-0.48943E-04	-0.30833E-02	-0.15466E-03	0.13243E-01

APPENDIX C

Front shroud and eye seal

Units: SI

With 2x clearance and 1/2height:
mass leakage rate= 1.1364Kg/sec
Tangential velocity ratio ($u_{\theta 0}$) seal inlet = 0.80

Stiffness matrix from seal

80475.	0.91271E+06
-0.91271E+06	80475.

Damping matrix from seal

571.99	-88.148
88.148	571.99

Stiffness matrix front shroud

-14771.	48684.	7051.4	11964.
-48684.	-14771.	11964.	-7051.4
9102.2	-15343.	-4523.6	-4320.7
-15343.	-9102.2	4320.7	-4523.6

Damping matrix front shroud

48.684	52.237	-13.143	25.697
-52.237	48.684	25.697	13.143
-16.404	-23.106	5.6833	-23.923
-23.106	16.404	23.923	5.6833

Mass matrix front shroud

0.30331E-01	-0.51399E-03	-0.16843E-01	0.18636E-03
0.51399E-03	0.30331E-01	0.18636E-03	0.16843E-01
-0.15180E-01	-0.55863E-03	0.16906E-01	-0.28477E-03
-0.55863E-03	0.15180E-01	0.28477E-03	0.16906E-01

With 3x clearance and 1/3height:

Stiffness matrix from seal

41413.	0.62631E+06
-0.62631E+06	41413

Damping matrix from seal

360.79	-36.367
36.367	360.79

Stiffness matrix front shroud

-21538.	74411.	10199.	17476.
-74411.	-21538.	17476.	-10199.
11798.	-23098.	-7198.5	-6106.1
-23098.	-11798.	6106.1	-7198.5

Damping matrix front shroud

67.646	58.987	-17.834	28.220
-58.987	67.646	28.220	17.834
-22.650	-24.152	7.5010	-24.893
-24.152	22.650	24.893	7.5010

Mass matrix front shroud

0.32963E-01	-0.86012E-03	-0.17940E-01	0.25482E-03
0.86012E-03	0.32963E-01	0.25482E-03	0.17940E-01
-0.15552E-01	-0.91223E-03	0.17126E-01	-0.45014E-03
-0.91223E-03	0.15552E-01	0.45014E-03	0.17126E-01

Back shroud and interstage seal with upward leakage
Units: SI
With 2x clearance and 1/2height

Stiffness matrix from seal

1103.1	82076
-82076.	1103.1

Damping matrix from seal

146.72	-0.66607
0.66607	146.72

Stiffness matrix back shroud

-30.680	25.583	-37.736	-196.09
-25.583	-30.680	-196.09	37.736
0.35897	8.9281	0.56855	-11.426
8.9281	-0.35897	11.426	0.56855

Damping matrix back shroud

-0.12937E-01	-0.49111E-01	-0.57703E-01	0.57889E-01
0.49111E-01	0.12937E-01	0.57889E-01	0.57703E-01
0.69813E-03	0.91888E-03	0.78360E-03	-0.10922E-02
0.91888E-03	-0.69813E-03	0.10922E-02	0.78360E-03

Mass matrix back shroud

0.39446E-04	-0.12884E-04	-0.47580E-04	0.17622E-04
0.12884E-04	0.39446E-04	0.17622E-04	0.47580E-04
0.73904E-06	-0.42820E-06	0.89406E-06	0.15309E-05
-0.42820E-06	-0.73904E-06	-0.15309E-05	0.89406E-06

With 3x clearance and 1/3height

Stiffness matrix from seal

449.84	53689
-53689.	449.84

Damping matrix from seal

93.840	-0.27587
0.27587	93.840

Stiffness matrix back shroud

-14.960	9.6746	-19.237	-213.22
-9.6746	-14.960	-213.22	19.237
0.48198E-01	15.404	0.26535	-24.968
15.404	-0.48198E-01	24.968	0.26535

Damping matrix back shroud

0.51717E-01	-0.62887E-01	-0.91880E-01	0.71700E-01
0.62887E-01	0.51717E-01	0.71700E-01	0.91880E-01
0.10040E-02	0.11712E-02	0.90317E-03	-0.13462E-02
0.11712E-02	-0.10040E-02	0.13462E-02	0.90317E-03

Mass matrix back shroud

0.50162E-04	-0.17501E-04	-0.60261E-04	0.22814E-04
0.17501E-04	0.50162E-04	0.22814E-04	0.60261E-04
0.94066E-06	-0.91847E-06	0.11335E-05	0.16760E-05
-0.91847E-06	-0.94066E-06	-0.16760E-05	0.11335E-05

VITA

MANOJ KUMAR GUPTA

Plot No. 22, 50-58-1/9, Rajendranagar
Visakhapatnam, India 530016

Manoj was born in India. He graduated from the Indian Institute of Technology-Madras in 2003 with a B.Tech. in naval architecture and ocean engineering. His current interest is in turbomachinery. His B.Tech thesis was on finite element modeling and response determination of rudder using NASTRAN/PATRAN under Dr. Springer and Dr. C.P. Vendhan.